

Quantifying Electronic Phenomena in Organic Chromophores

THÈSE N° 8136 (2017)

PRÉSENTÉE LE 5 DÉCEMBRE 2017
À LA FACULTÉ DES SCIENCES DE BASE
LABORATOIRE DE DESIGN MOLÉCULAIRE COMPUTATIONNEL
PROGRAMME DOCTORAL EN CHIMIE ET GÉNIE CHIMIQUE

ÉCOLE POLYTECHNIQUE FÉDÉRALE DE LAUSANNE

POUR L'OBTENTION DU GRADE DE DOCTEUR ÈS SCIENCES

PAR

Antonio PRLJ

acceptée sur proposition du jury:

Prof. J.-E. Moser, président du jury
Prof. A.-C. Corminboeuf, directrice de thèse
Dr I. Tavernelli, rapporteur
Prof. B. Mennucci, rapporteuse
Prof. J. Vanicek, rapporteur



ÉCOLE POLYTECHNIQUE
FÉDÉRALE DE LAUSANNE

Suisse
2017

Acknowledgements

First, I would like to thank Prof. Clemence Corminboeuf for her guidance, her great enthusiasm for research and all her input during these four years. I truly enjoyed being a part of LCMD, an experience that will certainly have a large impact on my future career.

I am very grateful to Prof. Basile Curchod for his enormous help beginning in the early days of my PhD. His incredible passion for science will always be inspiration to me.

My PhD colleagues, Kun-Han Lin and Alberto Fabrizio, are acknowledged for our many collaborations and their friendly support. I wish them both a successful PhD. I also acknowledge Laurent Vannay who has always been very helpful and friendly during the past four years.

I had a pleasure to collaborate with several LCMD postdocs. I thank Dr. Ewa Pastorcza for all her help and support, Dr. Anya Gryn'ova who has always been so inspiring, Dr. Hongguang Liu, Dr. Jian-Hao Li and Dr. Adrien Nicolai with whom I did some enjoyable research. I wish them all successful academic careers.

I am grateful to all the collaborators who directly contributed to the research presented in this thesis. These are Prof. Basile Curchod, Dr. Nađa Došlić, Prof. Denis Jacquemin, Prof. David Casanova, Dr. Ewa Pastorcza, Dr. Jerome Gonthier, Alberto Fabrizio, Laurent Vannay, and Leonard Floryan. Prof. Benedetta Mennucci, Prof. Jiri Vanicek, Dr. Ivano Tavernelli and Prof. Jacques Moser are acknowledged for serving as jury members at my oral exam.

Furthermore, I acknowledge LCMD members: Boodsarin Sawatlon, Thierry Tran, Dr. Benjamin Meyer, Dr. Giulia Mangione, Dr. Riccardo Petraglia, Dr. Piotr de Silva, Dr. Eric Bremond, Dr. Peter Tentscher, Dr. Stepan Ruzicka and Kevin Murray. Special thanks go to Dr. Matthew Wodrich who has always been around to help, and Veronique Bujard who made the administrative work go smoothly.

Several people helped me significantly during the preparation of the thesis, either through critical reading or technical support. I am indebted to Prof. Basile Curchod, Dr. Anya Gryn'ova, Dr. Matthew Wodrich, Thierry Tran, and Dr. Benjamin Meyer.

Finally, funding from European Research Council (COMPOREL, grant 306528) and Swiss National Science Foundation (no. 156001) is acknowledged.

Lausanne, September 10, 2017

Abstract

Challenging ground and excited state problems in the chemistry of common organic chromophores are investigated with state-of-the-art quantum chemical methods.

We present a comprehensive excited state molecular dynamics analysis of (a) fundamental building blocks in organic electronics (thiophene and its derivatives), (b) aggregation-induced emission systems (tetraphenylethylene), and (c) organic fluorophores used for imaging and sensing applications (BODIPY and its derivatives). We identify the efficient excited state deactivation pathways which are essential to understanding the photochemical stability and emissive properties of these compounds. The internal conversion mechanisms of theoretically challenging thiophene and bithiophene molecules are investigated with a trajectory surface hopping approach utilizing reliable electronic structure methods. We gain new insights into the photochemistry and photophysics of these systems, including a new mechanism in thiophene excited state decay and the increased photostability of bithiophene, thereby complementing earlier theoretical and experimental literature. The origin of the non-emissive behavior of tetraphenylethylene in the gas phase is explained by identifying energetically accessible conical intersections which promote radiationless decay. It is implied that restricted access to the conical intersection induces strong emission upon aggregation - a phenomenon that attracted significant research attention recently. Finally, the concept of conical intersection accessibility is utilized to explain the fluorescence quenching in certain *meso*-substituted BODIPY derivatives. We deliver a full mechanistic picture of the nonradiative decay of these molecules, invoking the role of excited state charge transfer and weak intramolecular interactions.

Understanding the failures of quantum chemical electronic structure methods is crucial for subsequent improvements of commonly applied theoretical approximations. To elucidate the origins behind the unbalanced description of the low-lying $\pi\pi^*$ excited states of heteroaromatic molecules (including thiophene and its derivatives, or in general fused heteroaromatics), we employ a range of quantum chemical approaches, from more approximate time-dependent density functional theory (TDDFT) to highly accurate wavefunction-based methods. The drawbacks of standard TDDFT were ascribed to the ubiquitous adiabatic approximation, rather than different functional approximations. On the other hand, the performance of wavefunction-based methods is found to be largely dependent on the treatment of electron correlation, which is key for a balanced description of excited states with disparate electronic character.

Non-covalent molecular interactions are at the origin of many chemical and physical phenomena. While quantifying intermolecular interactions has become a routine task, intramolecular interactions are still considered particularly difficult to treat by theoretical methods. Here, we develop an original wavefunction-based method for quantifying intermolecular and intramolecular interactions on equal footing. The method, intra-SAPT, makes use of a single Slater determinant wavefunction, subject to perturbational corrections. The scheme decomposes interaction energies into physically meaningful components: electrostatics-exchange, induction and dispersion.

Keywords

Excited states, non-radiative decay, trajectory surface hopping, thiophene, tetraphenylethylene, BODIPY, conical intersection, aggregation-induced emission, TDDFT, intramolecular interactions

Résumé

D'importants problèmes dans l'état fondamental et les états excités de procédés chimiques de chromophores organiques usuels sont étudiés à l'aide de méthodes de chimie quantique avancées.

Nous présentons une analyse globale de dynamiques moléculaires dans les états excités (a) de briques élémentaires primordiales dans les électroniques organiques (le thiophène et ses dérivés), (b) de systèmes à émission induite par agrégation (tetraphenylethylene), et (c) des fluorophores organiques utilisés pour des applications d'imagerie et de détection (BODIPY et ses dérivés). Nous identifions des voies efficaces de désactivation de l'état excité qui sont essentielles à la compréhension de la stabilité photochimique et des propriétés émettrices de ces composés. Les mécanismes de conversion interne de thiophène et bithiophène, systèmes moléculaires très exigeants, sont étudiés avec une approche de type "saut de surface" s'appuyant sur des méthodes fiables de structures électroniques. Nous gagnons des connaissances approfondies dans la photochimie et la photophysique de ces systèmes, ce qui inclut un nouveau mécanisme de relaxation de l'état excité du thiophène et l'augmentation de la photo-stabilité du bithiophène, complétant ainsi des études théoriques et expérimentales antérieures. L'origine du comportement non émissif du tetraphenylethylene en phase gazeuse est expliqué en identifiant des intersections coniques accessibles d'un point de vue énergétique, qui encourage une relaxation sans radiations. Il est signifié que la restriction de l'accès à l'intersection conique induit une forte émission par agrégation – un phénomène qui a tout récemment attiré de vives attentions. Finalement, le concept de l'accessibilité à l'intersection conique est utilisé pour expliquer le quenching de fluorescence de certains dérivés meso-substitués du BODIPY. Nous rendons une image mécanistique claire de relaxation non radiative de ces molécules, en invoquant le rôle du transfert de charge dans l'état excité et d'interactions intramoléculaires faibles.

La compréhension des limites des méthodes de chimie quantique est cruciale pour améliorer les approximations théoriques appliquées. Pour comprendre les origines de la description mal balancée des états excités de molécules hétéroaromatiques (incluant le thiophène et ses dérivés), nous employons une panoplie d'approches de chimie quantique, allant de la plus approximée théorie de la fonctionnelle de la densité dépendante du temps (TDDFT) aux méthodes très précises basées sur la fonction d'onde. Les limitations de la TDDFT sont attribuées à la très répandue approximation adiabatique, plutôt qu'aux différentes approximations faites sur les fonctionnelles. Dans un second temps, la performance des méthodes basées sur la fonction d'onde est largement dépendante du traitement de la corrélation électronique, qui est la clé de la description balancée des états excités avec un caractère électronique disparate.

Les interactions moléculaires non-covalentes sont à l'origine de nombreux phénomènes chimiques et physiques. Alors que la quantification de ces interactions intermoléculaires est devenue une routine, les interactions intramoléculaires sont encore considérées comme particulièrement difficiles à traiter avec des méthodes théoriques. Ici, nous développons une méthode originale basée sur la fonction d'onde pour quantifier les interactions intermoléculaires et intramoléculaires sur un pied d'égalité. La méthode, intra-SAPT, se base sur une fonction d'onde construite avec un unique déterminant de Slater, sujette à des corrections perturbatives. Le procédé décompose les énergies d'interactions en plusieurs composantes physiques importantes : l'échange-électrostatique, l'induction et la dispersion.

Mots-clés

Etat excités, relaxation non radiative, trajectoire de saut de surface, thiophène, tetraphenylethylène, BODIPY, intersection conique, émission induite par agrégation, TDDFT, interactions intramoléculaires

Contents

Acknowledgements	i
Abstract.....	iii
Keywords.....	iii
Résumé	v
Mots-clés.....	vi
Chapter 1 Introduction.....	1
Chapter 2 Theory	5
2.1 Time-Dependent Density Functional Theory	5
2.2 Algebraic Diagrammatic Construction Methods.....	7
2.3 Excited State Dynamics: Surface Hopping Approach	9
2.3.1 Alternative methods	11
Chapter 3 Excited State Dynamics of Thiophene and Bithiophene: New Insights into Theoretically Challenging Systems	13
3.1 Introduction.....	13
3.2 Computational details	14
3.3 Results and discussion	15
3.3.1 Vertical excitation energies and spectra	15
3.3.2 Excited state dynamics of thiophene	17
3.3.3 Excited state dynamics of bithiophene	21
3.4 Conclusion	24
Chapter 4 How Does Tetraphenylethylene Relax from its Excited States?.....	25
4.1 Computational details	28
Chapter 5 Rationalizing Fluorescence Quenching in <i>meso</i>-BODIPY Dyes	29
5.1 Computational section.....	33
Chapter 6 Fluorescence Quenching in BODIPY Dyes: The Role of Intramolecular Interactions and Charge Transfer ..	35
6.1 Introduction.....	35
6.2 Results and Discussion.....	36
6.3 Conclusions.....	41
6.4 Computational Section	41
Chapter 7 Qualitatively Incorrect Features in the TDDFT Spectrum of Thiophene-Based Compounds	43

7.1	Computational methods	50
Chapter 8	Low-Lying $\pi\pi^*$ States of Heteroaromatic Molecules: A Challenge for Excited State Methods	51
8.1	Introduction	51
8.2	Computational Details	52
8.3	Results and Discussion	53
8.3.1	The Case of Naphthalene L_a and L_b States	53
8.3.2	Criteria for L_a - and L_b -like States	55
8.3.3	Three Illustrative Compounds	55
8.3.4	Statistical Analysis of Excitation Energy Trends	57
8.4	Conclusions	59
Chapter 9	Intramolecular Symmetry-Adapted Perturbation Theory with a Single-Determinant Wavefunction	61
9.1	Introduction	61
9.2	Theory	62
9.2.1	The zeroth-order energy	62
9.2.2	Energy decomposition	63
9.3	Illustrative examples	65
9.3.1	Computational details	66
9.3.2	Hairpin alkanes-stabilizing effect of dihydrogen contacts	66
9.3.3	$\pi - \pi$ stacking interactions	68
9.3.4	Intramolecular hydrogen bonds	69
9.3.5	Host-guest complexes with a cationic guest	71
9.4	Conclusions	72
Chapter 10	Conclusions and Outlook	75
References		79
Curriculum Vitae		97

Chapter 1 Introduction

Over the last decades, computational theoretical chemistry has evolved into a powerful tool for investigating molecular phenomena, in both a qualitative and quantitative manner. Experimental data, often remarkably non-trivial to interpret on their own, can now routinely be explained by computations. The latter allows us to overcome the difficulties that, as Paul Dirac said, arise from quantum mechanical equations that are “too complex to be solved”.¹ Since *in silico* simulations are indeed trying to closely approximate these “fundamental laws” of nature (*i.e.*, the quantum mechanical equations that cannot be solved exactly, except for the most trivial cases), it comes as no surprise that in recent years more and more phenomena are reliably predicted by theory, even prior to any experimental work. However, the use of computational chemistry is still not a “black box” procedure, and significant effort remains to be made to improve theoretical models and allow the study of molecular systems of an arbitrary size.

In this work, different aspects of the interplay between experiment and theory arise. The first instance is in the field of molecular excited states and excited state molecular dynamics, where both theory and experiment face numerous difficulties which has stimulated both sides to contribute in a complementary manner. Curiously, even the simplest molecules often exhibit rather complex photochemical and photophysical behavior, with competition between radiative and non-radiative deactivation pathways that occur on multiple timescales. While experiment can provide information about the timescales and the quantum yields of specific excited state processes, the mechanistic details of excited state phenomena are completely absent. On the other side, theory is limited (at least, in practice) by a system’s size and complexity, but it provides a fundamental (*i.e.*, atomistic) picture of excited state dynamics. More importantly, theory offers a meaningful interpretation of experimental data - its role is “to provide a framework in which to think, to organize experimental knowledge”.² Figure 1.1 shows the different radiative (*e.g.* fluorescence) and non-radiative deactivation pathways (involving both conical intersections and avoided crossings) of a photoexcited molecule. Understanding the competition between these processes is crucial to deciphering the working principles of organic dyes, with applications in organic light emitting diodes, or as fluorescent labels for imaging and sensing of biologically relevant molecules. Historically, the role of conical intersections has been underestimated in favor of vibronically mediated decay through the avoided crossing, typically described within the Fermi Golden Rule approximation framework.³ However, this has changed recently, due to developments in theoretical chemistry which can directly locate the conical intersections and investigate their role in molecular dynamics. In fact, the energetic accessibility of conical intersections makes the assumptions behind the Fermi Golden Rule invalid. Therefore, this work largely focuses on the role of conical intersections in excited state decay of experimentally relevant organic chromophores. This has facilitated explanation and prediction of the photostability and fluorescence properties of such molecules, opening a way for the holy grail of applied theoretical chemistry – reliable rational molecular design.

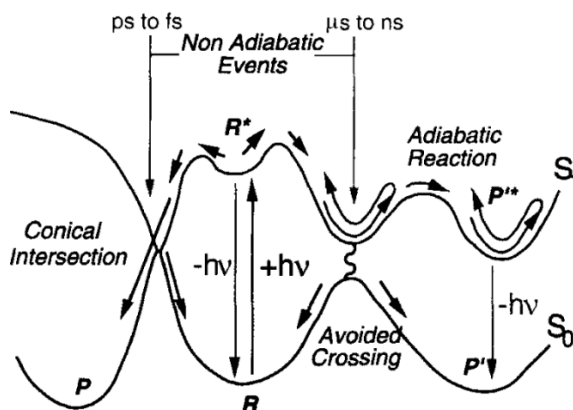


Figure 1.1 Schematic representation of photochemical processes involving conical intersection and avoided crossing. Figure is modified and adopted from ref. [3]

The second aspect explored in this work is how best to assess and improve quantum chemical methods, in order to better match experimental data. Apart from the potentially predictive power of computational models, one should bear in mind that the theory necessarily resorts to approximations. In the context of excited states, arguably the most important decision is the choice of an electronic structure method, which should be both computationally efficient and accurate enough for qualitative and quantitative analyses. For instance, the outcome of excited state molecular dynamics simulations, which are by no means computationally inexpensive, critically depends on the method employed to describe potential energy surfaces on which the dynamics takes place. However, applying highly accurate quantum chemical methods for electronic structure typically makes computations intractable. Making a compromise between accuracy and computational efficiency is, therefore, an indispensable pathway, as long as the experimental observables can be reliably predicted. A great deal of this work focuses on assessing the quality of approximate methods for computing excitation energies and excited state properties and searching for the common failures that may arise for various molecular systems. Modern approaches such as time-dependent density functional theory (TDDFT)⁴ and the family of algebraic diagrammatic construction (ADC)⁵ methods are obvious examples of methods that could potentially meet the desired balance of accuracy and efficiency. While the global performance of these methods, typically assessed by mean absolute deviations or other statistical parameters, is well-known from numerous benchmark studies performed on standard molecular test sets, future research should focus on more specific, albeit challenging problems, such as failures that arise for particular types of molecular excitations based on their molecular orbital and valence bond descriptions. This will not only affect the numerous applications of such methods in the literature. Understanding the origins of such failures is crucial to systematically improve the theoretical approximations and ultimately bring theory closer to the experiment.

Finally, there are some fields of research where experiments only provide a limited picture. A relevant example is non-covalent molecular interactions, whose quantification could substantially deepen our understanding of various chemical and physical phenomena. The latter include stability of materials, energetics of molecular isomers, molecular conformations (for instance, in proteins), supramolecular chemistry, chemical reactions, *etc.* The interpretation of molecular interactions in terms of physically meaningful energy components (*i.e.*, dispersion, electrostatics, polarization, charge transfer) not only allows understanding of structure-property relationships in molecules and molecular assemblies, but opens a way for rational molecular design with previously unprecedented strategies. Indeed, probing the individual molecular interactions directly by experiment is highly challenging, if not completely impossible. Fortunately, modern quantum-chemical approaches have great potential to fill this gap. Despite the significant progress already being made in quantifying intermolecular interactions, intramolecular interactions still remain a great challenge for theory. Ideally, a method which could treat both intermolecular and intramolecular interactions on equal footing could be devised. Therefore, focus is placed on the development of an original theoretical framework for energy decomposition analysis which reconciles both inter- and intra-molecular aspect.

Hereby, we note that the work on intramolecular interactions was done as a side project and the content of the corresponding Chapter is not strongly related to excited state topics. The thesis is organized in the following manner.

In **Chapter 2**, a short overview of the methods employed in this work is given. This includes an introduction to time dependent density functional theory (TDDFT) and the algebraic diagrammatic construction (ADC) methods for the computation of molecular excited states. Furthermore, a brief overview of the methods used to deal with excited state molecular dynamics, with an emphasis on the trajectory surface hopping approach that will be employed in the following chapters is provided.

The Chapters 3-9 are published as articles in peer-reviewed journals. The introduction to each chapter is based on the abstracts from the published work.

In **Chapter 3**, we present excited state dynamics of thiophene and bithiophene. The computational elucidation and proper description of the ultrafast deactivation mechanisms of simple organic electronic units, such as thiophene and its oligomers, is as challenging as it is contentious. A comprehensive excited state dynamics analysis of these systems utilizing reliable electronic structure approaches is currently lacking, with earlier pictures of the photochemistry of these systems being conceived based upon high-level static computations or lower level dynamic trajectories. Here, a detailed surface hopping molecular dynamics of thiophene and bithiophene using the algebraic diagrammatic construction to second order (ADC(2)) method is presented. Our findings illustrate that ring puckering plays an important role in thiophene photochemistry and that the photostability increases when going upon dimerization into bithiophene.

In **Chapter 4** we discuss how tetraphenylethylene relaxes from its excited states. Tetraphenylethylene is a prototypical example of a molecule displaying aggregation-induced emission. Despite many studies on the optical properties of tetraphenylethylene and its derivatives, the origin of the non-emissive behavior in the gas phase or in dilute solutions has yet to be unravelled. Here, we identify the ultrafast deactivation mechanisms responsible for the fluorescence quenching in isolated tetraphenylethylene.

In **Chapter 5** we attempt to rationalize the fluorescence quenching in some *meso*-substituted boron-dipyrromethene (BODIPY) dyes. *meso*-BODIPY dyes are a puzzling class of molecules featuring contrasting emissive behaviors. The full mechanistic picture for these distinctive properties is still missing. Using static and dynamic excited state computations we unravel the key reasons behind these divergences. The principle is illustrated on two structurally similar molecules, vinyl-BODIPY (fluorescent) and ethyl-BODIPY (non-fluorescent). The tendency for luminescence is attributed to the accessibility of the conical intersection between the lowest excited singlet state and the ground state.

Closely related to Chapter 5, in **Chapter 6** we generalize the picture of fluorescence quenching in BODIPY dyes with emphasis on the role of intramolecular interactions and charge transfer. The fluorescence properties of the BODIPY dye and its two *meso*-substituted derivatives, *tert*-butyl- and phenyl-BODIPY, are rationalized. The non-emissive behavior of the latter two are attributed to the energetically accessible low-lying conical intersection between the ground state and the lowest excited singlet state. Both intramolecular non-covalent interactions and excited state charge transfer character are identified as being crucial for “stabilizing” the intersection and prompting nonradiative decay. A similar crossing was located in the bare BODIPY dye, but was energetically less accessible, which correlates well with the high fluorescence quantum yields of the parent dye.

In **Chapter 7** we discuss qualitatively incorrect features in the TDDFT spectrum of thiophene-based compounds. *Ab initio* molecular electronic structure computations of thiophene-based compounds constitute an active field of research prompted by growing interest in low-cost materials for organic electronic devices. In particular, the modeling of electronically excited states and other time-dependent phenomena has moved toward the description of more realistic, albeit challenging, systems. We demonstrate that due to its underlying approximations, time-dependent density functional theory predicts results that are qualitatively incorrect for thiophene and thienoacenes, although not for oligothiophene chains. The failure includes spurious state inversion and excitation characters, incorrect distributions of

oscillator strengths and erroneous potential energy surfaces. We briefly analyze possible origins of this behavior and identify alternative methods that alleviate these problems.

In **Chapter 8** we investigate low-lying $\pi\pi^*$ states of heteroaromatic molecules as a challenge for excited state methods. The description of low-lying $\pi\pi^*$ states of linear acenes by standard electronic structure methods is known to be challenging. Here, we broaden the framework of this problem by considering a set of fused heteroaromatic rings and demonstrate that standard electronic structure methods do not provide a balanced description of the two (typically) lowest singlet state (L_a and L_b) excitations. While the L_b state is highly sensitive to correlation effects, L_a suffers from the same drawbacks as charge transfer excitations. We show that the comparison between CIS/CIS(D) can serve as a diagnostic for detecting the two problematic excited states. Standard TD-DFT and even its spin-flip variant lead to inaccurate excitation energies and interstate gaps, with only a double hybrid functional performing somewhat better. The complication inherent to a balanced description of these states is so important that even CC2 and ADC(2) do not necessarily match the ADC(3) reference.

In **Chapter 9** we present the intramolecular symmetry-adapted perturbation theory with a single-determinant wavefunction. We introduce an intramolecular energy decomposition scheme for analyzing non-covalent interactions within molecules in the spirit of symmetry-adapted perturbation theory (SAPT). The proposed intra-SAPT approach is based upon the Chemical Hamiltonian of Mayer⁶ and the recently introduced zeroth-order wavefunction.⁷ The scheme decomposes the energy between weakly bound fragments located within the same molecule into physically meaningful components, *i.e.*, electrostatic-exchange, induction, and dispersion. Here, we discuss the key steps of the approach and demonstrate that a single-determinant wavefunction can already deliver a detailed and insightful description of a wide range of intramolecular non-covalent phenomena such as hydrogen bonds, dihydrogen contacts, and $\pi - \pi$ stacking interactions. Intra-SAPT is also used to shed some light on competing intra- and intermolecular interactions.

Conclusions and outlook are presented in **Chapter 10**.

Chapter 2 Theory

2.1 Time-Dependent Density Functional Theory

Over the last 20 years, time-dependent density functional theory (TDDFT) has become the most popular approach for the computation of molecular excited states. However, TDDFT itself is much more than that - in fact it is the exact reformulation of the time dependent equations of quantum mechanics, where the fundamental quantity is the electronic density, rather than the many-body electronic wavefunction.⁸ Applications of TDDFT are various (transport through single molecule, high harmonic generation, multiphoton ionization *etc.*),⁹ but as the present work is mainly concerned with the excited states of molecular systems, naturally our overview gravitates in that direction.

Density functional theory relies on two well known theorems by Hohenberg and Kohn.¹⁰ The central theorem of TDDFT, namely the Runge-Gross theorem,¹¹ is the natural (though not trivial) extension of the first Hohenberg-Kohn theorem to time-dependent systems, establishing a one-to-one mapping between the electronic density ρ and the external potential, v_{ext} , now both taken as time dependent quantities. This means that if we know the initial state of the system and its time dependent density, we can determine all the properties of the system at any time, *i.e.* with knowledge of the external potential the time dependent Schrödinger equation could (in principle) be solved. The second Hohenberg-Kohn theorem is the variational principle for electronic densities which ensures that the electronic energy evaluated with any trial density is higher than the energy obtained with the exact density.¹² In time dependent case, the focus of the variational principle is not on the total energy but on the quantum mechanical action A .⁸

$$A[\psi] = \int_{t_0}^{t_1} dt \langle \psi(t) | i \frac{\partial}{\partial t} - \hat{H}(t) | \psi(t) \rangle, \quad (2.1)$$

where:

$$\hat{H} = \hat{T} + \hat{W} + \hat{V}_{ext} \quad (2.2)$$

is the total Hamiltonian, being the sum of kinetic energy, \hat{T} , electron-electron interaction, \hat{W} , and external potential, \hat{V}_{ext} . \hat{V}_{ext} can be written as a sum:

$$V_{ext}(\{r\}, t) = \sum_{i=1}^N v_{ext}(r_i, t), \quad (2.3)$$

where one-particle external potentials v_{ext} describe the (sometimes time-dependent) Coulomb interaction of electrons with nuclei, as well as the interaction with a time-dependent field. $\{r\}$ represent collective electronic degrees of freedom. Total electronic density is written as:¹²

$$\rho(r, t) = \int |\psi(r, r_2, r_3, \dots, r_N; t)|^2 dr_2 dr_3 \dots dr_N. \quad (2.4)$$

In principle, the exact density $\rho(r, t)$ can be obtained from the Euler equation:

$$\frac{\delta A[\rho]}{\delta \rho(r, t)} = 0. \quad (2.5)$$

This stationary principle is the equivalent of the second (variational) Hohenberg-Kohn theorem, and forms the basis for the derivation of the time-dependent Kohn-Sham equations.¹³ The gist of the Kohn-Sham approach, both time-independent and time-dependent, is that the real interacting (and therefore rather complex) system, could be replaced by an auxiliary system of noninteracting electrons with the electron density ρ_{KS} equal to the exact electron density ρ . Noninteracting electrons feel the local potential v_{KS} ,

$$v_{KS} = v_{ext} + v_{Hartree} + v_{xc}. \quad (2.6)$$

Here, v_{xc} is the exchange correlation potential which contains complex many body effects, while $v_{Hartree}$ is the classical part of the electron-electron interaction.⁸ With such auxiliary system in hand, one can construct a simple set of one particle equations, *i.e.* the Kohn-Sham equations, which can be routinely solved on today's computers.

Kohn-Sham equations in their time dependent form read:⁸

$$i \frac{\partial}{\partial t} \Phi_j(r, t) = \left(-\frac{1}{2} \nabla^2 + v_{KS}[\rho](r, t) \right) \Phi_j(r, t), \quad (2.7)$$

where Φ_j are single electron orbitals, which allow us to construct the density:

$$\rho(r, t) = \rho_{KS}(r, t) = \sum_j^N |\Phi_j(r, t)|^2 \quad (2.8)$$

Detailed relation between the stationary principle of the action integral and the Kohn-Sham framework can be found in ref. [4,12]. Obviously, it is possible to vary (and optimize) the density in order to satisfy the stationary action principle, now corresponding to the noninteracting system, *i.e.* A_{KS} . In practice, Kohn-Sham equations are solved instead. The exchange-correlation potential, v_{xc} , is indeed a key ingredient connecting the real system with a simpler noninteracting system. The exact exchange-correlation potential is generally unknown both in DFT and its time-dependent extension. However, while for the ground state DFT many density functionals (with corresponding xc potentials) are devised, forming the so called Jacob's ladder of accuracy, the situation is rather different in TDDFT. The exact TDDFT potential is a functional of the history of the past densities and initial condition and is explicitly time-dependent.¹⁴ In practical approximations memory effects are completely neglected in the so called adiabatic approximation (AA). In the AA, the time dependent xc potential is replaced by the static DFT potential evaluated for the time dependent densities:⁸

$$v_{xc}^{AA}[\rho](r, t) = v_{xc}[\rho](r)|_{\rho=\rho(r,t)} \quad (2.9)$$

While the AA significantly simplifies the problem by allowing the use of well known ground state functional approximations for excited state applications, it is certainly one of the major limiting factors of standard TDDFT. For instance, AA is considered to be a major reason for the lack of double excitations in the TDDFT spectrum.¹⁴ Despite some efforts being made to develop time-dependent memory functionals, the AA is still used in almost all practical applications. Instead of going "beyond" the AA, various approaches to go "around" the AA¹⁴ have been developed (such as spin-flip TDDFT,¹⁵ constricted variational DFT¹⁶ *etc.*).

It remains to be seen how to evaluate excitation energies for a given molecular system. Time propagation of the Kohn-Sham equations, the so called real-time TDDFT,^{17,18} is one way, although not so common in chemistry. The linear-response TDDFT is by far the most used.

If the external potential is changed by a small perturbation δv_{ext} the change in the density in linear order can be expressed as:⁸

$$\delta \rho(r, \omega) = \int dr' \chi(r, r', \omega) \delta v_{ext}(r', \omega) \quad (2.10)$$

Note that the frequency domain rather than time domain is used. χ is known as the linear density response function⁸ or susceptibility.¹⁴ Analogously, the change of density can be expressed referring to the noninteracting Kohn-Sham system:⁸

$$\delta\rho(r, \omega) = \int dr' \chi_{KS}(r, r', \omega) \delta v_{KS}(r', \omega) \quad (2.11)$$

The relation between the response function of the interacting system, χ , and the one from Kohn-Sham system, χ_{KS} , is given by a Dyson-like equation:^{8,12}

$$\chi(r, r', \omega) = \chi_{KS}(r, r', \omega) + \int dr'' \int dr''' \chi(r, r'', \omega) \left[\frac{1}{|r'' - r'''|} + f_{xc}(r'', r''', \omega) \right] \chi_{KS}(r''', r', \omega) \quad (2.12)$$

where f_{xc} is the xc kernel, which appears to be a crucial term, containing complex many-body effects. The exact χ itself can be written in the Lehman representation,⁸ where it becomes obvious that the poles of the response function correspond to the excitation energies. However, instead of evaluating χ through the slowly converging equation (2.12), it is common to solve the equivalent set of non-Hermitian eigenvalue equations, *i.e.* the Casida equations:¹⁹

$$\begin{bmatrix} A & B \\ B^* & A^* \end{bmatrix} \begin{bmatrix} x \\ y \end{bmatrix} = \Omega \begin{bmatrix} 1 & 0 \\ 0 & -1 \end{bmatrix} \begin{bmatrix} x \\ y \end{bmatrix} \quad (2.13)$$

where Ω are excitation energies, $x(y)$ transition amplitudes for excitations(de-excitations), and matrix elements of A and B are given as a sum of two-electron integrals (in Mulliken notation):

$$\begin{aligned} A_{ia,jb} &= \delta_{ij} \delta_{ab} (\varepsilon_a - \varepsilon_i) + (ia|jb) + (ia|f_{xc}|jb), \\ B_{ia,jb} &= (ia|bj) + (ia|f_{xc}|bj), \end{aligned} \quad (2.14)$$

ε being KS orbital energies and i, j, a, b KS orbitals.

When TDDFT equations are recast in this matrix form the relation with other wavefunction based methods becomes more obvious.¹² The equations of TDHF (also known as random phase approximation, RPA) strongly resemble those of TDDFT, being only different in the last terms of A and B . If B matrix is neglected in equation (2.13), also known as Tamm-Dancoff approximation (TDA),²⁰ Hermitian eigenvalue equation is obtained:

$$A\omega = \omega X \quad (2.15)$$

TDA on TDHF gives the configuration interaction singles (CIS) method. However, in contrast to CIS and TDHF, TDDFT in this form is still formally exact (*i.e.* if we do not use AA and have exact xc kernel and potential).

2.2 Algebraic Diagrammatic Construction Methods

The family of algebraic diagrammatic construction (ADC) methods^{21,22} represents a viable wavefunction-based alternative to TDDFT. ADC(1) is an equivalent of CIS⁵ and as such provides a very crude description of molecular excited states. However, the ADC(2) approach allows for the description of important correlation effects and performs fairly well for the (dominantly singly) excited states of typical conjugated organic molecules.⁵ The method is commonly referred to as the “MP2 for excited states”. Despite the possibilities of efficient implementation, employing approximations such as resolution of identity,²³ ADC(2) has relatively steep computational scaling (n^5 , where n is the number of orbitals) which prevents its use beyond middle sized molecules (10-30 atoms of the second row in the periodic table). Fortunately, most of the systems considered in this thesis belong to this class. Further in the hierarchy is ADC(3) which is mainly used for benchmark purposes, due to its high computational burden and scaling relation of n^6 .⁵

The ADC scheme has its roots in many body Green's function theory, while effectively it combines diagonalization of the Hermitian secular matrix and Rayleigh-Schrödinger perturbation theory for the secular matrix elements.²¹ Before providing a summary of ADC methods, we emphasize that the “algebraic diagrammatic construction” approach may be applied for the computation of various observables, such as electron affinities, ionization potentials, *etc.* In the context of excited states, we necessarily speak about algebraic diagrammatic construction for the polarization propagator; other properties are related to other respective propagators.⁵

Polarization propagator describes the time evolution of the electronic polarization of a molecule in the ground state, *i.e.* the propagator acts on the ground state wavefunction and propagates the ground state density fluctuations.⁵ The expression for the polarization propagator reads:

$$\Pi(\omega) = \Pi^+(\omega) + \Pi^-(\omega), \quad (2.16)$$

where the two terms (containing the same physical information) are trivially related as:

$$\Pi^+(-\omega) = \Pi^-(\omega), \quad (2.17)$$

and their matrix elements are given as:

$$\Pi_{pq,rs}^+(\omega) = \sum_{n \neq 0} \frac{\langle \psi_0 | c_q^\dagger c_p | \psi_n \rangle \langle \psi_n | c_r^\dagger c_s | \psi_0 \rangle}{\omega + E_0 - E_n}. \quad (2.18)$$

c_q^\dagger (c_p) are creation (annihilation) operators of the electron in respective Hartree-Fock orbitals, ψ_0 is a ground state wavefunction with the corresponding total energy E_0 , ψ_n excited state wavefunction with the corresponding energy E_n , and the sum runs over all excited states n . Therefore, polarization propagator carries the information about the vertical excitation energies which correspond to the poles of the function ($\omega = E_n - E_0$), whereas the residues are transition probabilities.⁵ Starting with the Lehmann representation of the polarization propagator, we outline the formal derivation of the ADC equations. However, the actual implementations are typically based on the intermediate state representation formalism.^{24–26}

The non-redundant part of the propagator can be rewritten in a compact diagonal representation as:⁵

$$\Pi(\omega) = X^\dagger (\omega - \Omega)^{-1} X, \quad (2.19)$$

where Ω is a diagonal matrix of excitation energies ω_n and X is a matrix of transition amplitudes. Schirmer rewrote the expression in a non-diagonal form:^{5,21}

$$\Pi(\omega) = f^\dagger (\omega - M)^{-1} f, \quad (2.20)$$

with M being the non-diagonal matrix representation of an effective Hamiltonian, and f being a matrix of effective transition moments. The relation between Ω and M is a Hermitian eigenvalue problem:

$$MY = Y\Omega, Y^\dagger Y = \mathbf{1}, \quad (2.21)$$

i.e. the diagonalization of M provides eigenenergies ω_n and eigenvectors Y , where

$$X = Y^\dagger f. \quad (2.22)$$

Schirmer *et al.*^{21,27} provided the explicit expressions for the matrix elements of M and f , which are both perturbationally expanded:

$$M = M^{(0)} + M^{(1)} + \dots \quad (2.23)$$

$$f = f^{(0)} + f^{(1)} + \dots$$

This is the basis for a systematic hierarchy of approximations ADC(n). With matrix elements $M_{\mu\nu}^{(n)}$ and $f_{\mu}^{(n)}$ in hand, where indices μ and ν correspond to the excitation levels (*i.e.* singles, doubles, triples *etc.*), ADC(n) equations can be built.

For the celebrated ADC(2) level (within its strict implementation) particle-hole block M_{11} is expanded up to the second order in perturbation theory, the coupling block, M_{12} , between the single and double excitations (p-h, 2p-2h) is expanded up to the first order, and 2p-2h block M_{22} up to the zeroth order.⁵ As for the transition amplitude matrix f , the p-h part is expanded up to the second and 2p-2h up to the first order. In the ADC(3) perturbational orders considered are systematically one order higher while the 3p-3h space is not explicitly considered.⁵ Finally, an overview of other (less common) ADC approximations, such as extended ADC(2)-x and the spin opposite scaling SOS-ADC(n) can be found in reference [5]. Hättig has shown that ADC(2) is a close approximation of the second order approximate coupled cluster singles and doubles, CC2 method, as ADC(2) symmetric matrix M can be derived from the non-symmetric CC2 Jacobian.²⁸

2.3 Excited State Dynamics: Surface Hopping Approach

Solving a problem of molecules in motion in different excited states implies the solution of the time-dependent Schrödinger equation for a given many-particle system. Since solving the time-dependent Schrödinger equation for a molecular system is feasible only for the smallest systems (those with a few degrees of freedom), various approximations have to be applied. Tully distinguishes three general pathways: fully quantum mechanical, semiclassical, and mixed quantum-classical (MQC) methods.²⁹ In the latter, which we shall consider in more detail further, nuclear motion is treated by classical mechanics while electronic degrees of freedom are still treated quantum mechanically. The two subsystems, the quantum and the classical one, mutually “interact”, which is one of the most challenging features of MQC methods.

The total Schrödinger equation for a molecular system reads:

$$i\hbar \frac{\partial}{\partial t} \Psi(\mathbf{r}, \mathbf{R}, t) = \hat{H}(\mathbf{r}, \mathbf{R}) \Psi(\mathbf{r}, \mathbf{R}, t), \quad (2.24)$$

where \mathbf{r} and \mathbf{R} are collective electronic and nuclear positions, respectively. Ψ is a time dependent molecular wavefunction and \hat{H} the total (non-relativistic) molecular Hamiltonian, being the sum of the nuclear kinetic energy operator and the electronic Hamiltonian, $\hat{H}(\mathbf{r}, \mathbf{R}) = \hat{T}_n(\mathbf{R}) + \hat{H}_{el}(\mathbf{r}; \mathbf{R})$. The electronic Hamiltonian contains an electronic kinetic energy term and all the (Coulomb) interaction terms, being parametrically dependent on nuclear degrees of freedom \mathbf{R} . It is convenient to split slow (nuclear) and fast (electronic) degrees of freedom, although this choice of separation is neither unique, nor always optimal.²⁹ Decoupling of the nuclear and electronic motion is done by the well-known Born-Oppenheimer approximation³⁰ with the argument that the nuclear motion is much slower than the electronic one.

The total wavefunction can be expanded as:

$$\Psi(\mathbf{r}, \mathbf{R}, t) = \sum_i^{\infty} \psi_i(\mathbf{R}, t) \varphi_i(\mathbf{r}; \mathbf{R}) \quad (2.25)$$

which is known as the Born-Huang expansion.^{31,32} Here φ_i denote electronic wavefunctions which are the eigenfunctions of \hat{H}_{el} and ψ_i are nuclear wavefunctions. Note that in this expansion (which is exact, but certainly not unique), time dependence is completely transferred to the nuclear part. The electronic part φ_i is, instead, parametrically dependent on the nuclear geometry \mathbf{R} . The corresponding eigenenergies E_i coming from the electronic Schrödinger equation therefore depend parametrically on the nuclear coordinates, forming the so called potential energy surfaces (PESs). By inserting (2.25) into (2.24), multiplying with φ_j from the left and integrating over the electronic degrees of freedom \mathbf{r} , we obtain the equation for the nuclear amplitudes:

$$i\hbar \frac{\partial}{\partial t} \psi_j(\mathbf{R}, t) = [\hat{T}_n(\mathbf{R}) + E_j(\mathbf{R})] \psi_j(\mathbf{R}, t) + \sum_i^{\infty} D_{ji}(\mathbf{R}) \psi_i(\mathbf{R}, t) \quad (2.26)$$

where D_{ji} are nonadiabatic coupling matrix elements.³² Since the summation in (2.26) runs over all electronic states, it is these terms that couple the multiple electronic states with the nuclear motion and give equation (2.26) its enormous complexity. In the adiabatic Born-Oppenheimer approximation, the D_{ji} terms are completely neglected: the first step is to omit the nondiagonal terms (Born-Oppenheimer approximation), and in a second step one also drops the diagonal terms D_{ii} , which are supposedly small when compared to the electronic energy. If the nonadiabatic terms are neglected, the dynamics effectively proceeds on a single potential energy surface, also known as adiabatic dynamics. This is a sensible approximation if one electronic state is well separated from the manifold of other states, and if nonadiabatic couplings are indeed negligible. Such situation is common for most organic molecules (closed-shell) in their ground electronic state, which is typically separated from the excited states by at least several eV. The existence of a sizable energy gap may not be the case for metallic compounds or open-shell organic molecules. Another common situation where nonadiabatic couplings cannot be *a priori* neglected is the excited state dynamics of essentially all the molecular systems, where multiple electronic states are directly involved. For that reason, we have to go beyond the Born-Oppenheimer approximation.³³

The trajectory surface hopping method³⁴ is a popular MQC approach to deal with the issue of non-Born-Oppenheimer effects. A classical Newtonian equation for the nuclei can be easily derived from equation (2.26) (after neglecting the nonadiabatic terms) by employing a polar representation of the nuclear wavefunction and applying the classical limit $\hbar \rightarrow 0$.^{32,35} It reads:

$$M_\alpha \ddot{\mathbf{R}}_\alpha(t) = -\nabla_\alpha E_j(\mathbf{R}(t)), \quad (2.27)$$

where the force on the atom α with mass M_α is equal to the negative gradient of the (single) electronic PES for state j . Since in excited state molecular dynamics many PESs are directly involved (corresponding to different electronic excited states) the question “Which state should be used to compute the forces for the Newton equation?” is of crucial importance. In the surface hopping method the nuclear gradients are always evaluated for a single PES along the trajectory, while the system from time to time “hops” between different surfaces. Therefore, the surface hopping algorithm is a “decision-maker” which determines on which surface the gradient will be computed at each instance of time. Alternatively, in the Ehrenfest approach, another common MQC method, classical nuclear gradients are evaluated on an average PES that is formed by a linear combination of many electronic excited states. For that reason, Ehrenfest is called a mean-field method, which poses various limitations in practical molecular applications.³⁵

In surface hopping, the total molecular wavefunction is commonly expanded in the complete set of adiabatic electronic states:^{32,34}

$$\Psi(\mathbf{r}, \mathbf{R}, t) = \sum_i^\infty C_i(t) \varphi_i(\mathbf{r}; \mathbf{R}) \quad (2.28)$$

with the time dependent coefficients $C_i(t)$ associated with each state i (alternatively, wavefunction can be expanded in diabatic or any other basis). Here we consider a discrete nuclear trajectory $\mathbf{R} = \mathbf{R}(t)$ along which the molecular system evolves. Nuclear quantum wavepacket is represented by a swarm of independent trajectories, each of which corresponds to a distinct initial condition (nuclear positions and momenta) sampled from a given distribution function (Boltzmann, Wigner). Inserting Eq. (2.28) into the electronic time-dependent Schrödinger equation we obtain a set of first-order differential equations for the coefficients:^{32,34}

$$\dot{C}_j(t) + \frac{i}{\hbar} E_j C_j(t) + \sum_i^\infty \Lambda_{ji} C_i(t) = 0. \quad (2.29)$$

The equations are coupled due to the sum containing nonadiabatic coupling terms:

$$\Lambda_{ji} = \sum_\alpha^{N_n} \int d\mathbf{r} \varphi_j^*(\mathbf{r}; \mathbf{R}) \nabla_\alpha \varphi_i(\mathbf{r}; \mathbf{R}) \cdot \dot{\mathbf{R}}_\alpha, \quad (2.30)$$

where the first-derivative nonadiabatic couplings (*i.e.* the integral) are multiplied by the nuclear velocities. Note that the integral refers to first-order couplings, while D_{ji} terms in (2.26) contain both first and second-order couplings. To solve the set of equations (2.29) we need to know the nonadiabatic couplings. They are computed either directly from

ab initio methods, or approximated by the wavefunction overlap method proposed by Hammes-Schiffer and Tully,³⁶ the latter often being used with methods that provide no direct access to excited state wavefunction (TDDFT, ADC(2)).³⁷

As noted earlier, in surface hopping the system always evolves on a single electronic potential energy surface, but jumps between the states are possible. The jump probability will depend on both the state coefficients and the nonadiabatic couplings. The most widely applied hopping criterion was proposed by Tully in the early 90s (Tully's fewest switches trajectory surface hopping), with the hopping probability (from state j to state i in the time interval $[t, t + dt]$) given as:^{32,34}

$$g_{ji}(t, t + dt) = 2 \int_t^{t+dt} d\tau \frac{-\text{Re}[C_i(\tau)C_j^*(\tau)\Lambda_{ij}(\tau)]}{C_j(\tau)C_j^*(\tau)} \quad (2.31)$$

The surface hop is allowed based on the "stochastic" criterion:

$$\sum_{k \leq i-1} g_{jk} < \zeta < \sum_{k \leq i} g_{jk} \quad (2.32)$$

where ζ is a uniformly selected random number between 0 and 1.

The surface hopping algorithm is not a rigorous classical limit of quantum mechanical equations and it lacks a formal derivation. However, it is an attractive method for excited state dynamics due to its simple implementation, "on-the-fly" propagation and the straight-forward interpretation of its results; all these points made it the most popular approach for excited state dynamics applications. It approximately satisfies the internal consistency, *i.e.* the fraction of trajectories assigned to each electronic state corresponds to the probabilities $|C_i(t)|^2$.³⁵ Problems with quantum decoherence were described in early applications,³⁸ and a number of corrections was proposed.^{39–41} Due to the classical treatment of nuclear motion, any nuclear quantum effects such as tunneling, interferences and zero-point motion are neglected. Other limitations come from the fact that trajectories are computed independently, while in principle a swarm should be propagated simultaneously with a mutual feedback to accurately describe coherence/decoherence effects.³⁵ Critical discussions on surface hopping can be found in the vast literature on the topic.^{35,42–46}

2.3.1 Alternative methods

Apart from trajectory surface hopping and Ehrenfest dynamics, alternative approaches for nonadiabatic molecular dynamics are briefly introduced.

Among the fully quantum mechanical methods (*i.e.*, nuclear dynamics is described by wavepacket propagation) the most prominent is multiconfiguration time-dependent Hartree (MCTDH).^{47,48} MCTDH has been applied to various molecular systems,⁴⁹ however, due to the large computational cost only a limited number of degrees of freedom (*e.g.*, vibrational modes) can be taken into account. Unlike surface hopping, which assumes an "on the fly" trajectory propagation, MCTDH typically requires precomputation of potential energy surfaces, although algorithms for direct dynamics have also been introduced.⁴⁸

Ab initio multiple spawning (AIMS), proposed by Martínez *et al.*,⁵⁰ combines advantages of both trajectory-based and wavepacket-based methods. AIMS is based on propagation of frozen Gaussian functions along the classical trajectories which allows for the formally exact description of nonadiabatic dynamics. The recent coupling of the AIMS method with GPU-accelerated electronic structure algorithms has permitted applications on fairly large molecular systems, treated in their full dimensionality.^{51,52}

Exact factorization is a general framework proposed by Gross *et al.*,⁵³ in which the molecular wavefunction (the solution of time-dependent Schrödinger equation) is factorized into a simple product of nuclear and electronic time-dependent wavefunctions, evolution of which is described by two connected differential equations.³²

Finally, among the semiclassical approaches (*i.e.*, referring to various semiclassical approximations in quantum mechanics), a variety of methods have been introduced.^{54–57}

Chapter 3 Excited State Dynamics of Thiophene and Bithiophene: New Insights into Theoretically Challenging Systems

The Chapter is published as: Prlj, A.; Curchod, B. F. E.; Corminboeuf, C. Phys. Chem. Chem. Phys. 2015, 17, 14719-14730.

3.1 Introduction

Owing to its prevalent role in biology and optoelectronics, organic photochemistry^{58,59} has received considerable experimental and theoretical interest. Aided by theory, experimental data can now be interpreted in previously unrealized ways. Concepts such as electronic potential energy surfaces and conical intersections⁶⁰ enhance understanding of phenomena that occur upon photoexcitation. Special attention has been devoted to the ultrafast deactivation mechanisms of small heteroaromatic molecules including pyrrole,^{61,62} furan,^{63,64} imidazole,⁶⁵ as well as others. On one hand, such simple systems represent fundamental building blocks of many biomolecules in which excited state deactivation may play important biological roles.⁶⁶ On the other hand, thiophene is the most illustrative molecular unit for optoelectronic applications;^{67,68} oligomers and polymers of this species dominate the field of organic electronics being utilized in solar cells,^{69,70} light emitting diodes,^{71,72} photoswitches⁷³ etc. It is the omnipresence of thiophene that has prompted fundamental research on its electronic properties, particularly on its excited states.

The fact that thiophene is non-fluorescent has been known for some time.⁷⁴ Ultrafast radiationless decay was confirmed by Weinkauff *et al.*'s pump-probe experiments⁷⁵ and interpretations by Marian *et al.*⁷⁶ Their TDDFT (time dependent density functional theory) and DFT-MRCI (density functional theory-multireference configuration interaction) computations, indicated that a ring opening mechanism is responsible for the internal conversion from the excited to the ground state, where deactivation is succeeded by a final ring closure.⁷⁶ In line with these results, surface hopping molecular dynamics simulations by Cui and Fang⁷⁷ initiated in the first singlet excited state (S_1) and employing the complete active space self-consistent field method (CASSCF) implied that ring opening through C-S bond cleavage is the sole deactivation mechanism from the S_1 state. Alternatively, Stenrup⁷⁸ suggested that the ring puckering mechanism could play a role based on scans of the CASPT2 (complete active space perturbation theory of second order) potential energy surfaces. Deactivation through a ring deformation event is known from pyrrole and furan photochemistry,^{61,64} making it somewhat curious that such a mechanism was not previously identified for thiophene. Most recently, Fazzi and co-workers presented a nonadiabatic molecular dynamics of the excited states of thiophene (and oligothiophenes) using TDDFT.⁷⁹ Whereas a relaxation process through the ring puckering mechanism was identified, these results are called into question owing to failures found in TDDFT spectra (*e.g.*, spurious state inversion and excitation characters, wrong distribution of oscillator strengths and erroneous potential energy surfaces which are independent from the exchange-correlation functional used in the TDDFT computation).^{80,81}

Since a fully reliable theoretical study of the photochemistry of thiophene and its related oligomers appears to be lacking, here, we provide a surface hopping molecular dynamics study of thiophene using the algebraic diagrammatic construction to second order^{21,22} (ADC(2)) method. Our findings verify that the ring puckering process indeed does play a critical role in the deactivation process, even when dynamic simulations are initiated on the S_1 potential energy surface. This mechanism operates on the same timescale as the ring opening mechanism, making experimental distinction more difficult. As opposed to CASSCF, which has the formal advantage in treating conical intersections, but misses essential dynamic correlation effects, ADC(2) is a correlated single-reference method. The method is sometimes

seen as a “MP2 for excited states” and often considered as a compromise to EOM-CCSD in terms of accuracy vs. efficiency for electronic-state calculations⁵ (for a detailed discussion on the ADC(2) formalism, the reader is referred to recent reviews^{5,28}). ADC(2) has been successfully applied to an important number of molecular systems^{5,82,83} and, more specifically, for thiophene-based molecules.^{80,84,85} In the case of thiophene,⁸⁰ ADC(2) reproduces the electronic state ordering given by CASPT2 at the ground-state geometry, while TDDFT suffers from its approximation and inverts the character of the first two electronic states. When it comes to excited-state properties and dynamics, ADC(2) is considered to be more robust than CC2 (approximate coupled cluster singles and doubles) as its eigenvalue problem is Hermitian.^{28,37,86} It is for example known that in the region of a conical intersection between excited states of same symmetry, CC2 excitation energies can become complex whereas ADC(2) behaves properly.²⁸ ADC(2) (which formally scales as n^5 with the number of orbitals) is therefore a method of choice for excited-state dynamics^{37,86} and has recently been combined with trajectory surface hopping, providing non-radiative decays for 9H-adenine in good agreement with higher-level methods.³⁷

In contrast to thiophene, the photochemical processes of bithiophene have been examined only by static computations^{87–92} with the exception of the recent TDDFT study of Fazzi and co-workers.⁷⁹ In the present study, we find that bithiophene preserves the key features of thiophene photochemistry, including the ring opening mechanism. However, we also find the lowest singlet excited state to have a significantly increased photostability, which may be linked with the wide-ranging application of oligothiophenes in optoelectronic devices. In fact, the increased photostability of the singlet state points to the possibility of intersystem crossing, as suggested by earlier studies.^{74,90}

3.2 Computational details

The ground state structures of thiophene and bithiophene and corresponding vibrational frequencies were obtained at the MP2/def2-TZVP⁹³ level. Excited states were consistently computed at the ADC(2)/def2-SVPD⁹⁴ level. Adiabatic excitation energies were computed by optimizing ground and excited state structures with the def2-SVPD basis set. The absorption spectra and the initial conditions for the nonadiabatic dynamics simulations of both systems were computed for geometries and nuclear momenta sampled from an uncorrelated Wigner distribution (0 K),^{95,96} as implemented in the Newton-X package.⁹⁷ 700 initial conditions (structures and momenta) were sampled for each compound from the Wigner distribution computed from harmonic vibrational frequencies in the ground state. For each structure, vertical excitation energies (the 5 lowest singlet states) and oscillator strengths were computed and the spectral transitions were broadened by a Lorentzian with a phenomenological broadening of 0.05 eV. The same set of initial conditions was used for the nonadiabatic *ab initio* dynamic simulations. With the assumption of the initial vertical excitation, a swarm of trajectories was propagated in the excited states where the nuclear motion was treated classically. Nonadiabatic effects were treated by Tully’s fewest switches surface hopping method³⁴ with the decoherence correction ($\alpha = 0.1$).⁴⁴ The microcanonical (NVE) framework was used. In total, 200 trajectories for thiophene with maximal time of 400 fs and 100 trajectories for bithiophene with maximal time of 500 fs were computed, with a nuclear time step of 0.5 fs. Due to methodological difficulties, *i.e.*, the absence of nonadiabatic couplings between the ADC(2) excited states and their underlying MP2 ground state, the hopping to the ground state was not considered and all the trajectories were terminated after reaching the crossing point between the excited (running) state and the ground state.^{37,86} It is furthermore important to note that in Newton-X nonadiabatic couplings are not directly computed from the ADC(2) electronic wavefunction, but rather from a CIS-like reconstructed wavefunction. For more information about the ADC(2) based surface hopping, the reader can refer to ref. [37] and [86].

All ADC(2) and MP2 computations were performed with Turbomole 6.5,⁹⁸ employing the resolution of identity and frozen core approximations. The dynamic simulations were performed with the Newton-X software⁹⁷ interfaced to the Turbomole 6.5 program suite. Molecular structures were visualized with the VMD 1.9.1 program.⁹⁹ Finally, due to the unavailability of spin–orbit coupling matrix elements at the ADC(2) level, the former were computed with TDDFT (PBE0¹⁰⁰/ZORA-DZP¹⁰¹), using the Zeroth Order Regular Approximation (ZORA) Hamiltonian,¹⁰² as implemented in the Amsterdam Density Functional (ADF2013.01 release) program package.^{103–105} EOM-CCSD computations for bithiophene were converged with the *jun*-cc-pVTZ basis set¹⁰⁶ in the Gaussian 09 program package.¹⁰⁷

3.3 Results and discussion

3.3.1 Vertical excitation energies and spectra

Low-lying excited states of thiophene include two $\pi\pi^*$ states (A_1 and B_2) which account for most of the absorption intensity and a slightly higher antibonding $\pi\sigma^*$ state (B_1) responsible for the ring opening process. Achieving a balanced description of these states using electronic structure methods is not an easy task. In a recent letter⁸⁰ we showed that CIS (configuration interaction singles) and TDDFT invert ordering of the two $\pi\pi^*$ states. This is somewhat surprising for TDDFT, which is usually considered reliable for $\pi\pi^*$ states. Nevertheless, standard functionals are unable to provide a picture comparable to reference wavefunction methods due to shortcomings affecting the treatment of both exchange and correlation. On the other hand, $\pi\sigma^*$ states (B_1 and A_2) have a pronounced diffuse character and can also been assigned as $\pi\sigma^* + \text{Rydberg}$ transition. A similar state exists in pyrrole causing the dissociation of the N–H bond,⁶¹ and its correct assignment was questioned in the literature.¹⁰⁸ For a good description of such $\pi\sigma^*$ states the basis set should contain at least few diffuse functions. In the present work, we use ADC(2) with a def2-SVPD basis set that satisfies this criterion. Although relatively small, this basis set yields results similar to larger basis sets, for a computational cost lower than a triple-zeta basis set. This is especially important in the context of nonadiabatic *ab initio* dynamics, which relies upon a good balance between accuracy and computational efficiency. Table 3.1 compares our vertical excitation energies with the reference results taken from the literature. The excitation energies to the triplet states are listed in the electronic supporting information (ESI).

Table 3.1 Comparison of vertical excitation energies (in eV) and corresponding oscillator strengths (in parentheses) obtained with ADC(2)/def2-SVPD and the values from the literature, as well as EOM-CCSD/*jun*-cc-pVTZ. Several numbers were not reported or did not converge (—). For details on the molecular geometries and basis sets used see the original articles

Thiophene	$A_1(\pi_2\pi_4^*)$	$B_2(\pi_3\pi_4^*)$	$B_1(\pi_3\sigma^*)$	$A_2(\pi_2\sigma^*)$	$A_2(\text{Ryd})$
ADC(2)	5.82(0.093)	6.23(0.112)	6.45(0.011)	6.60(0.0)	6.77(0.0)
MS-CASPT2 ⁷⁸	5.85(0.067)	6.14(0.109)	6.57(0.0)	6.65(0.0)	—
EOM-CCSD ¹⁰⁹	5.78(0.081)	6.13(0.084)	6.33(0.013)	6.37(—)	6.19(—)
DFT-MRCI ⁷⁶	5.39(0.114)	5.54(0.112)	5.86(0.004)	6.10(0.0)	5.88(0.0)
Bithiophene	$B(\pi_6\pi_7^*)$	$A(\pi_5\pi_7^*)$	$B(\pi_4\pi_7^*)$	$A(\pi_6\sigma^*)$	$B(\text{Ryd})$
ADC(2)	4.59(0.445)	5.32(0.007)	5.47(0.146)	5.70(0.002)	5.80(0.002)
EOM-CCSD	4.62(0.378)	5.38(0.006)	5.50(0.097)	5.67 (0.008)	—
SS-CASPT2 ⁹¹	4.11(0.32)	—	5.14(0.13)	—	—

To gain a better insight into the character of the excited states listed in Table 3.1, the most relevant molecular orbitals are displayed in Figure 3.1. It is well known that the Hartree–Fock orbitals may significantly change their shape depending on the size of the basis set,¹¹⁰ while the excitations can be expressed with a large number of orbital transitions having sizeable amplitudes. For that reason, we find more convenient to display transition natural orbitals, which better reflect the main character of the states. The natural transition orbitals are used here only in a qualitative way, but we notice that they were computed by neglecting correlation effects in the ground state and the double excitations in excited states.

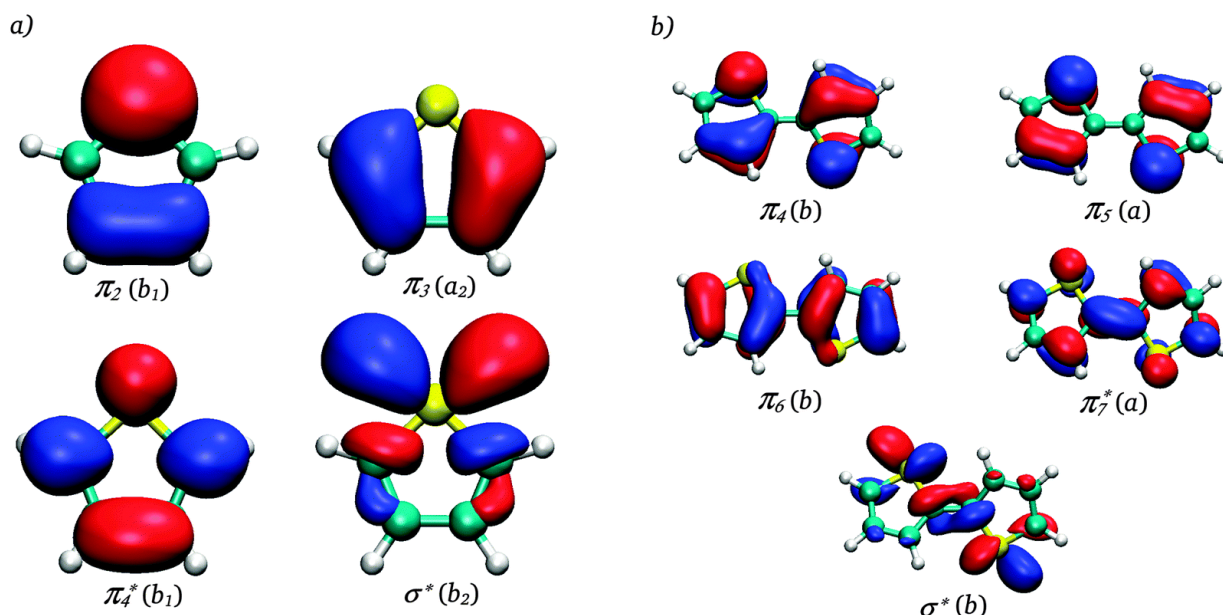


Figure 3.1. (Natural transition) orbitals involved in the lowest singlet transitions of (a) thiophene and (b) bithiophene (isovalue = 0.04).

For thiophene, a reasonable agreement is achieved between our ADC(2) vertical excitation energies, the CASPT2 results of Stenrup⁷⁸ and the EOM-CCSD (equation of motion – coupled cluster singles doubles) of Holland *et al.*¹⁰⁹ The Rydberg state (A_2) is higher in energy with ADC(2), although this should have no effect on the dynamics in the low-lying states. The DFT-MRCI energies computed by Marian *et al.*⁷⁶ are somewhat lower and closer to the experimental peak maxima measured at 5.26¹¹¹/5.48¹¹² eV for $A_1(\pi\pi^*)$ and 5.64¹¹¹/5.93¹¹² eV for $B_2(\pi\pi^*)$ state. However, it is known that vertical excitation energies should not be strictly compared to the experimental band maxima^{113,114} and this is especially true for thiophene, which is characterized by a strong coupling between the two $\pi\pi^*$ states.^{76,78} Instead, a more suited comparison is achieved with the adiabatic (ΔE_{0-0}) excitation energies. In this respect, our ΔE_{0-0} energy for the A_1 minimum (5.17 eV) agrees well with experiment¹¹⁵ (5.16 eV), and so does the CASPT2 result of Stenrup⁷⁸ (5.12 eV), and the TDDFT + DFT-MRCI value of Marian *et al.*⁷⁶ (5.16 eV) (zero point energy corrections are not taken into account in all three cases). Whereas our recent study demonstrated that TDDFT yields incorrect geometries,⁸⁰ this issue was resolved by Marian *et al.*⁷⁶ through imposing a symmetry constraint. The elusive $B_2(\pi\pi^*)$ minimum is a more intriguing question. For this state, the ΔE_{0-0} was never determined experimentally¹⁰⁹ and no minimum was found at the CASPT2 level,⁷⁸ implying that the B_2 state is most likely unbound. Our ADC(2) computations support this view as no B_2 minimum was located. The geometries resulting from the TDDFT⁸⁰ and CASSCF¹¹⁶ optimizations are most likely spurious.

The vertical excitation energies of bithiophene are also reported in Table 3.1. Good agreement was found between the ADC(2) and EOM-CCSD results computed on the same geometry. The CASPT2 energies of Andrzejak and Witek⁹¹ are lower than our ADC(2) values. However, they correspond to the C_{2h} symmetric structure whereas the true ground state minimum is not planar.¹¹⁷ Imposing planarity lowers the ADC(2) excitation energies to 4.34 and 5.45 eV for the two bright $\pi\pi^*(B)$ states. It is not surprising that the excitation energy of S_1 decreases significantly upon planarization: the excited state gets stabilized (S_1 has a planar minimum⁸⁰) and the ground state destabilized. When converging our results further using a large basis set (*aug-cc-pVTZ*¹¹⁸), the energies of 4.22 and 5.36 eV compare well with the CASPT2 values. Differences of 0.1–0.2 eV are within the accuracy of ADC(2), which has mean error of 0.22 eV.⁵ The S_3 state (as well as S_2) is rather sensitive to the perturbative double excitations as shown by the CIS/CIS(D) diagnostics.⁸⁰ Given that ADC(2) treats the double excitations only approximately, the energy of the two states ($B \pi\pi^*$) may be slightly overestimated. On the other hand, the CASPT2 excitation energies of the two bright $\pi\pi^*$ states are anticipated to be highly sensitive to the active spaces, basis sets *etc.*^{87,89,91} Andrzejak and Witek⁹¹ demonstrated that earlier CASPT2 computations^{87,89} were

erroneously predicting the two states as quasi-degenerate, whereas the actual gap is as large as 1 eV when using large basis sets and a variety of active spaces.

Finally, we show the absorption cross sections (Figure 3.2) for both thiophene and bithiophene computed with the semiclassical Wigner distribution approach at the ADC(2)/def2-SVPD level. The simulated spectra confirm that the band maxima are slightly red-shifted with respect to the vertical excitation energies. The spectra were decomposed into contributions from different states, S_1 (blue) and S_2 (red) for thiophene, S_1 (red) and $S_3 + S_4$ (blue) for bithiophene. The color code is consistent with the one used in our previous study,⁸⁰ and reflects the character of the $\pi\pi^*$ states. The energy windows used for the sampling of the initial conditions of the molecular dynamics simulations are also indicated.

3.3.2 Excited state dynamics of thiophene

In contrast to the earlier CASSCF surface hopping study,⁷⁷ which was applied only from the first excited state, the present dynamics is initiated from both S_1 and S_2 , which have comparable intensities (Figure 3.2a). Initial conditions were chosen randomly from the narrow energy windows approximately centered at the vertical excitation energies. A swarm of 100 trajectories was initiated from both states and nonadiabatic couplings were computed for the first four excited states. Since no couplings were computed between the ground (MP2) and excited (ADC(2)) states, the dynamics was terminated at their crossing point. The sole consideration of the excited state dynamics suffices to identify the major deactivation paths. The main underlying assumption is that in the crossing region electronic population is transferred to the ground state while recurrences represent only a minor effect. Similar protocols were also adopted in earlier ADC(2)^{37,86} and TDDFT^{61,65} surface hopping studies.

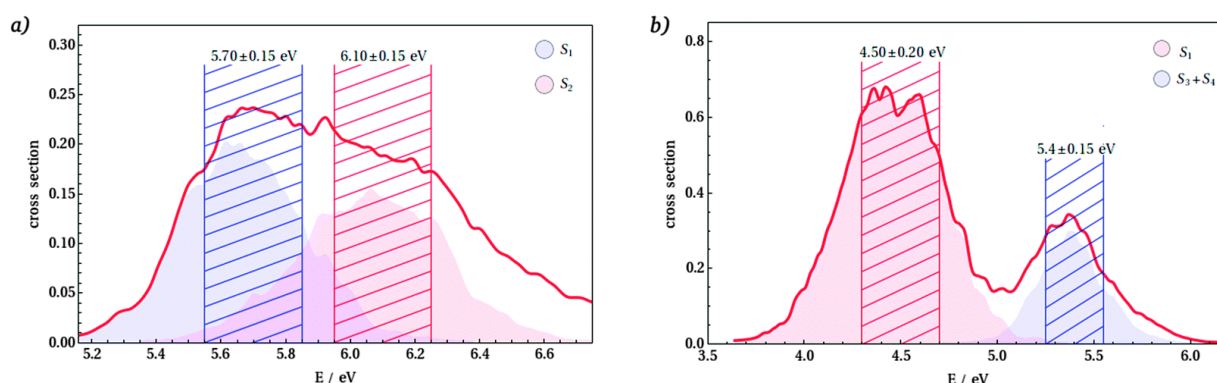


Figure 3.2 Photoabsorption spectra computed from a Wigner distribution of: (a) thiophene and (b) bithiophene at ADC(2)/def2-SVPD level.

Two internal conversion mechanisms characterize the thiophene photochemistry: the ring opening due to the CS bond cleavage and the ring puckering arising from the out-of-plane distortions. The ring opening is favored and accounts for 83% and 70% of the deactivation pathways from S_1 and S_2 respectively, while the rest of the trajectories proceed *via* ring puckering. The energy profiles of four illustrative trajectories are shown in Figure 3.3, although alternative scenarios are possible. In Figure 3.3a, the molecule is initially excited in the S_1 state having a dominant $\pi_2\pi_4^*$ character. The trajectory evolves on the S_1 potential energy surface, which eventually changes into a $\pi_3\pi_4^*$ and $\pi_3\sigma^*$ character. This is followed by the elongation of the CS bond distance and an increase of the ground state energy, which after an approximate total time of 80 fs crosses the first excited state. More detailed analysis of this trajectory (as well as the one shown in Figure 3.3c) can be found in ESI. The second trajectory (Figure 3.3b) was initiated in the S_2 state with a dominant $\pi_3\pi_4^*$ character. Surface hopping to $S_1(\pi_2\pi_4^*)$ occurs around 15 fs leading finally to the ring opening owing to the antibonding $\pi_3\sigma^*$ nature of the S_1 potential energy surface. Note that the major dynamical changes occur both nonadiabatically (*i.e.*, surface hopping due to the strong nonadiabatic coupling) and adiabatically (*i.e.*, within the same adiabatic state) by a change in electronic character. The latter suggests that the corresponding diabatic states are

strongly coupled through nondiagonal matrix elements of the electronic Hamiltonian. Note however that in the present context the concept of diabatic states is used in a rather non-mathematical way to assign the main orbital configurations of the excited states. Akin to the first trajectory, Figure 3.3c shows a system evolving adiabatically on the S_1 potential energy surface. Initial $\pi_2\pi_4^*$ character changes into $\pi_3\pi_4^*$ leading to the ring puckered intersection with the ground state. The final structure is characterized by a deplanarized ring and a sp^3 hybridization of the carbon atom adjacent to sulfur. The last example (Figure 3.3d) features several hops but the running state preserves the main $\pi_3\pi_4^*$ character. The trajectory ends with the ring puckering after a total time of roughly 100 fs. Since the ring puckering occurs at the crossing between the $\pi_3\pi_4^*$ state (B_2 irrep in C_{2v} point group) and the ground state, it is not surprising that its probability increases for the trajectories initiated in the S_2 state. However, the higher energy window, which is closer to the antibonding $\pi\sigma^*$ state, also facilitates ring opening. Overall, the deactivation is not strongly dependent on the initial excitation energies although puckering becomes more important at higher energies. The ultrafast decay was accomplished by all 200 computed trajectories within a time significantly shorter than the maximal time set to 400 fs.

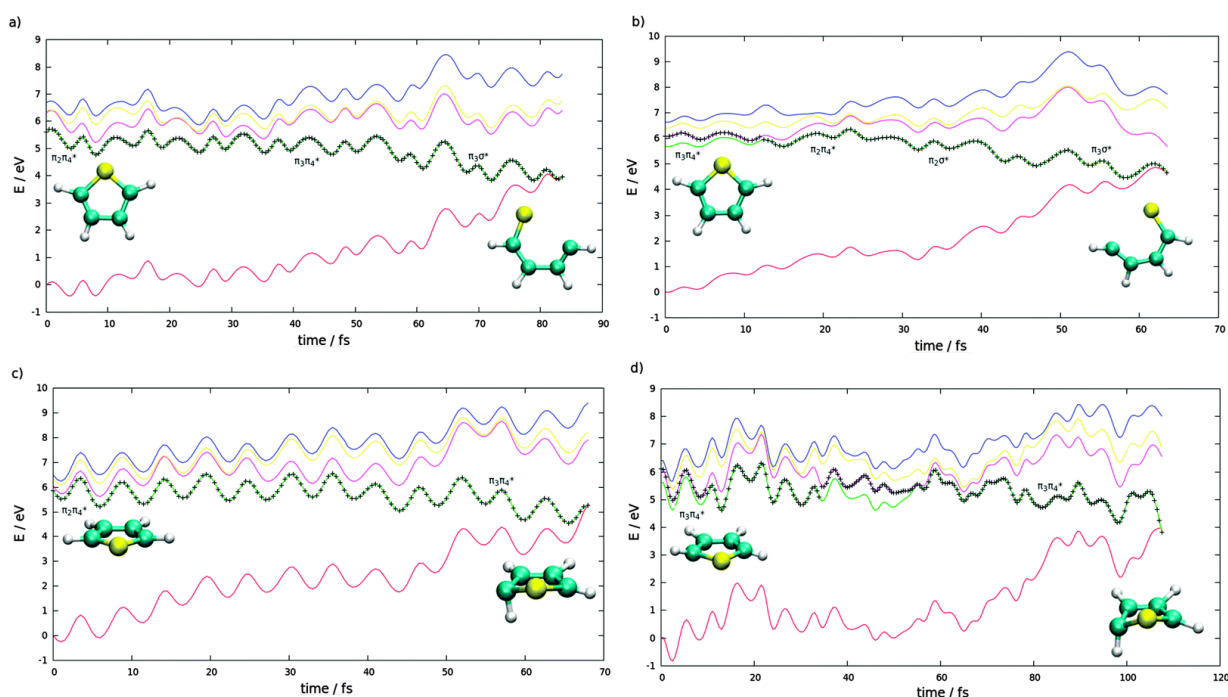


Figure 3.3 Energy profiles of the four trajectories following the (a, b) ring opening and (c, d) ring puckering mechanism. Trajectories were initiated on (a, c) S_1 and (b, d) S_2 potential energy surface. The time evolution of the ground and four lowest excited adiabatic singlet states are displayed in color, whereas the running state is indicated in black. The energies are plotted relative to the initial ground state energy (0 fs). Molecular geometries at the initial and final step of the dynamics are given for each trajectory. The figures on the left are “adiabatic” while those on the right are nonadiabatic, *i.e.*, with surface hops.

Although specific trajectories may indicate possible relaxation paths that molecules can undergo, in surface hopping properties should be monitored over the full swarm of trajectories, which is expected to mimic the dynamics of a nuclear wavepacket (within a semiclassical approximation⁴⁶). In Figure 3.4 we show a time evolution of the average CS bond lengths (as both CS bonds in thiophene can break) for trajectories initiated in each of the two states (S_1 and S_2). The final steps representing the crossing between the first excited and the ground states are given in black. In both cases, the initial elongation of the CS bond occurs already in the $\pi\pi^*$ states owing to their nature. This motion efficiently couples with the higher $\pi\sigma^*$ state, resulting in the ultrafast decay of most of the trajectories before 100 fs. The rest of the trajectories resists up several hundred femtoseconds. This observation is consistent with the earlier CASSCF dynamics⁷⁷ where a time constant of 65 ± 5 fs was obtained for 80% of the trajectories. However, a non-negligible portion of the

trajectories terminates with the ring puckering, which is represented by the black dots in the lower part of the graphs. The timescales on which the two mechanisms operate are indistinguishable.

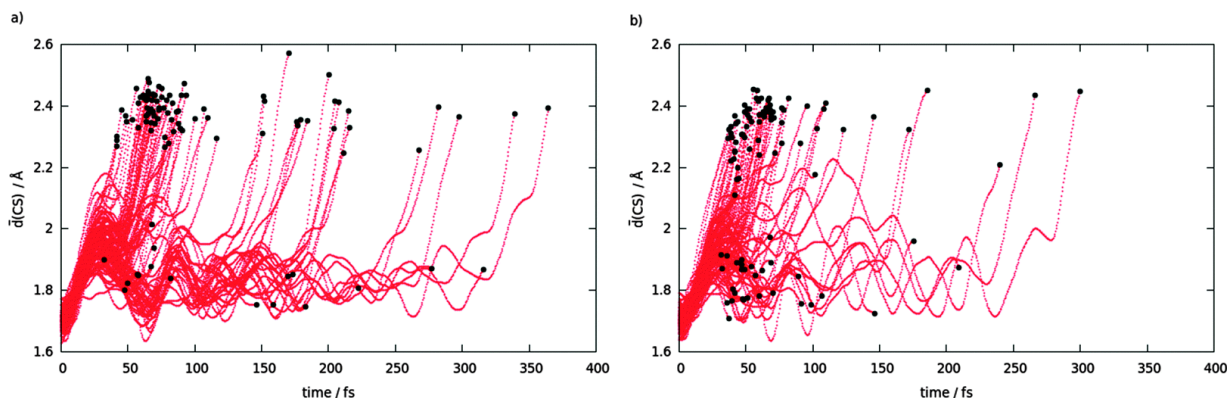


Figure 3.4 Time evolution of the average CS bond lengths for trajectories initiated on the (a) S_1 and (b) S_2 potential energy surface. The steps of the nonadiabatic dynamics are represented by the red dots while the final points are marked in black.

The out-of-plane motions of the hydrogen atoms next to sulfur (*i.e.*, the δ_{CCCH} dihedral angle) can also distinguish the puckering from the ring opening and is chosen as another collective variable (the average value was considered for both H atoms). Figure 3.5 demonstrates how do the swarms split into two regions, representing two internal conversion mechanisms. The geometrical parameters of the CASPT2⁷⁸ optimized S_1/S_0 conical intersections and S_1 minimum are also plotted for comparison. The scattering of dots representing crossing points from the simulations is mainly due to the dynamical effects. As noted by Tully,²⁹ the actual probability that an arbitrary trajectory will pass exactly through a conical intersection is equal to zero. The proximity of a conical intersection is more relevant as it represents the region of small energy splitting and large nonadiabatic couplings, resulting in a high probability of nonadiabatic transition. The intersection region seems to be qualitatively well described by ADC(2). However, the ring opening appears at somewhat lower CS distances (~ 3 Å) as compared to the optimized CASPT2 conical intersection (3.4 Å; in Figure 3.4 only the average value is shown). Stenrup⁷⁸ also reports a shallow minimum very close to the ring opened conical intersection, which we do not find at the ADC(2) level. Such discrepancies could be expected given that ADC(2) is not very accurate for distorted geometries close to the conical intersections with the ground state. The method lacks double excitations and is based on the MP2 single reference ground state. The latter aspect is illustrated by the rapid increase of the D1 diagnostic as the trajectory approaches the crossing with the ground state (see ESI). The analysis of the D1 parameters also shows that in the course of the simulations, the molecule indeed spends most of the time in the region where the method is reliable. Out-of-plane distortions also play important role in the excited state dynamics of thiophene as indicated by the region with a high density of red points, which coincides with the nonplanar S_1 minimum. Such motions also prompt ultrafast deactivation *via* ring puckering. Stenrup⁷⁸ distinguishes two types of puckering, one mainly on the sulfur atom (CI b) and another on the carbon atom (CI c). The analysis of our geometries reveals that only several crossing points are associated with the conical intersection of the c type, while most of the structures resemble to the conical intersection of type b (see insets in Figure 3.3). Furthermore, we find another type of puckering where distortion occurs on C atom opposite to S, although the corresponding trajectory was not part of the original set of calculations (see ESI).

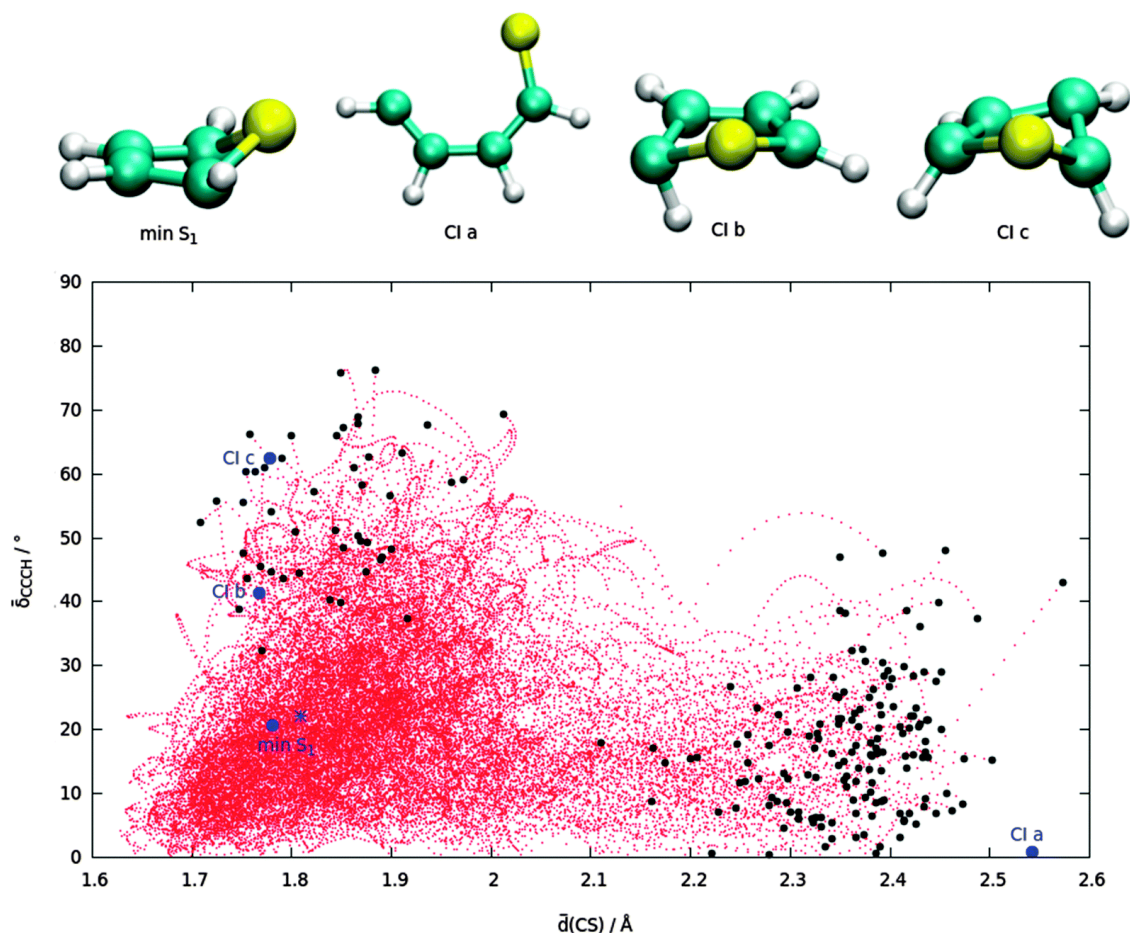


Figure 3.5 Evolution of the average bond length distances and CCH dihedral angles of all 200 thiophene trajectories. The steps of the dynamics are represented in red, while the final crossing steps are marked in black. The dihedral angle was redefined in the range between 0° and 90° . The structures associated with the CASPT2-optimized conical intersections and S_1 minimum were taken from the ESI of ref. [78] and are represented in blue. For comparison, the S_1 minimum obtained at the ADC(2)/def2-SVPD level is shown as a blue asterisk.

The average populations of the individual excited states shown in Figure 3.6, mirror the timescales on which the internal conversion processes occur. As noted earlier, it is assumed that the molecule will relax in the ground state after the crossing. For the first set of trajectories initiated in S_1 (Figure 3.6a), the decay seems more complex than an exponential but the appearance of a small knee at around 100 fs, might be due to a sampling issue. The overall decay time is nevertheless calculated from the population fitted to a single exponential function $f(t) = \exp[-(t-t_d)/t_e]$ where t_d is a latency time and t_e the exponential time constant. For the S_1 dynamics $t_d = 18$ fs and $t_e = 93$ fs so that total time constant ($t_d + t_e$) is equal to 111 fs. Based on both pump–probe photoelectron spectroscopy and theoretical modeling, the lifetime provided by Weinkauff *et al.*⁷⁵ is expected to be in the 100 fs regime, which is in line with our results. Note, however, that direct comparison is restricted since the experiment corresponds to an excitation to the lowest S_1 vibrational level. The trajectories initiated on the second excited state (Figure 3.6b) are characterized by a rapid depopulation of S_2 state occurring in 10 fs. Fitting of the assumed S_0 population to an exponential function leads to $t_d = 16$ fs and $t_e = 57$ fs. The shorter total time constant is in line with the unbound nature of the $B_2 \pi\pi^*$ state and the larger internal energy associated with the higher energy window.

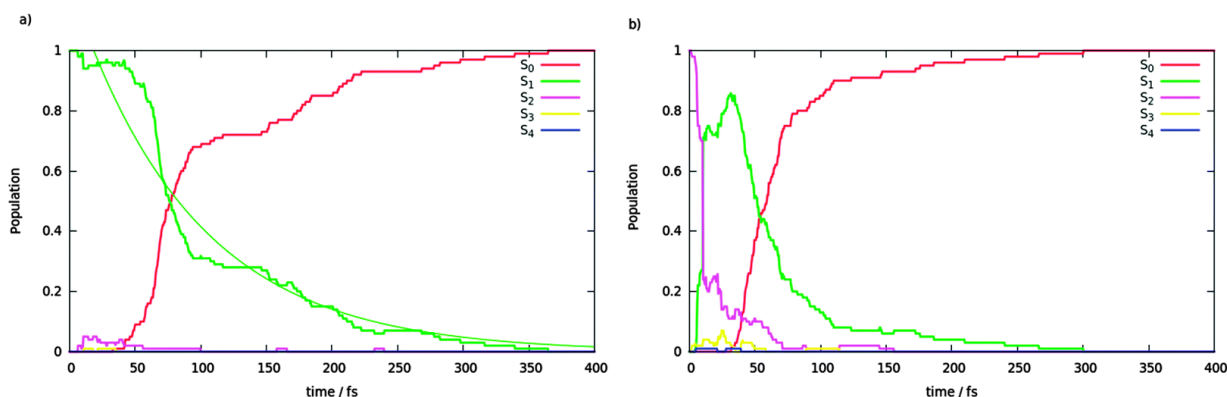


Figure 3.6 Time evolution of the average populations of the ground and first four singlet excited states for the trajectories started in (a) S_1 and (b) S_2 state.

Overall, our dynamic picture complements the “static” computations of Marian *et al.*⁷⁶ and Stenrup.⁷⁸ An obvious advantage of *ab initio* nonadiabatic dynamics is the unbiased exploration of the potential energy surfaces, the treatment of nonadiabatic effects and the insight into the timescales. The existence of the ring puckering mechanism is in major disagreement with the CASSCF surface hopping study of Cui and Fang,⁷⁷ in-line with the TDDFT dynamics of Fazzi *et al.*,⁷⁹ who also predicted both mechanisms. At this point, it is hard to say why CASSCF differs, especially since the authors did not provide the corresponding excitation energies. However, results from the literature show that CASSCF can give various values, depending on the active space, basis set and other parameters. For instance, A_1 and B_2 states ($\pi\pi^*$) were found to be nearly degenerate in ref. [116], whereas in work of Roos *et al.*¹¹⁹ B_2 state is placed 1.7 eV above A_1 . Alternatively, Stenrup⁷⁸ notices that CASSCF does not provide a balanced description of the two $\pi\pi^*$ states and the perturbational correction is necessary.

3.3.3 Excited state dynamics of bithiophene

Despite the considerable interest in small oligothiophenes, the excited state dynamics of bithiophene was only studied experimentally,^{120,121} with the exception of TDDFT simulations mentioned previously.⁷⁹ The lowest excited singlet state of bithiophene was shown to decay in a relatively long time (lifetime 51 ps)¹²¹ and the population transfer was attributed to an intersystem crossing with an efficiency of 0.99.^{74,121} Note that the experiments^{74,121} were performed in dioxane and benzene. While several quantum chemical studies dealt with singlet and triplet excited states of bithiophene,^{74,88,89,122–124} the most recent one of Weinkauff *et al.*⁹⁰ (including oligothiophenes of chain lengths 2 to 6) attributes efficient intersystem crossing to a transition from the S_1 state to the lower triplet state T_2 , which subsequently transfers its population to the T_1 state. We here compute the excited state dynamics of bithiophene by means of surface hopping trajectories. Our primary focus is the intrinsic (gas phase) dynamical properties of the singlet excited states, while the interplay with the triplets is only considered through single point computations. The full surface hopping dynamics including both singlet and triplet states, and the possibility of the singlet–triplet transitions will be considered in future studies. One of the goals is to establish the similarity between the dynamics of thiophene to its simplest oligomer. As noted before, two bright $\pi\pi^*$ (B) states dominate the low-energy photoabsorption spectrum of bithiophene, giving rise to two distinct peaks. Our simulations were initiated in both $\pi\pi^*$ states. The initial conditions for the surface hopping dynamics from S_1 were sampled from the lower energy window shown in Figure 3.2b. In contrast to thiophene, which experiences very fast deactivation, bithiophene S_1 dynamics is substantially more stable. Out of 50 trajectories computed with a total time of 500 fs and with nonadiabatic couplings between the first four excited states, 71% of the trajectories were stable, while the rest underwent a ring opening (see Figure 3.7a). We observed no equivalent of the ring puckering mechanism. In the illustrative trajectory (Figure 3.7a) leading to the ring opening mechanism system remains in the same state for about 400 fs. A surface hopping to the antibonding $\pi\sigma^*$ state occurs after around 420 fs, followed by a crossing with the ground state. The transition to the $\pi\sigma^*$ state is alternatively realized by an adiabatic change of character. The CS bond cleavage is therefore due to the lowering of the $\pi\sigma^*$ state from the higher energy manifold.

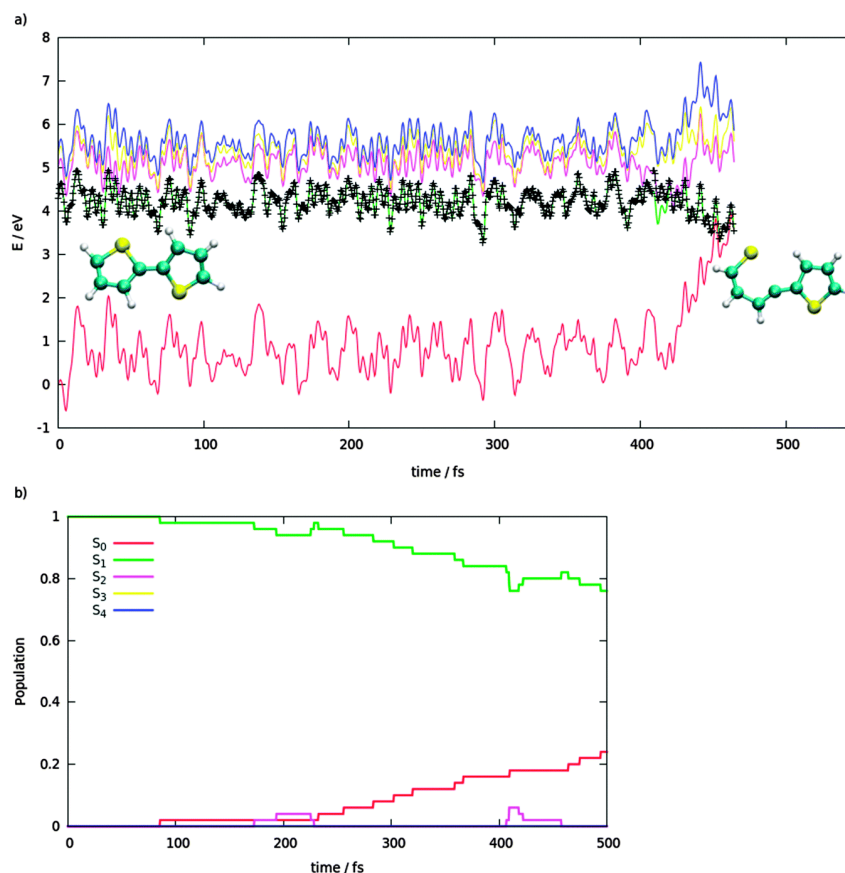


Figure 3.7 (a) A representative ring opening trajectory showing the time evolution of the ground and four lowest excited adiabatic singlet states. The running state is indicated in black. The energies are plotted with respect to the initial ground state energy (0 fs). The molecular geometries at the initial and final step of the dynamics are shown. (b) The time evolution of the average populations of the ground and first four singlet excited states for the surface hopping dynamics of bithiophene initiated on the S_1 potential energy surface.

Figure 3.7b shows that the dynamics is dominated by the S_1 state, while the small population of S_2 is mainly due to the hops to S_2 in the ring opening type trajectories. Although our dynamics study is based on a relatively small number of trajectories and short simulation times, the rough estimate of the S_1 lifetime is 1.8 ps with a latency time of 0.1 ps. This is certainly not in a good quantitative agreement with the experimental lifetime (51 ps).¹²¹ At this stage, we cannot exclude that the ring opening is an artifact of our computations or that the solvent inhibits this process. TDDFT simulations⁷⁹ similarly predict that small fraction of trajectories relaxes by CS bond cleavage. Nevertheless, the crucial finding is that bithiophene evolving in S_1 is much more stable, which opens the possibility for an efficient ISC. The relative stability with respect to the internal conversion mechanisms may be attributed to the energy lowering of the S_1 $\pi\pi^*$ state (being even more pronounced for larger oligothiophene chains) implying that the respective dynamics is less affected by the higher manifold of states. Non-polar organic solvents typically stabilize S_1 for 0.2–0.4 eV.⁹⁰ In general, the absence of internal conversion is fundamental for any real-life optoelectronic applications, since conversion of (absorbed) energy into geometrical rearrangements such as bond breaking would be detrimental to the device.

The energies of four lowest triplet states vary through the dynamics on the S_1 (green) potential energy surface (Figure 3.8a). Evidently, the trajectory running in S_1 experiences multiple crossings with the T_2 state (black). The role of the higher triplet states is smaller but should not be disregarded. The distribution of T_x – S_1 ($x = 1$ –4) energy gaps between the four triplets and S_1 state (Figure 3.8b) shows that T_2 has the largest overlap with S_1 . As S_1 has a planar minimum, group theory restricts the spin–orbit coupling matrix elements between S_1 and T_2 to be zero for the minimum geometry.

Therefore, the out-of-plane motions could prompt singlet–triplet transitions, as noted before.⁹⁰ Such motions are highly active during the S_1 dynamics. The minimum ground state geometry exhibits large inter-ring dihedral angle (experimental 148° ,¹²⁵ in this work 150°) and is slightly bent (molecule does not possess center of inversion). After vertical excitation to S_1 , which is characterized by a planar C_{2h} minimum, the out-of-plane oscillatory motions become significant. Nevertheless, the truthful interpretation of the experimental observation would require additional excited state dynamic studies including spin–orbit couplings and environment effects. In the case of thiophene, the possibility of ISC was invoked by Marian *et al.*,⁷⁶ although it was considered less probable due to the ultrafast internal conversion paths and modest spin–orbit couplings.¹²⁶ On the other hand, weak phosphorescence was experimentally detected¹²⁷ (though not in another study⁷⁵) and that question is certainly awaiting additional theoretical investigation. The development of surface hopping with states of different multiplicities is still at its infancy,¹²⁸ but alternative schemes such as SHARC (surface hopping with arbitrary couplings) of González *et al.*¹²⁹ and generalized trajectory surface hopping of Cui and Thiel¹³⁰ exist. One discouraging feature is that multireference methods might be overly expensive (and even challenging⁹¹) for bithiophene, and even more for larger oligomers. Computationally cheaper correlated single reference methods such as ADC(2) represent an appealing alternative assuming that spin–orbit couplings will become available in standard quantum chemical codes. Here we only analyze several crossing points (S_1 – T_2) for the trajectory shown in Figure 3.8a. Based on the approximate TDDFT method we computed spin–orbit coupling matrix elements in the range from 3 to 45 cm^{-1} , the latter values being sufficient for effective ISC over the long time.

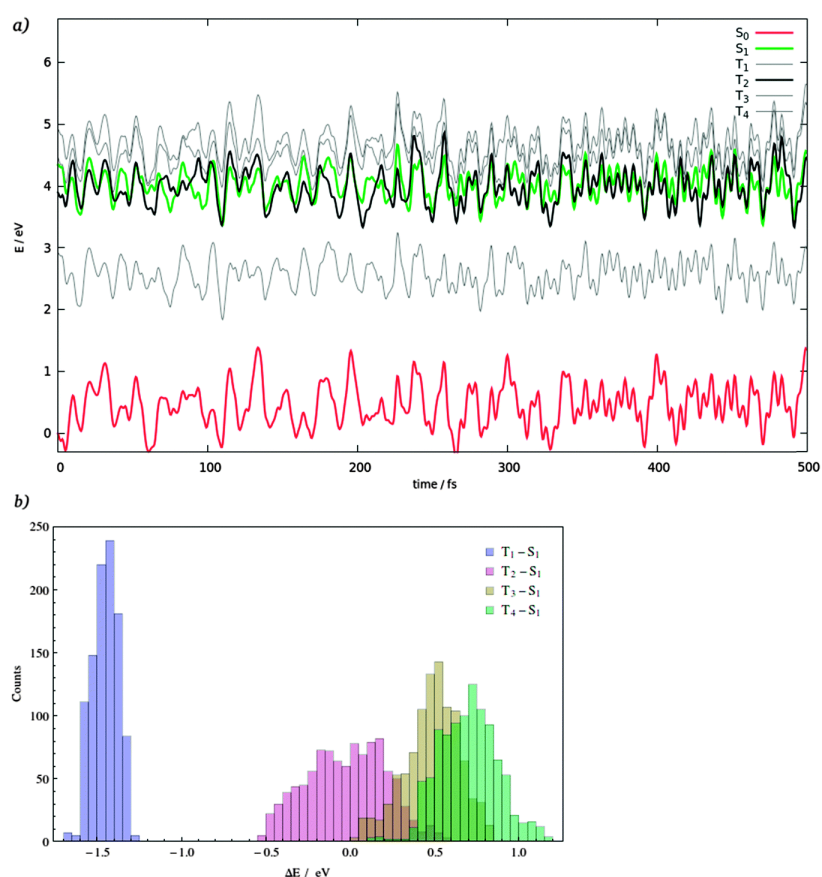


Figure 3.8 (a) Variation of the electronic energies of the four lowest triplet states of bithiophene (T_1 , T_3 , T_4 gray, T_2 black) for a representative trajectory evolving on the S_1 (green) potential energy surface. The energies are plotted with respect to the initial ground state (red) energy. (b) Histogram of the energy gaps between the four triplets and S_1 state based on thousand steps taken from the trajectory in (a).

The final dynamic trajectories were initiated at the higher $\pi\pi^*$ states (with the initial conditions randomly sampled from the window indicated in Figure 3.2). To ensure that the dynamics starts at the bright state, only the states with large oscillator strengths ($f > 0.05$) were accepted as a proper initial condition. By applying this criterion, a total of 50 trajectories were initiated in S_2 (1), S_3 (36), S_4 (12) and S_5 (1), with the number of respective trajectories indicated in parenthesis. The trajectories were propagated for 500 fs and nonadiabatic couplings were computed between first six excited states. As expected, the proximity of the $\pi\sigma^*$ state, results, for most of the trajectories (82%), in a relaxation to the ground state *via* ring opening. The rest populates S_1 state and remains stable in the course of the dynamics. No analogue of ring puckering was found as for the lower energy window. It is also worth mentioning that the ring opening was observed almost exclusively (for both windows) for the breaking of the “inner” CS bond (next to the CC linker). This is consistent with the localization of the σ^* orbital depicted in Figure 3.1b. Only a single trajectory initiated from the higher energy window experienced the dissociation through the “outer” CS bond, forming the less stable primary carbon radical. The fitting of the assumed ground state population increase (Figure 3.9) through an exponential function leads to an effective time constant of 270 fs, corresponding to an ultrafast deactivation process. Two trajectories were discarded from the analysis as they ended with a direct crossing between S_2 and the reference state (S_0), with S_1 being below the reference state (ADC(2) is not reliable in the regions crossing the ground state).

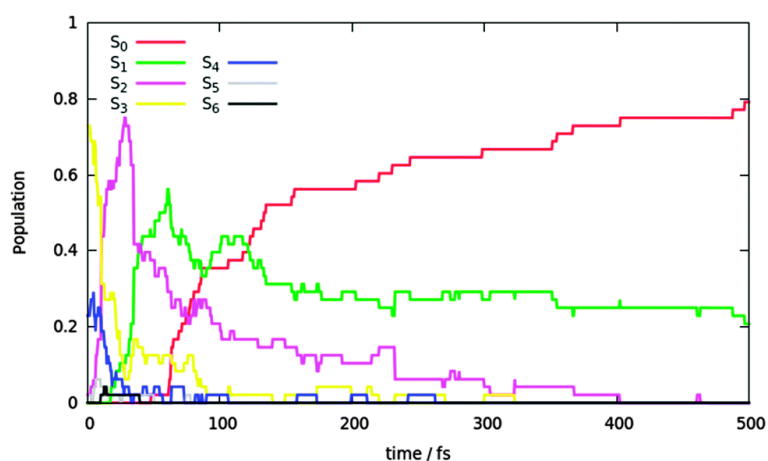


Figure 3.9 Time evolution of the average populations of the ground and first six singlet excited states of bithiophene for trajectories started at the higher energy window (see Figure 3.2).

3.4 Conclusion

The accurate theoretical description of the photochemical processes of thiophene-based molecules may promote our ability to address the most relevant questions associated with applications in the field of organic electronics. We presented a detailed and comprehensive surface hopping molecular dynamics study of thiophene and bithiophene using the algebraic diagrammatic construction to second order method. Our results stress that the ring puckering mechanism plays a critical role in the deactivation process from the S_1 potential energy surface of thiophene. This mechanism operates on the same timescale as the more representative and previously identified ring opening process. In contrast, the ring opening was the only deactivation mechanism identified from the excited state dynamic trajectories of bithiophene. Furthermore, the lowest excited state of bithiophene was found to exhibit an enhanced photostability illustrated by a much longer lifetime. Our computations also illustrate that correlated single reference methods such as ADC(2) represent an appealing alternative to expensive quantum chemical methods as CASPT2, and has the potential to replace the often used, but more approximate, TDDFT, at least for the small and middle-sized molecular systems.

Chapter 4 How Does Tetraphenylethylene Relax from its Excited States?

The Chapter is published as: Prlj, A., Došlić, N.; Corminboeuf, C. *Phys. Chem. Chem. Phys.* **2016**, *18*, 11606-11609.

Aggregation-induced emission (AIE)^{131–135} molecular systems are defined as having weak or non-emissive behaviour in dilute solutions or the gas phase while they emit strongly in aggregate solutions. These systems now receive considerable interest owing to their potential uses in organic light emitting diodes and in bio/chemosensing. Tetraphenylethylene (TPE) is a prototypical example of a system displaying AIE: its fluorescence depends upon the degree of conformational flexibility, with restricted conformers displaying higher fluorescence. Thus, a route to improve aggregation and emission properties is the addition of organic,^{136–139} metal–organic,^{140–142} ionic,^{143,144} and other substituents onto the TPE frame. Despite a considerable amount of experimental research, reliable studies aiming to unravel the photochemistry of TPE are lacking. Here, we explore the ultrafast deactivation mechanisms responsible for fluorescence quenching in isolated TPE (*i.e.*, in gas phase).

The nonradiative decay of TPE has been interpreted in terms of an internal conversion associated with an ethylenic twist,^{145–147} albeit several studies have hinted that phenyl ring torsions may also play a significant or even primary role.^{148,149} However, no definitive geometry interpretation has been given for the decay process, yet this information would be quite beneficial for the rational design of novel TPE-based fluorophores. The present work seeks to gain atomic level insights into the excited state dynamics of TPE through the use of a mixed quantum-classical formalism³⁴ (see details in the Computational section) based on trajectories that represent the motion of the molecular system upon photoexcitation. The same methodology has been previously employed^{150–153} to identify radiationless decay mechanisms in organic molecules that yielded valuable insights for interpreting experimental data.

Despite an on-going debate,^{154–156} the deactivation of ethylene from its first excited state (referred to here as an ethylenic twist) is a typical example of relaxation through a conical intersection (CI) seam.^{58,59} Excitation to the S_1 state (HOMO \rightarrow LUMO) causes a reduction in the C=C bond order, which initiates the twisting dynamics. This motion (along with the CH bond dynamics) stabilizes the first excited state (S_1) and destabilizes the ground state (S_0), ultimately causing the two states to become degenerate (*i.e.*, the crossing referred to as CI). The dynamic process goes through (or in vicinity of) the CIs, which explains the ultrafast internal conversion (IC) from the excited to the ground state, as well as the subsequent *cis–trans* photoisomerization (see Figure 4.1a). The excited state dynamics of TPE* (in the time interval between the Franck–Condon region and the S_1/S_0 CI, which is our primary focus) can be, in part, described by a similar picture (Figure 4.1b). Indeed, the trajectory shown in Figure 4.2a confirms that TPE* can also deactivate *via* an ethylenic twist. The system, after initial excitation to the S_1 state (red curve, lower panel), evolves adiabatically on the same potential energy surface. Simultaneously, twisting of the central CC bond (upper panel) strongly destabilizes the ground state (magenta curve, lower panel). After ~ 1 ps the S_1 state becomes nearly degenerate with the ground state and eventually reaches the CI between the S_1 and S_0 states. The system then may undergo an ultrafast IC to the ground state. Surprisingly, only 3 out of 60 computed trajectories followed this specific deactivation channel that is considered to be the main pathway. Importantly, this implies that other, more efficient IC mechanisms exist that may involve phenyl ring dynamics.

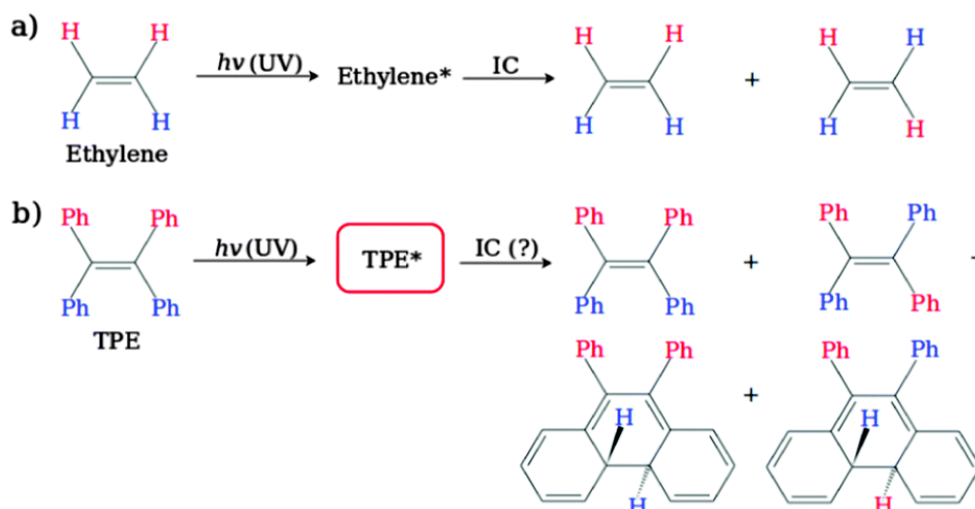


Figure 4.1 Photoexcitation and (assumed) photoproducts of (a) ethylene and (b) TPE upon internal conversion.

A search for alternative mechanisms revealed that 75% of the trajectories (45/60) proceed through photocyclization (Figure 4.2b). The fact that this particular mechanism has not been considered as a possible decay pathway is rather curious, particularly considering its existence in the structurally similar (*cis*-) stilbene^{59,157,158} and the identification of biphenyl dihydrophenanthrene as a reaction intermediate in the photo-oxidative reaction of TPE.¹⁵⁹ Nonradiative decay *via* cyclization explains, for instance, why *ortho*-terphenyl does not fluoresce, while the *meta*- and *para*-isomers do fluoresce.^{160–162} Woodward–Hoffmann rules predict a conrotative electrocyclicization of the excited 6π -electronic system for the photocyclization process. The phenyl-ring torsions bring the S_1 and S_0 close together (Figure 4.2b, lower panel) leading the system to the CI (characteristic hexagonal arrangement of the C atoms highlighted in red). In contrast, restricting the torsional motion would, in principle, block the nonradiative decay and promote the radiative pathways. The extent to which various photoproducts are formed *via* nonradiative relaxation to the ground state (opened or closed ring TPE, as in Figure 4.1b) essentially depends upon the precise CI topology encountered by the trajectory. If formed, experimental characterisation of the closed-ring TPE (*i.e.*, biphenyl dihydrophenanthrene) in its ground state would constitute definitive proof of photocyclization. Yet, the closed form is expected to be photochemically unstable (*i.e.*, in its excited state) and reopens in an ultrafast photoinduced process (see electronic supporting information, ESI) under visible light. Overall, the photodynamical cycle of TPE is rather complex but there is little doubt that photocyclization plays a key role.

Of the remaining trajectories: one followed the fulvene-like cyclization (ESI for details), representative of a minor deactivation channel, while the remainder (12/60) persist in the excited states with no change through the length of the simulation. Figure 4.3 shows a time evolution of the twist angle θ (as in Figure 4.2a) for the ensemble of trajectories. Red/blue/green lines represent molecules in $S_1/S_2/S_3$, respectively, whereas S_1/S_0 crossing points are indicated by black dots. The cyclization dynamics is easily distinguished from the ethylenic twist by its modest θ values. The phenyl rings are initially close to one another and cyclization dominates. As the twisting motion around the central CC bond proceeds, the cyclization becomes inaccessible and another decay channel (ethylenic twist) opens. The overall oscillatory nature of the dynamics shows that the interplay between both deactivation mechanisms (cyclization and twist) leads to the radiationless decay of TPE.

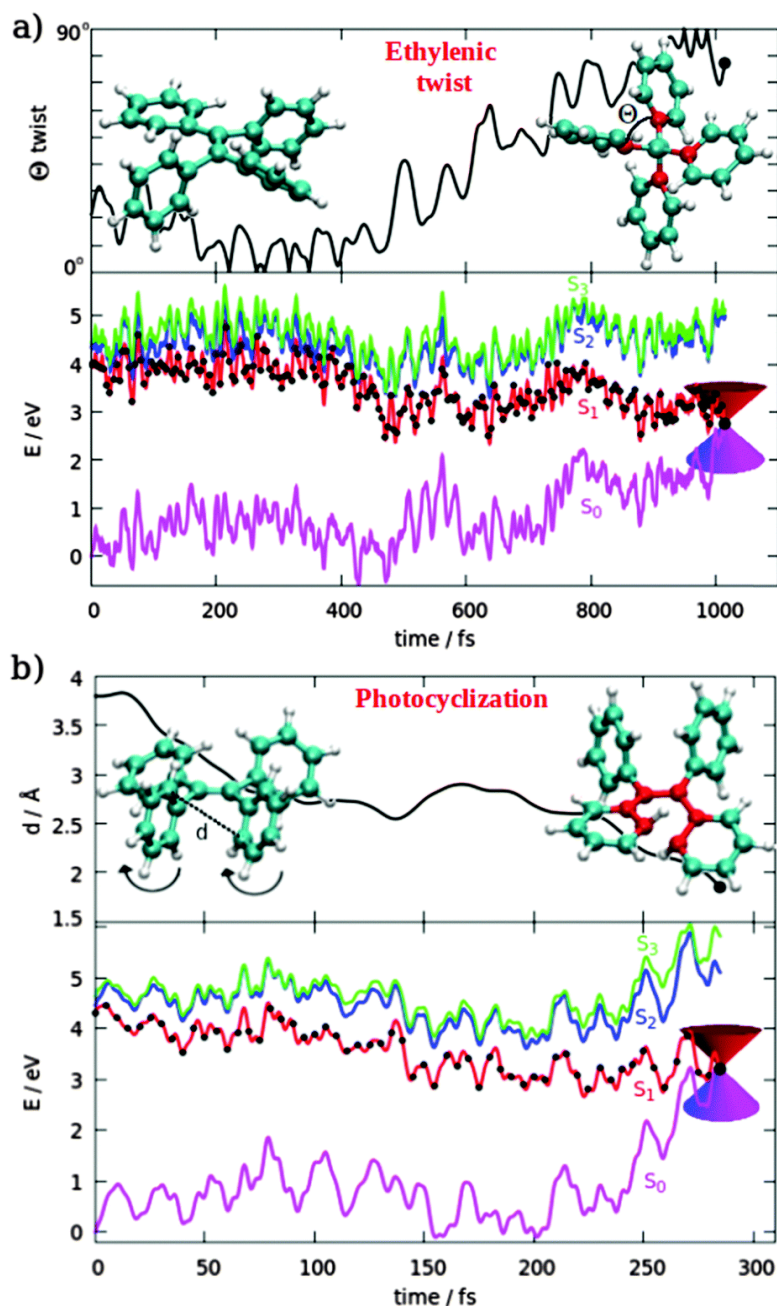


Figure 4.2 Relevant geometrical parameters (upper panel) and electronic state potential energies (lower panel) as a function of time for two representative trajectories showing (a) the ethylenic twist and (b) the photocyclization process. The time evolution of the ethylenic twist is monitored by the torsional angle Θ (defined in the $[0 : 90^\circ]$ range), whereas for photocyclization is described by the relevant CC distance. Potential energies of $S_0/S_1/S_2/S_3$ are shown in magenta/red/blue/green curves respectively, while the actual (running) electronic state is indicated in black. All the energies are relative to the initial (0 fs) S_0 energy. Initial (0 fs) and final (*i.e.*, close to CI) molecular structures are shown. The trajectories are computed at the PBE0/def2-SVP level (ESI for details).

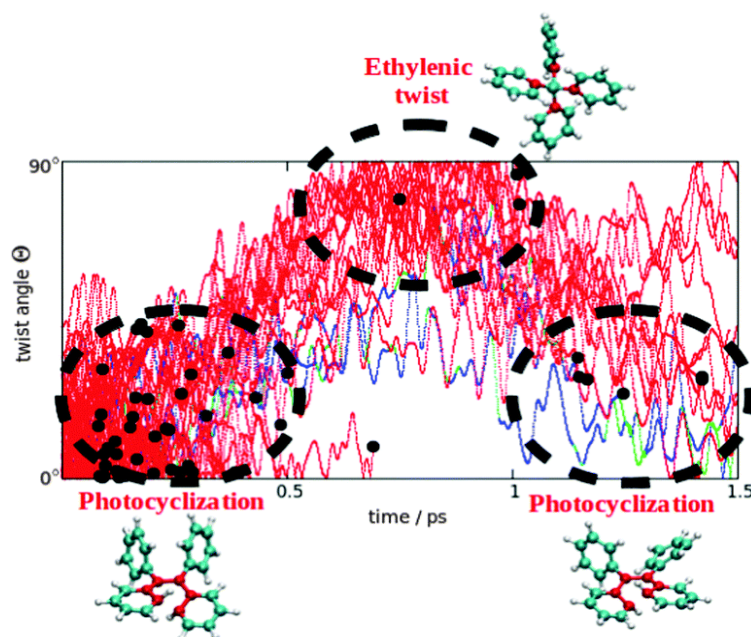


Figure 4.3 Time evolution of the Θ twist angle (see Figure 4.2a) for 60 trajectories. The trajectories (lines) are colored according to the populated state ($S_1/S_2/S_3$ in red/blue/green) while the black dots indicate the S_1/S_0 crossings, *i.e.* the regions of population transfer from the excited to the ground state.

From the general perspective of aggregation-induced emission, the fluorescence quenching in various fluorophores has traditionally been assigned to the photophysical energy dissipation caused by propeller-like rotations of the side groups, rather than to photochemical decay as shown here. Restricted intramolecular rotations (RIR) in the aggregate were invoked as an explanation for the observed induced emission.^{133–135} However, very recently this picture has been challenged,^{163,164} at least for systems possessing accessible conical intersections. Static QM/MM investigation of the CIs of a related molecule (*i.e.*, diphenyldibenzofulvene) in the crystal phase has shown that induced emission can be explained by the inaccessibility of the CI seam. Although we did not account for the effects of aggregation, we have clearly demonstrated that CIs play a key role in the photochemistry of the prototypical TPE (though the accessibility of the CIs is indeed related to the intramolecular rotations). The present findings will be of considerable value for future interpretation and understanding of the AIE properties.

4.1 Computational details

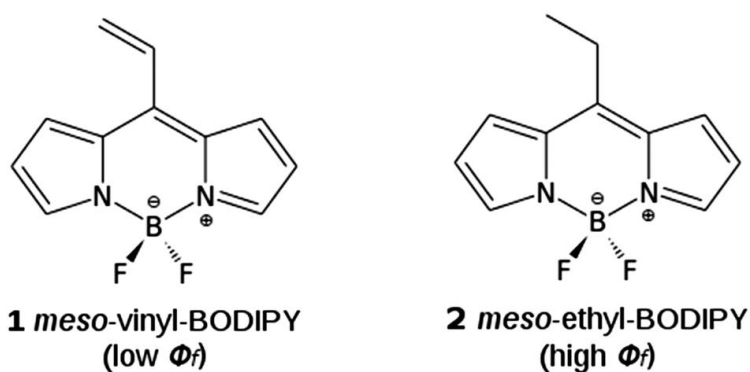
Full details can be found in ESI. We used a mixed quantum-classical trajectory surface hopping method based on Tully's fewest switches scheme³⁴ (for implementation details see ref. [165]). 60 trajectories were computed with the initial conditions taken from the Boltzmann ensemble at 300 K and assuming the vertical excitations to the first excited singlet state, S_1 . The electronic structure was described using linear-response time-dependent density functional theory (TDDFT) within the Tamm–Dancoff approximation.^{11,19,166} Despite the typical challenges associated with the description of the excited states of unsaturated organic molecules,^{80,167,168} earlier benchmark studies have shown that TDDFT can describe both photoisomerization and photocyclization qualitatively well.¹⁶⁹ Consequently, we intentionally do not deliver a detailed quantitative interpretation (*e.g.*, yields, lifetimes) but rather focus on the qualitative TDDFT picture. Note also that in the realistic environment (*i.e.*, in solution) these quantities will be influenced by the viscosity and polarity of the specific solvent.

Chapter 5 Rationalizing Fluorescence Quenching in *meso*-BODIPY Dyes

The Chapter is published as: Prlj, A.[†]; Fabrizio, A.[†]; Corminboeuf, C. *Phys. Chem. Chem. Phys.* **2016**, *18*, 32668-32672 (†contributed equally)

Boron-dipyrromethene (BODIPY) dyes are a foremost class of small organic molecules with a wide range of applications in imaging and sensing,¹⁷⁰ photovoltaics,^{171,172} electrochemistry,¹⁷³ non-linear optics,^{174,175} lasers,^{176,177} etc. The key features of these compounds include excellent thermal and chemical stability as well as sharp absorption and emission bands with fluorescence quantum yields approaching 100%.¹⁷⁸ Their optoelectronic properties are generally tunable by introducing various substituents, which has prompted extensive synthetic efforts and fine-tuning of their optical performance through both experimental^{179–183} and quantum-chemical modelling.^{184–189} Owing to its unique versatility,^{190,191} the BODIPY dye was labeled as the “El Dorado for fluorescence tools”¹⁹⁰ and “the most versatile fluorophore ever”.¹⁹¹ However, *a priori* knowledge of the structure–property relationships connecting the substituent and the emissive properties of the dye still remains the holy grail for the molecular design.

meso-Substituted BODIPYs have received special attention due to their evident contrasting emissive behaviors.^{192–198} Small variations in the nature of the substituents are associated with dramatically different photophysical properties. In particular, BODIPY is strongly fluorescent upon UV irradiation if bonded to a sp^3 carbon, whereas the fluorescence of the sp^2 -bonded analogue is almost completely quenched.^{196–198} In particular, the excellent fluorescence characteristics of the parent BODIPY are preserved in the *meso*-substituted alkyl chain core (fluorescence quantum yields, $\Phi_f > 0.9$),^{194,196,199} but the *meso*-alkenyl derivatives are virtually non-fluorescent ($\Phi_f \approx 0$).^{196,199,200} Cosa *et al.* have shown that the same contrast holds for formyl (sp^2 , non-fluorescent) and hydroxymethyl (sp^3 , fluorescent), or iminyl (sp^2 , non-fluorescent) and aminomethyl (sp^3 , fluorescent) moieties.¹⁹⁷ Such sharp differences in the emissive properties do not typically hold for α - and β -substituted derivatives (see ref. [200] and the examples therein). The full mechanistic picture of the nonradiative decay in *meso*-substituted dyes is still missing even though the quantum yield drop was attributed to intramolecular deactivation pathways, consistent with the large Stokes shifts, rather than to a quenching mechanism such as intersystem crossing.¹⁹⁷ In this contribution, we unravel the key physical reasons behind the different emissive properties of two exemplary compounds *meso*-vinyl and *meso*-ethyl BODIPY (Scheme 5.1).



Scheme 5.1 Schematic 2D representations of the studied compounds with their expected fluorescence quantum yields (Φ_f).

Relying upon high level excited state and molecular dynamics computations, we provide evidence that **1** is more likely to deactivate non-radiatively from the first excited singlet state (S_1) to the ground state (S_0) due to the accessible conical intersection (CI). CIs are crossings between potential energy surfaces (of the same multiplicity), which enable very efficient non-radiative decay^{58,60,201–203} and have proved to be important to explain fluorescence properties of many organic dyes.^{163,204–207} In principle, a CI may be separated from the Franck–Condon (FC) region and the excited state minimum by a potential energy barrier. If the barrier can be easily overcome, the crossing region is energetically accessible and the system will easily undergo radiationless decay to the ground state. In contrast, large barriers will suppress the radiationless deactivation and promote fluorescence.

The electronic state profiles using a reaction coordinate that characterizes the excited state decay are provided in Figure 5.1 for both **1** and **2**. The geometry deformation largely corresponds to the butterfly-like motion of the BODIPY core, bending over the boron-*meso*-C line. Upon this geometrical change, the excited state potential energy surfaces are clearly flatter than that of the ground state. The key difference is revealed by a closer look at the energy landscape of the first excited state. The initial excitation of **1** to the S_1 state is followed by the large energetic relaxation (~ 0.4 eV) to the S_1 minimum, associated with the puckering of the BODIPY ring. The S_1/S_0 crossing point is geometrically close to the S_1 minimum, so the small geometrical evolution prompts the non-radiative relaxation to the ground state. The situation for **2** is rather different. As opposed to **1**, for which the excitation can delocalize to the π -system of the vinyl substituent (having a weak charge transfer character; see Figure S1 in the electronic supporting information, ESI), the relaxation effects in **2** are modest (~ 0.15 eV). The S_1 minimum is geometrically distant from the crossing, which is separated by an energy barrier. While the crossing is at a slightly lower energy than the FC point, the whole process following the reaction coordinate is energetically unfavorable. Hence the retention of the system close to the S_1 minimum prompts the radiative decay (*i.e.*, fluorescence). Additionally, the oscillator strength (between S_1 and S_0) in the excited state minimum is almost three times larger for **2** (0.29) than for **1** (0.11), which goes along with the smaller geometrical distortion of the former and points to its larger tendency for radiative decay. Nevertheless, the static profiles displayed in Figure 5.1 are not without deficiencies. In fact, the molecule absorbs a broad range of frequencies, which requires the sampling of various ground state geometries. The photoexcited molecules have already acquired a certain kinetic energy, which may help in overcoming the potential barrier (note that the interpolated barrier in Figure 5.1b is only the upper bound for the true barrier). Additionally, the crossings are typically reached at the higher energies rather than the minimal energy crossing point.²⁰⁸ It is therefore not clear whether the intersection region is also energetically accessible to **2**. Finally, alternative pathways and the possible participation of the higher excited states (through nonadiabatic coupling) are disregarded in this static picture (Figure 5.1).

To overcome these limitations, we provide more realistic molecular dynamics computations by initiating 50 independent trajectories in the S_1 states of both molecules. The initial conditions (*i.e.* structures and velocities) were sampled from the Boltzmann ensemble at 300 K and vertical excitations from the ground state equilibrium to the non-equilibrium S_1 state were assumed. In line with the static picture, all 50 trajectories of **1** follow the butterfly-like motion and reach the crossing intersection with S_0 . In sharp contrast, only one out of 50 computed trajectories of **2** reaches the crossing within the 1 ps simulation time. These results confirm the behavior anticipated from the much simpler profiles of Figure 5.1: **1** shows a large tendency for radiationless decay, whereas due to the energy barrier and the longer timescales involved, **2** tends to favor fluorescence.

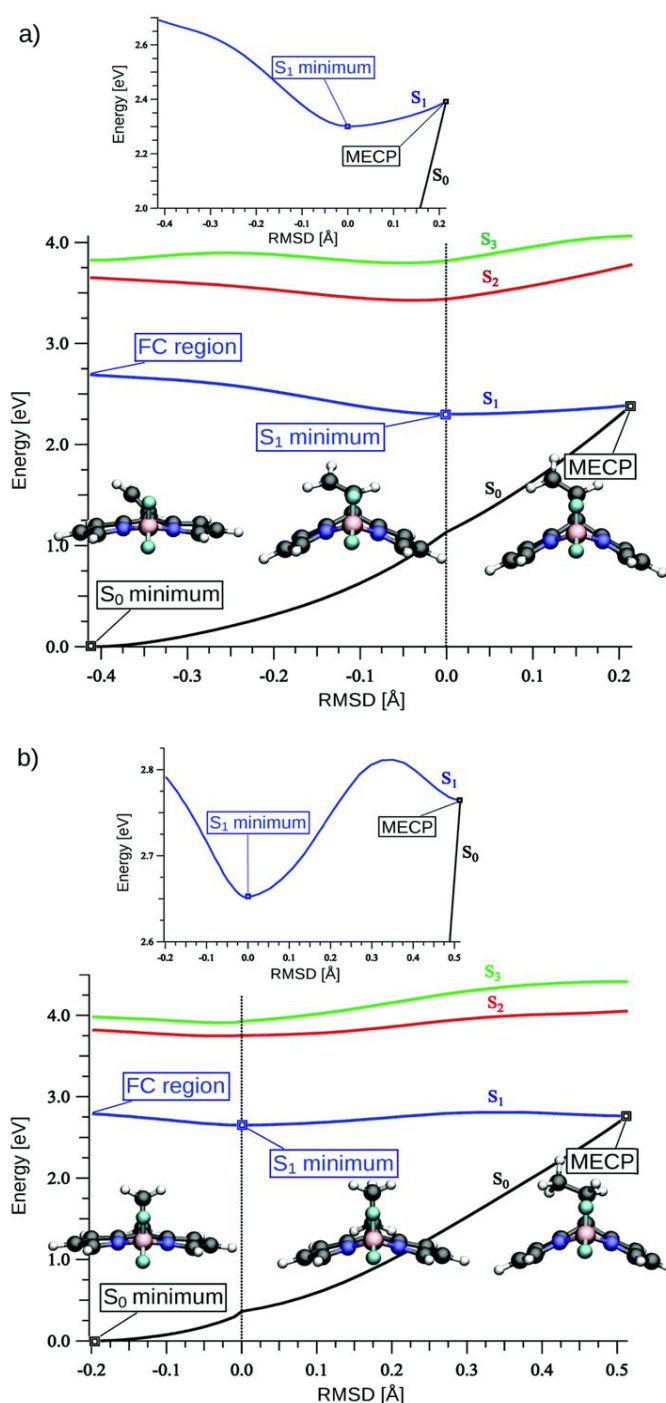


Figure 5.1 Energy profiles (in eV) of (a) **1** and (b) **2**. Optimized structures are shown as insets, while intermediate structures are obtained by linear interpolation of internal coordinates. Zoom into the S₁ topology is shown in smaller graphs. “MECP” stands for minimal energy crossing point. The ADC(2)/MP2 levels were used with the def2-SVP basis set.

The excited state molecular dynamics simulation also confirms that there is no participation from the higher excited states, as can be anticipated from the relatively large energy gaps between S₁ and S₂. Exemplary trajectories of both **1** and **2** are depicted in Figure 5.2, showing the time evolution of the electronic state potential energies and the simultaneous bending of the BODIPY core. While **1** evolves towards the S₁/S₀ intersection with the progressive bending of the fused core, **2** relaxes to the excited state minimum as indicated by the oscillations of the puckering angle.

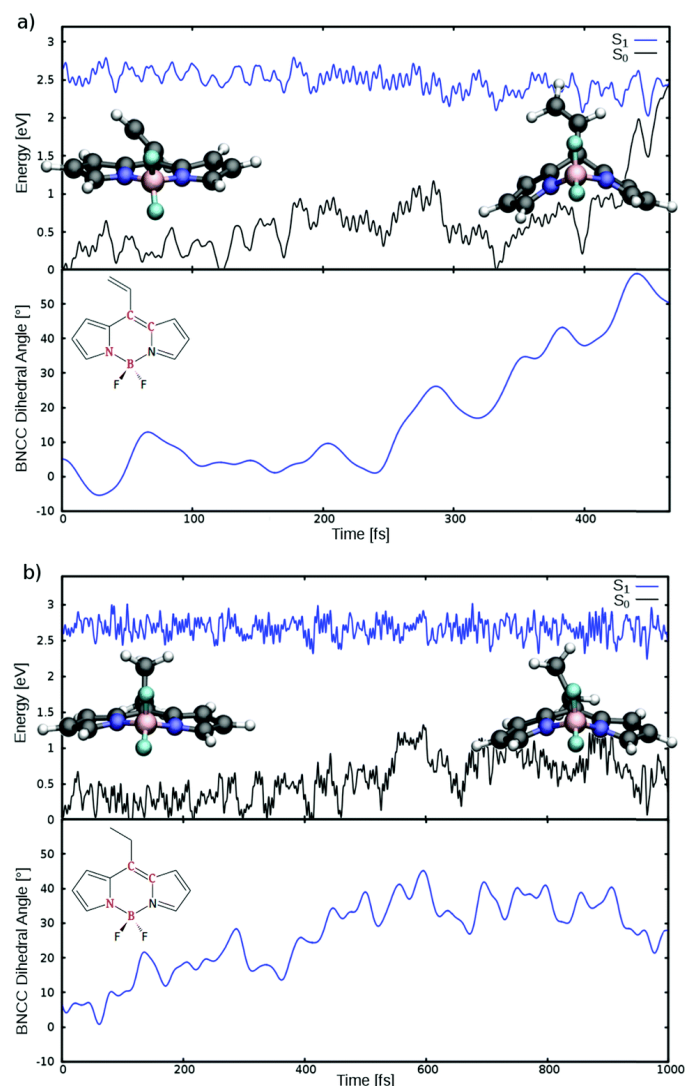


Figure 5.2 Illustrative trajectories for the S_1 dynamics of (a) **1** and (b) **2**, showing the time evolution of the potential energy surfaces of the ground and first excited states, as well as the BNCC torsional angle (atoms in red). Geometries of the first and the last frame of the dynamics are depicted. ADC(2)/MP2/def2-SVP levels were used.

Considering the ensemble of trajectories, the computed lower bound for the S_1 lifetime of **1** (in a vacuum) is roughly 0.5 ps, while the S_1 lifetime of **2** is inconclusive. Nevertheless, the solvent is expected to further slow down the relevant low-frequency motions, extending the timescales to the picosecond time range. We thus recomputed the potential energy surfaces (as in Figure 5.1) including the implicit tetrahydrofuran (THF; used in experiments¹⁹⁶) solvent (see the ESI), which shows no qualitative difference when compared to the vacuum case. Excited state molecular dynamics with the explicit THF solvent (within the QM-MM framework) were also performed (see the ESI). In this case, none of the trajectories reached the crossing within the imposed simulation time of 1 ps. The static and the dynamic pictures indicate that the solvent does not alter the photophysics of these compounds, apart from slowing down the dynamics due to the solvent drag. While desirable, the consideration of longer timescales is unfortunately cumbersome for real time molecular dynamics computations.

To summarize, the divergence in the fluorescence properties of two BODIPY dyes stems from the different topologies of the S_1 potential energy surface. **1** exhibits large stabilization upon photoexcitation along with the bending of the fused

BODIPY core. The crossing with the ground state is close to the excited state minimum so the population quickly decays to S_0 . **2** is qualitatively different. Excited state relaxation is modest and the crossing with the ground state is geometrically and energetically distant, due to the presence of a kinetic barrier. This difference points towards a dominant radiative relaxation pathway. From the general perspective of the fluorescence in BODIPY derivatives, the importance of CI (and its accessibility) still has to be investigated as theoretical studies on this topic are scarce.^{199,209} Previous explanations of non-radiative decay involving concepts such as intramolecular charge transfer and the lack of molecular rigidity^{193,200} are somewhat too general. The vast experimental work^{192–198} on *meso*-BODIPY dyes indicates that the principles demonstrated here have a broader significance. In fact, we have verified that *meso*-formyl and *meso*-hydroxymethyl derivatives are qualitatively similar to **1** and **2**, respectively (see the ESI). Therefore, we expect that the computational modeling will be of great relevance as a future guide for the rational design.

5.1 Computational section

Excited states were computed at the ADC(2) level^{5,22} combined with the def2-SVP^{93,210} basis set. The resolution of identity and frozen core approximations were employed. ADC(2) has proved to be reliable for potential energy surfaces^{80,205,211–214} and excited state dynamics^{37,86,152,153,215–217} of organic molecules. The method is particularly applicable for BODIPY dyes owing to the importance of differential correlation effects (which limits the use of standardly employed excited state methods such as TDDFT and CASSCF).^{218–220} Single point computations and optimizations were performed with Turbomole 6.5 software.⁹⁸ Minimal energy crossing points were optimized using the CIOpt code²²¹ coupled to Turbomole. Although ADC(2) does not provide the correct 2D branching space of the conical intersection between the first excited and the ground state (computed at the MP2 level), but rather a 1D diabatic-like crossing, a detailed benchmark study²²² has shown that it can provide correct geometries and energetics of the crossing, motivating the use of ADC(2) for photochemistry. Nevertheless, we here focus on the qualitative picture, while more quantitative data are provided in the ESI. Molecular geometries between the optimized structures were obtained *via* the linear interpolation of internal coordinates, while the relative lengths of the paths (Figure 5.1) were scaled based on the root mean square deviation (RMSD) between the first and the last structure. The ground and excited state dynamics analysis was performed with the Newton-X software⁹⁷ coupled to Turbomole. To sample the initial conditions, 20 ps long ground state dynamic trajectories were computed for both systems within the NVT ensemble at 300 K (Andersen thermostat). The PBE0¹⁰⁰/def2-SVP level was employed, with a time step of 1 fs. 50 initial conditions (coordinates and velocities) were sampled randomly from the last 15 ps of dynamics, and used for excited state dynamics initiated from S_1 . 50 trajectories (of each compound) were evolved within the *NVE* ensemble with the time step of 0.5 fs and the maximal time of 1 ps. Two higher excited states were included *via* the surface hopping scheme,³⁴ but since there was virtually no population in these states, the dynamics is equivalent to the adiabatic dynamics in S_1 . All the trajectories were terminated when approaching the crossing with the ground state, as discussed earlier.³⁷ For further details see the ESI.

Chapter 6 Fluorescence Quenching in BODIPY Dyes: The Role of Intramolecular Interactions and Charge Transfer

The Chapter is published as: Prlj, A.; Vannay, L.; Corminboeuf, C. *Helv. Chim. Acta* **2017**, *100*, e1700093.

6.1 Introduction

BODIPY derivatives have recently emerged as one of the most prominent classes of organic dyes, with wide applications in fields such as fluorescent imaging and sensing,^{170,223} dye-sensitized solar cells,^{224,225} lasing,²²⁶ non-linear optics,¹⁷⁵ photocatalysis,^{227,228} singlet oxygen generation and photodynamic therapy²²⁹ etc. These *cis*-constrained cyanines²¹⁹ were first synthesized in 1968²³⁰ (although the parent dye, **1** in Figure 6.1, was only reported in 2009²³¹), followed by an extensive synthetic efforts to functionalize the dye core and tune the chemical and photophysical properties.^{178,200,232} Alternatively, the success of BODIPY derivatives inspired the design of various similar compounds such as aza-BODIPY,²³² PODIPY,²³³ BODIHY,²³⁴ BOPHY,²³⁵ BOIMPY²³⁶ and others.^{237–239}

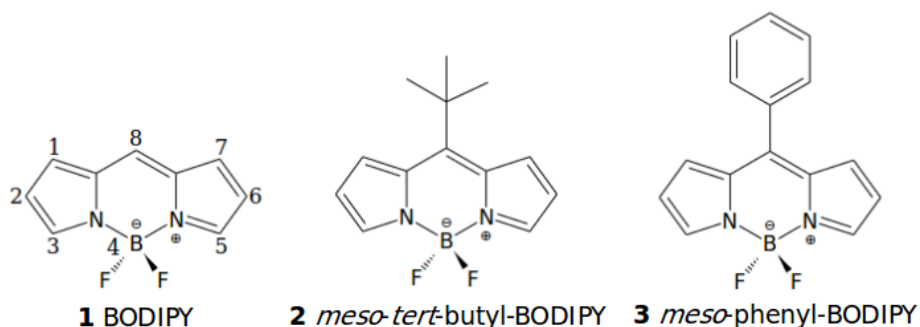


Figure 6.1 Studied compounds.

Of all possible positions, substitution at the *meso*-site (C(8) atom in Figure 6.1) is the most relevant, at least in terms of the fluorescence properties.^{192,196,197,199,240,241} As summarized in ref. [199], alkyl-, alkynyl-, and halo-substituted BODIPYs exhibit high fluorescence quantum yields (Φ_f), whereas for alkenyl- or aryl- substituents, the Φ_f values are small, often close to zero. The BODIPY dye itself has a relatively high Φ_f value (0.93 in ethanol, 0.77 in THF),²³¹ and the intense fluorescence, which is the basis for vast applications, persists in most of its derivatives. In our earlier work,²⁴¹ we addressed the contrast between fluorescence quenching in *meso*-alkenyl-BODIPYs, vs. the highly fluorescent *meso*-alkyl-BODIPYs. The divergent emissive properties can be well understood by the accessibility of the conical intersection upon excited state relaxation. Conical intersections,^{58,60} *i.e.*, the crossings between the electronic states of the same multiplicity are of key importance to rationalize the fluorescence properties of many organic molecules (see for instance recent applications in refs. [205,207,242–244]). In the illustrative vinyl-BODIPY compound, the crossing between the lowest excited singlet state (S_1) and the ground state (S_0) lies energetically below the initial vertical excitation, the so-called Franck-Condon (FC) point, thus explaining the high nonradiative rates. In sharp contrast, the kinetic barrier in ethyl-BODIPY makes the crossing less accessible, promoting the radiative decay instead of the internal conversion. Nevertheless, one might still wonder if the basic principles demonstrated for these systems (*i.e.*, the existence of the

low energy conical intersection and its accessibility) are broadly applicable to the photochemistry (fluorescence quenching in particular) of the other BODIPY compounds. The goal of the present work is to identify general underlying concepts based on three prototypical molecules depicted in Figure 6.1: parent BODIPY (**1**), *meso*-substituted *tert*-butyl-BODIPY (**2**) which, in contrast to other *meso*-alkyl-BODIPYs, is very weakly fluorescent, as well as the ubiquitous *meso*-phenyl-BODIPY (**3**). We employ state-of-the-art quantum chemical computations to differentiate the excited state deactivation pathways and rationalize the fluorescence properties of these compounds.

6.2 Results and Discussion

The emissive properties of the BODIPY dyes are intimately related to the topology of the S_1 potential energy surface. Rare examples violating Kasha's rule exist (for instance certain BODIHY compounds).²⁴⁵ The triplet state population *via* intersystem crossing is typically negligible, except for the heavy atom substituted BODIPYs^{246,247} and the specific fused^{248,249} and oligomeric compounds.²⁵⁰ For this reason, our attention is placed on the two lowest singlet electronic states, the ground and first excited state.

The electronic profiles of S_0 (blue) and S_1 (red) of **1** along the interpolated reaction coordinate (see Computational Section) are shown in Figure 6.2. For both states, the energy minima were optimized (detailed photophysical data are given in the Electronic Supporting Information, ESI). Unlike the nearly planar ground state geometry, BODIPY in its first excited state is symmetrically bent over the *meso*C-boron line. Our Density overlap region indicator (DORI)^{251,252} analysis of the bonding pattern in the S_0 and S_1 (Figure 6.3) reveals that the reduction of the CC bond order (most evident for the bonds involving *meso*C atom) is the main driving force for the bending.

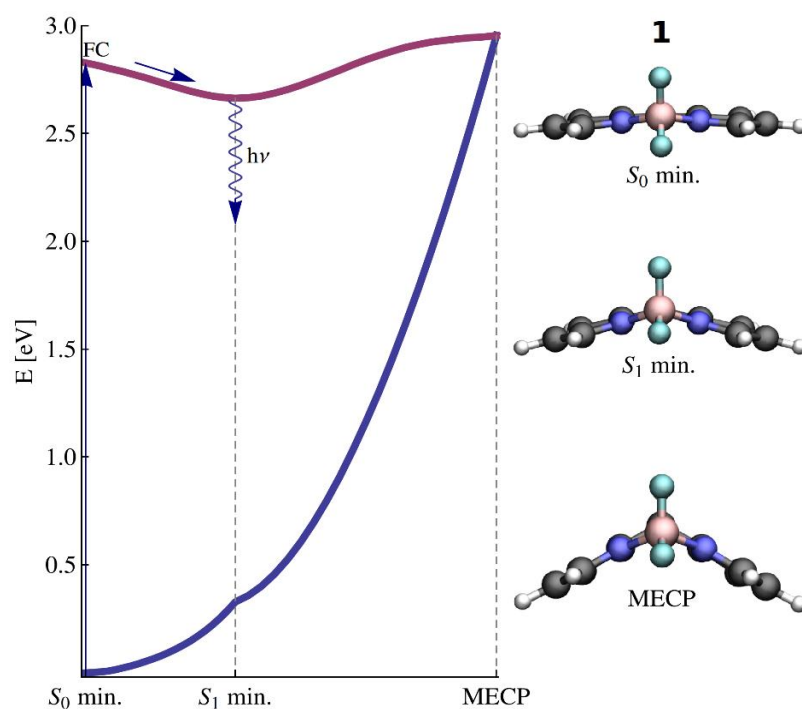


Figure 6.2 Energy profile (in eV) of compound **1**. The MP2/ADC(2) level and the def2-SVP basis set were used.

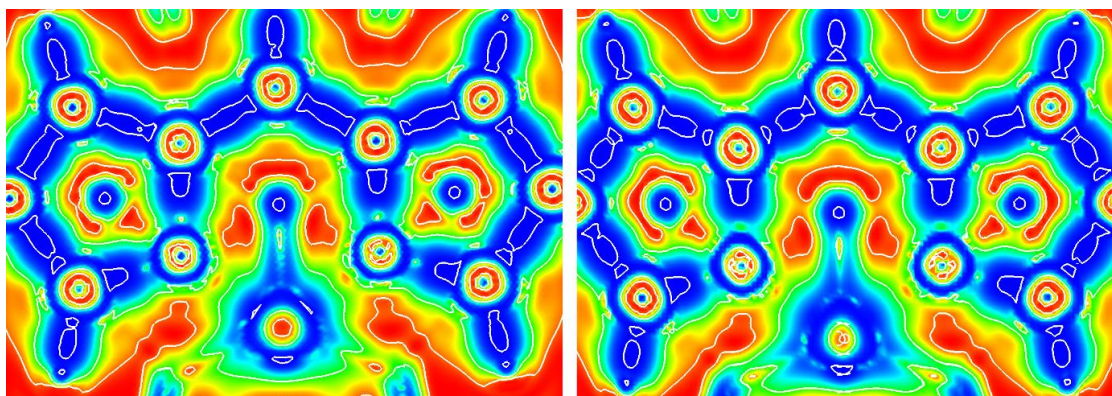


Figure 6.3 2D DORI map of **1** in S_0 (left) and S_1 (right) geometry. White contours represent the bonding pattern; a quasi-aromatic behavior characterizes the ground state, while the bond order is reduced in the excited state. Structures are oriented as in Figure 6.1. See the Computational Section for details. The MP2/ADC(2) level and the def2-SVP basis set were used.

In addition to the minimum energy stationary points, the minimum energy crossing point (MECP in Figure 6.2) between the two states was also optimized. The geometry is in fact very similar to the ones of the *meso*-substituted BODIPYs computed in our earlier work,²⁴¹ with the characteristic excessive bending of the fused core, and the out-of-plane distortion of the *meso*-bonded substituent (H-atom in case of bare dye). This similarity implies that the puckered conical intersection is a signature of all BODIPY dyes, while its energetic position critically depends on the substituents. If we turn our attention back to the Figure 6.2, we notice that upon photoexcitation the system can relax into the excited state minimum with a small excess energy (*ca.* 0.1 eV). Although relatively close, the barrier to the conical intersection is roughly twice the reorganization energy. Therefore, the nonradiative decay is not expected to play a major role. Dede *et al.*²⁰⁹ reported another S_1/S_0 conical intersection, associated with the BN bond breaking in the nearly planar geometry (located at the MCSCF level). Similarity to the conical intersection of the dipyrin molecule was invoked. However, this crossing is almost 3 eV above the FC region, which makes it irrelevant for the photophysics of BODIPY, unless it is excited to very high energies.

While most *meso*-alkyl BODIPYs are qualitatively similar to the parent dye, exhibiting intense fluorescence, compound **2** is an exception from the rule. It bears very low Φ_f values (0.04 in methanol, 0.045 in THF) with large Stokes shifts and a broad fluorescence peak (as opposed to the rather typical small Stokes shifts and a sharp fluorescence).¹⁹⁹ The unusual properties were explained by Jiao *et al.*¹⁹⁹ who located the conical intersection at the CASSCF level. The structure identified in our computations (MECP in Figure 6.4) resembles closely that of Jiao *et al.* confirming our hypothesis on common conical intersection. However, no shallow minimum close to the conical intersection was located at the present theoretical level. Nevertheless, the qualitative picture is clear: upon photoexcitation the system readily relaxes towards the conical intersection, with the subsequent transition to the ground electronic state. The remaining question is why does the crossing appear at such low energy? The DORI analysis of the ground state minimum, and of the structure in vicinity of the crossing (Figure 6.5) helps gaining further understanding. At the S_0 geometry, there is a steric clash between the BODIPY ring and the bulky *tert*-butyl group (red color; blue islands correspond to attractive interactions). The ground state and the excited state potential energy surfaces (near the FC region) are expected to be destabilized. However, as the structure approaches the crossing geometry, the *tert*-butyl group is pushed away from the BODIPY core and the steric interactions are less significant. Therefore, the energy of the crossing is not lifted higher. In addition, a weakly attractive interaction appears between the *tert*-butyl group and the fluorine atom. This rather directional and fairly electrostatic interaction, further stabilizes the crossing relative to the FC region. Finally, our analysis of the density difference (between excited and the ground state; see ESI) revealed a weak charge transfer from the pyrrole rings to the *meso*C atom and even to the substituent, which can also contribute to the stabilization of the excited state. This charge transfer appears surprising owing to the aliphatic nature of the *tert*-butyl group, but can possibly be explained by invoking hyperconjugation effects. Although charge transfer may weaken the aforementioned electrostatic

interaction, both effects are expected to lower the energy of the excited state. In summary, the combination of intramolecular non-covalent interactions and charge transfer character can significantly modify the shape of the excited state potential energy surface, leading to the unexpected fluorescence quenching.

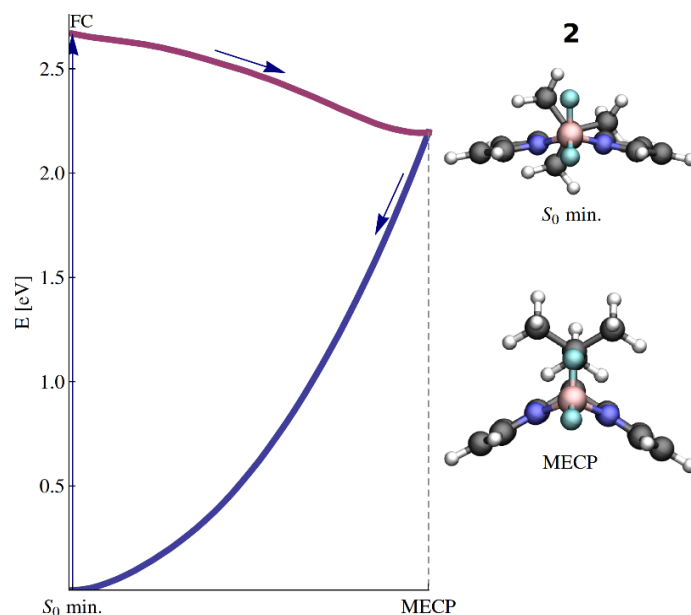


Figure 6.4 Energy profile (in eV) of compound **2**. The ADC(2)/MP2 level and the def2-SVP basis set were used.

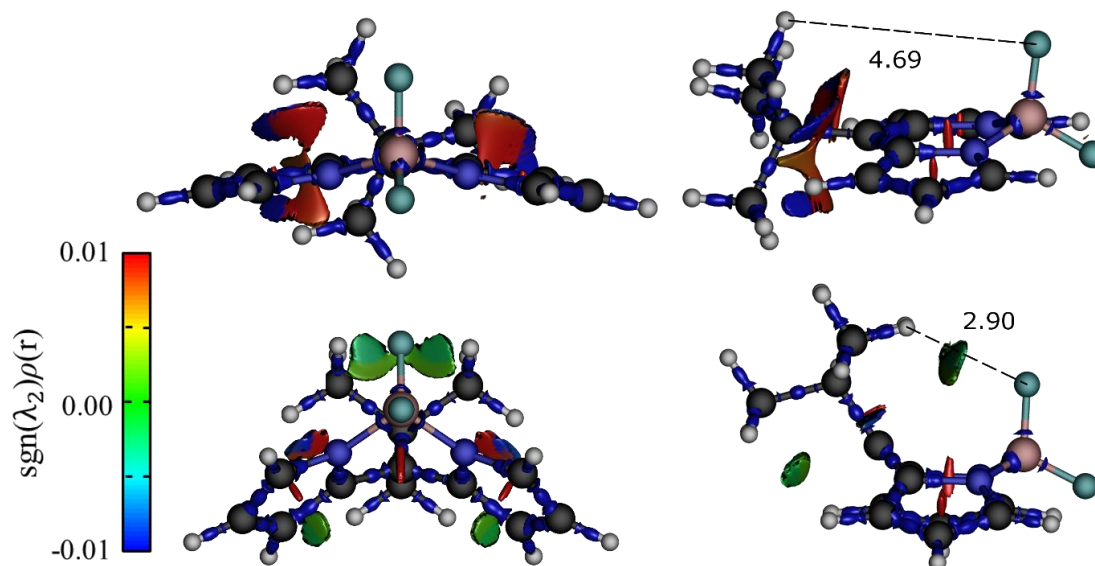


Figure 6.5 3D DORI representation (isovalue = 0.995) of compound **2** in the geometry of the ground state minimum (top) and near the conical intersection (bottom). DORI isosurfaces are color-coded ranging from blue (attractive) to red (repulsive interaction). For details on DORI see the Computational Section. The shortest hydrogen – fluorine distance [Å] is plotted in black dashed line. The MP2/ADC(2) level and the def2-SVP basis set were used.

Finally, we discuss *meso*-aryl-BODIPYs which are among the most popular BODIPY derivatives.^{178,192–194,200,232,240,253,254} Illustrative compound **3** is very weakly fluorescent in various solvents ($\Phi_f = 0.053$ in toluene,²⁴⁰ 0.065 in THF²⁵³). However, if the methyl groups are attached to the BODIPY core (on atoms C(1) and C(7)) or alternatively to the *ortho*-positions of the phenyl group, the Φ_f values become rather high; $\Phi_f = 0.65$ in the case of former (in methanol),²³² $\Phi_f = 0.93$ in the case of latter (in toluene).¹⁹² Fluorescence intensity also strongly depends on the viscosity of the solvent, *i.e.*, being larger in very viscous environments.²⁵⁴ This implies that the torsions of the aryl group are crucial for the nonradiative decay. Time-resolved spectroscopy of Lindsey *et al.*²⁴⁰ revealed a biphasic excited state decay (in toluene), with a major slow component of 440 ps, and a fast component of 17 ps. The complex excited state dynamics was explained based on semiempirical molecular orbital computations, which revealed the existence of two conformers in the S_1 state, the higher energy metastable state (**M**) responsible for the slow component, and the lower energy relaxed state (**R**) responsible for the fast component in decay. In a more recent study,¹⁹² time constants of *ca.* 400, 10 and 1 ps were determined (in toluene). Accompanying computations (at the SAC-CI level), however, suggest that the “barrierless or nearly barrierless” relaxation to the **R** minimum takes place directly from the FC region. In both studies, a nonradiative relaxation was ascribed to the (more or less) favorable vibrational overlap factors with the ground state at the excited state minimum geometries. Here, we would like to reconcile the picture of the excited state decay of **3** with the concept of conical intersection accessibility, and provide a somewhat different explanation for its complex excited state behavior.

The energy profile of the S_1 state between the S_0 geometry and the located minimal energy crossing point is shown in Figure 6.6. The crossing structure certainly resembles those of **1** and **2** (Figures 6.2 and 6.4). Both the **M** and **R** minima were optimized, though the torsional barrier of the former appears almost non-existent (< 0.01 eV). Since our standard procedure consisting in the interpolation of internal coordinates leads to unphysical barriers between the **M** and **R** conformers (due to the steric clashes in the intermediate geometries), we performed a constrained optimization, which presumably follows the reaction coordinate close to the minimal energy path. In the ground state, the phenyl ring is almost orthogonal to the BODIPY core (Figure 6.6). In the excited state, the relaxation proceeds through both the ring torsion and the core bending. The rotational axis of the phenyl moiety in **M** still lies approximately in the plane of the BODIPY ring. Pure rotation and excessive core bending are both strongly hindered by the steric interaction. However, the concerted motion (torsion plus bending) appears unhindered (as indicated by vanishingly small barrier). At the critical torsional angle (sharp feature in Figure 6.6), the phenyl ring is released from the structural constraints imposed by the H(1) and H(7) atoms and the large out-of-plane distortion, accompanied by a sudden drop in energy towards the **R** minimum, takes place. The excess in reorganization energy is certainly sufficient to reach the conical intersection (which is energetically below the **M** minimum). Lindsey *et al.* argue that upon photoexcitation both the **M** and **R** conformers are formed on the ultrafast time scale, with little interconversion between them. **M** decays *via* both the radiative and nonradiative pathways (long lifetime), while **R** decays mainly nonradiatively (short lifetime).²⁴⁰ It is clear that the fast decay components correspond to the immediate relaxation to the **R** state and its subsequent internal conversion. However, due to the vanishing barrier associated with the **M** conformer, it is also likely that the excited state population initially trapped in **M** will slowly leak towards **R** and the nearby conical intersection. Accordingly, we propose the following scenario. Depending on the initially excited vibronic mode, part of the population will quickly relax to the **R** minimum and decay to the ground state *via* conical intersection. Larger part of the population will presumably be trapped in a metastable state **M**. The trapping is also consistent with the small Stokes shifts observed in experiments (*i.e.*, the emission from the **R** state would result with rather large Stokes shifts). Favorable pathway towards **R** is very narrow and implies the concerted ring torsion and the core bending motion. Therefore, slow relaxation to the conical intersection is expected to occur on a longer timescale. Hence, the energetically accessible conical intersection may play an essential role in the fluorescence quenching of the compound **3**, but the high-level wave packet simulations would be necessary to provide an unambiguous picture.

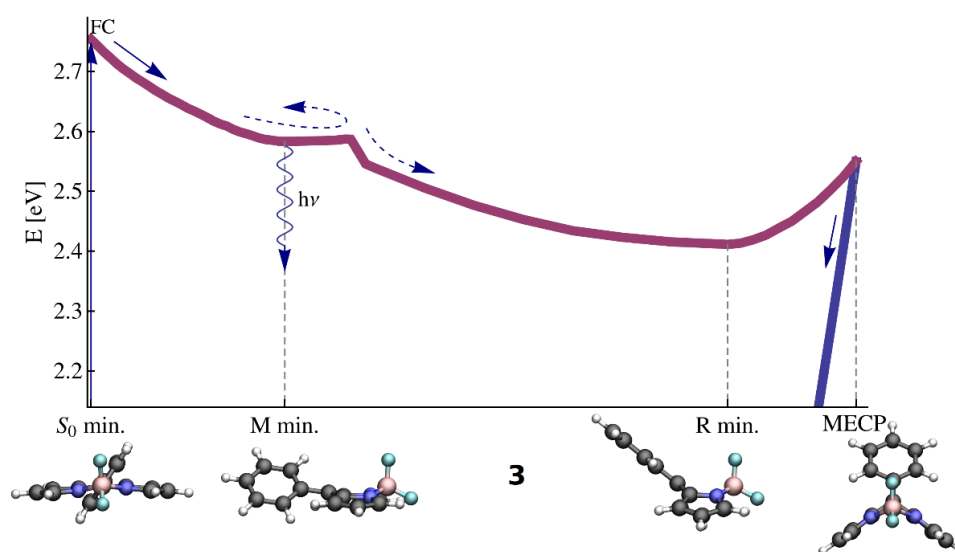


Figure 6.6 Energy profile (in eV) of compound **3**. The MP2/ADC(2) level and the def2-SVP basis set were used.

Why is the crossing stabilized relative to the FC region (when compared to the parent compound **1**) remains to be clarified. Although the intramolecular interactions (*i.e.*, steric clashes) play an important role in the dynamics, the primary reason is of electronic nature and can be rationalized by considering only the HOMO and LUMO. As noted earlier,^{192,200,240} the HOMO has a node in the boron-*meso*C vertical plane, and does not extend to the *meso*-group. On the other hand, the LUMO can delocalize on the *meso*-substituent, lowering its energy. Upon rotation of the phenyl ring, the S_1 state of **3** will transfer charge through the delocalized LUMO (Figure 6.7).

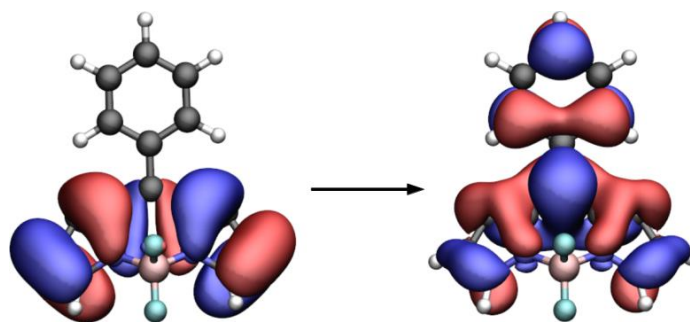


Figure 6.7 Dominant natural transition orbitals (NTOs; coeff = 0.99) of the S_1 state of compound **3** in the minimum geometry of **R**. The ADC(2)/def2-SVP level was used; isovalue = 0.02.

The portion of the potential energy surface with a charge transfer character is stabilized with respect to the FC region, and the conical intersection becomes energetically accessible. In our earlier work, we have found that the S_1 state of non-emissive vinyl-BODIPY also achieves a partial charge transfer character upon torsion of the vinyl moiety. Therefore, the stabilization by charge transfer can be regarded as a general effect, which explains the weak fluorescence of the *meso*-BODIPY dyes substituted with the conjugated sp^2 moieties. Some caution should be taken for the large electron donating groups such as triphenylamine and pyrene.^{193,194} Here an additional excited state appears in the low energy spectral region, exhibiting the charge transfer between the electron donating *meso*-substituent and the BODIPY acceptor (charge transfer has a direction opposite to that in **3**). In the polar environment, this state may be stabilized below the local BODIPY excitation, and the population transfer to the “dark” charge transfer state causes a loss of fluorescence.

6.3 Conclusions

Fluorescence properties of BODIPY dyes were rationalized by exploring the topology of the lowest excited singlet state. The parent BODIPY exhibits a low lying conical intersection with the ground state, corresponding to the substantial bending of the molecular core over the boron-*meso*C line. Since the conical intersection is located at an energy higher than the Franck-Condon point, nonradiative decay is not expected to be significant. However, different substituents, in particular those at the *meso*-position, can “stabilize” the conical intersection, which prompts the internal conversion to the ground electronic state. We have identified two distinct situations, which lead to the relative lowering of the crossing energy and, as a consequence, to the quenching of fluorescence. In the case of *tert*-butyl-BODIPY, non-covalent interactions within the molecule play a key role, destabilizing the Franck-Condon region and stabilizing the crossing region. A partial charge transfer character was also detected. For phenyl-BODIPY, excited state achieves a significant charge transfer character upon torsion of the phenyl moiety, which lowers the energy of both the excited state global minimum and the nearby conical intersection. Since the intersection becomes energetically accessible, the excited state population is expected to decay to the ground state. The concept of the conical intersection accessibility was already successfully applied in our earlier study on *meso*-alkyl and *meso*-alkenyl compounds, explaining their distinct emissive properties observed in experiments.²⁴¹ Therefore the present methodology can be further generalized and used for the structure-property relationships and the rational design of the new BODIPY fluorophores.

6.4 Computational Section

A variety of theoretical methods were previously employed to study excited states of BODIPY and its derivatives, including DFT based (TDDFT,^{184,197,247,249,255,256} Δ SCF,^{253,257} ROKS,²⁵⁸ DFT-MRCI²⁵⁹), single reference wavefunction-based (ADC(2),^{241,260} CC2,¹⁸⁶ SAC-CI¹⁹²), mixed (SOS-CIS(D)/TDDFT²¹⁸), multireference (CASSCF,^{199,209,250} CASPT2,²⁵⁷ XMCQDPT2²⁶¹), semiempirical²⁴⁰ and machine learning¹⁸⁹ methods. The S_1 state of various BODIPY compounds is well described by a single excitation from the highest occupied (HOMO) to the lowest unoccupied molecular orbital (LUMO), having a high oscillator strength which manifests in the intense and sharp absorption peaks.²¹⁹ However, BODIPYs are considered challenging due to the importance of dynamical electron correlation effects.^{218–220} The same problem holds for linear cyanines as widely discussed in the literature.^{262–266} The single excitation methods (such as TDDFT or CIS) as well as methods which lack dynamical correlation (CASSCF) are expected to have large errors.²²⁰ In a benchmark study of Momeni and Brown,²²⁰ the best performance was assigned to the CASPT2 and the local CC2 method. Here we use the ADC(2) method^{21,22} which is closely related, and has a similar accuracy as CC2.²⁸ ADC(2) was recently applied to various organic molecules,^{86,152,153,205,213,241,243,244} typically providing the results consistent with experiments. The method can also be used for optimizing conical intersections,^{205,211,212,214,217,241,243,267} although it does not provide a correct dimensionality of the crossing seam (for S_1/S_0 crossing).²²² The computations were performed with Turbomole 7.0.2 package⁹⁸ and the strict ADC(2) method implemented therein. Ground state computations were performed with MP2 method. The def2-SVP⁹³ basis set was systematically used; BODIPY compounds exhibit a relatively small basis set dependence, as shown in Table S2 in ESI. The resolution of identity (along with the universal auxiliary basis set²¹⁰) and the frozen core approximations were employed. Minimal energy crossing points were optimized with CIOpt code²²¹ coupled to Turbomole. For all optimized geometries, tight convergence criteria were chosen. While the interpolated energies are generally not representative of the minimum energy pathway in the excited state, the energetic positions of the optimized critical points provide a good description of the excited state dynamics. The coordinate interpolation serves essentially as a visual guideline. When this interpolation leads to an unnaturally high barrier, we employed a constrained optimization. For the segment between the **M** and **R** minima of compound **3**, the energies were computed by a constrained optimization in which the torsional angle ϕ (see ESI for definition) was fixed and varied ranging from -49.2° corresponding to the **M** structure and -4.3° corresponding to the **R** structure. The relative distances between the points (*i.e.*, minima and MECPs) on the reaction coordinate were scaled based on the root mean square deviation between the structures of the consecutive points. All the optimized structures (xyz) and the detailed photophysical data are given in ESI. Profiles in the Figures 6.2, 6.4, and 6.6 were computed in the vacuum, thus reflecting the intrinsic properties of the molecules. Continuum solvation models are challenging to apply in this case (equilibrium vs. nonequilibrium conditions²⁶⁸ in the excited state). Nevertheless, earlier studies imply that the solvent

effects are not very significant.^{241,256} The state with the charge transfer character (as in molecule **3**) may be further stabilized in the polar environment but this is still fully compatible with the proposed interpretation of the excited state dynamics. The qualitative shape of S_1 potential energy surface remains the same, even if there is an additional stabilization of the portion of potential energy surface with the charge transfer character.

Density overlap region indicator (DORI)^{251,252} was used to describe bonding pattern and the intramolecular interactions. DORI detects regions where electron density stemming from different atoms overlap. However, while DORI provides the extent of the overlap, it is inapt at distinguishing whether the interaction is attractive or repulsive. This information is retrieved using the second eigenvalue of the Laplacian of the electron density (λ_2): $\nabla^2\rho = \lambda_1 + \lambda_2 + \lambda_3$, ($\lambda_1 \leq \lambda_2 \leq \lambda_3$). λ_2 is negative in bonding regions, and positive for repulsive interactions. The interaction strength is estimated using the value of the density itself: $\text{sgn}(\lambda_2)\rho(r)$ (see refs. [251] and [269] for more details). For applications of DORI in excited states see ref. [252]. Both DORI and $\nabla^2\rho$ were computed numerically on optimized densities, with a precision of 10 points/bohr on the grid mesh. DORI was obtained using a local script, whereas $\nabla^2\rho$ was computed using the NCImilano software.²⁷⁰

Chapter 7 Qualitatively Incorrect Features in the TDDFT Spectrum of Thiophene-Based Compounds

The Chapter is published as: Prlj, A.; Curchod, B. F. E.; Fabrizio, A.; Floryan, L.; Corminboeuf, C. *J. Phys. Chem. Lett.* **2015**, *6*, 13-21.

Thiophene-based materials play a central role in the field of organic electronics.^{67,68,271} Derivatives of thiophene, oligothiophenes and oligothienoacenes are extensively used in organic photovoltaics,^{69,70,272-276} light emitting diodes,^{71,72,277-279} field effect transistors,²⁸⁰⁻²⁸⁵ and so forth. Typically high extinction coefficients make them particularly suitable for solar cell materials. As a matter of fact, organic dyes, which do not contain thiophene motifs, seem to be in minority. This is part of the reason why excited states of simple thiophene compounds have drawn interest from numerous theoretical perspectives, including spectroscopy,^{76,78,87-92,109,119,286-290} excited state geometries,^{76,78,88} and nonadiabatic molecular dynamics.^{77,85} In this Letter, we discuss the computational conundrum associated with the low-lying bright $\pi\pi^*$ singlet excited states of thiophene, short oligothiophenes, and oligothienoacenes (planar fused oligomers). Figure 7.1 compares the absorption spectra of thiophene computed with linear-response time-dependent density functional theory (TDDFT) and a post-Hartree-Fock (post-HF) formalism. The overall band structure appears rather similar, yet decomposition into individual states (*vide infra*) reveals an inversion that could dramatically impact the computational prediction of photochemical and photophysical processes of thiophene-based compounds. We believe that this dichotomy and especially its consequences have been overlooked in the literature. The following analysis discusses the underlying origin for this contrasting behavior and identifies methods that alleviate the problem.

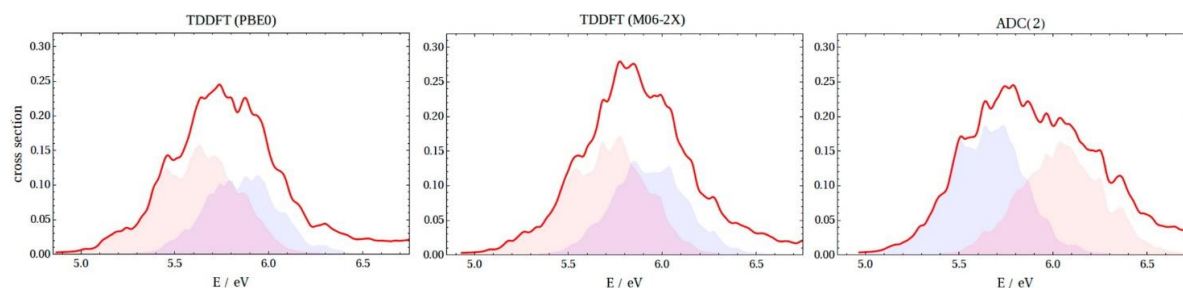


Figure 7.1 Photoabsorption spectra computed from the Wigner distribution (red line) of thiophene. The spectra were decomposed into contributions from two lowest excited states, S_1 and S_2 . The red peak is mainly due to the excitations from highest occupied to the lowest unoccupied molecular orbital (HOMO \rightarrow LUMO, B_2), whereas the blue peak is dominated by HOMO-1 \rightarrow LUMO, A_1 , character. The cc-pVTZ basis set was used.

TDDFT,¹¹ or more precisely linear response TDDFT within the adiabatic approximation,¹⁹ has emerged as the most widely used method for molecular excited states.¹⁰⁸ Its exalted status certainly arises from the combination of low computational cost and, in many cases, amazing predictive power for both excitation energies²⁹¹ and excited state properties²⁵⁵ of fairly large systems. This contrasts sharply with highly accurate multireference methods, such as CASPT2 (complete active space second order perturbation theory)²⁹² and MCQDPT2 (multiconfigurational quasi-degenerate second order perturbation theory),²⁹³ which can be applied only to small systems that appear particularly challenging (of relevance to the present study, we point out the controversy with CASPT2 results for bithiophene⁹¹). Although TDDFT

is a formally exact theory, standardly employed approximations result in several limitations. These include the underestimation of charge-transfer and Rydberg excitations,²⁹⁴ underestimation of triplet excitation energies,²⁹⁵ and a general inapplicability for high-lying excited states.²⁹⁶ The ubiquitous adiabatic approximation is responsible for the inaccurate description of conical intersections as well as the absence of doubly and multiply excited states^{297,298} (though it also underlies the charge-transfer problem²⁹⁹). Valence $\pi\pi^*$ states with mainly single excitation character (which are studied here) are usually considered less problematic, although exceptions do exist. Grimme and Parac studied the two lowest singlet $\pi\pi^*$ states of oligoacenes,³⁰⁰ short-axis polarized L_a (HOMO \rightarrow LUMO) and long-axis polarized L_b (HOMO-1 \rightarrow LUMO, HOMO \rightarrow LUMO+1). They found L_a to be strongly underestimated by hybrid and GGA (generalized gradient approximation) functionals, with spurious inversion of states in case of naphthalene. L_a was later described as an “ionic”,³⁰⁰ “charge-transfer in disguise”³⁰¹ and “charge-transfer-like”³⁰² excitation. Substantial improvements were found with range separated hybrid functionals.^{303,304} Most recently, by employing a range separated hybrid functional with optimally tuned parameter,³⁰⁵ Baer, Kronik *et al.*³⁰² reported excellent agreement with reference CC2 (approximate coupled cluster singles and doubles)³⁰⁶ results, thereby restoring the predictive power of TDDFT for the oligoacene series.

Here we focus upon the $\pi\pi^*$ state inversion in related categories of π -conjugated thiophenes and oligothiophenoacenes that are, nevertheless, distinct in nature due to the presence of third row heteroatoms (*i.e.*, low-lying *d*-orbitals close in energy) and lower symmetry. The problem illustrated for thiophene in Figure 7.1 is further examined by computing the vertical excitation energies of the two lowest $\pi\pi^*$ states at various TDDFT and post-Hartree–Fock levels (Figure 7.2a). TDDFT generally predicts that two states, one dominated by the HOMO \rightarrow LUMO (B_2) and another by the HOMO-1 \rightarrow LUMO (A_1) transition, appear in a reversed order (or nearly degenerate) when compared to more accurate post-HF methods. The dependence on the specific exchange–correlation kernels and especially on the fraction of exact exchange is assessed *via* consideration of different categories of functionals: PBE (GGA), B3LYP and PBE0 (global GGA hybrid), M06 (*meta*-GGA hybrid), M06-2X (*meta*-GGA hybrid with 54% Hartree–Fock exchange), long-range corrected hybrid, ω B97x-D as well as optimally tuned long-range corrected hybrid LC-PBE*. Despite their conceptual differences, each of these functionals gives the same qualitative results: two transitions of similar intensities with B_2 being slightly lower than A_1 . Including an implicit polar solvent does not alter the ordering of the transitions and only slightly affects the excitation energies (see Electronic Supporting Information, ESI). This state ordering is amplified with the CIS (configuration interaction singles) approach, and its response analogue TD-HF (time dependent Hartree–Fock).¹² However, the energy of the HOMO-1 \rightarrow LUMO (A_1) state drops by more than 1 eV, and the sequence reverses when correlation is added to CIS by means of doubles and approximate triples using the CIS(D) method.³⁰⁷ This indicates that A_1 is highly sensitive to the correlation effects introduced by CIS(D). CC2 and the second order algebraic diagrammatic construction, ADC(2),²² predict the same ordering as CIS(D). This post-HF picture is further solidified by the computationally more involved EOM-CCSD (equation of motion coupled cluster singles doubles),³⁰⁸ SAC-CI (symmetry adapted cluster–configuration interaction)³⁰⁹ and multi state MS-CASPT2 of ref. [78]. Additionally, the agreement achieved by the double hybrid TDA-B2PLYP with wavefunction-based methods is excellent. Similar in spirit to CIS(D), the double hybrid approach of Grimme and Neese²⁶³ adds perturbative second-order corrections to the CIS-like representation of TDDFT (*i.e.*, TDDFT in Tamm–Dancoff approximation; TDA). Although less dramatic, an inversion similar to CIS/CIS(D) is found for the two excited states of thiophene with the double hybrid after introducing the perturbative correction (for details, see Table 1 in ESI).

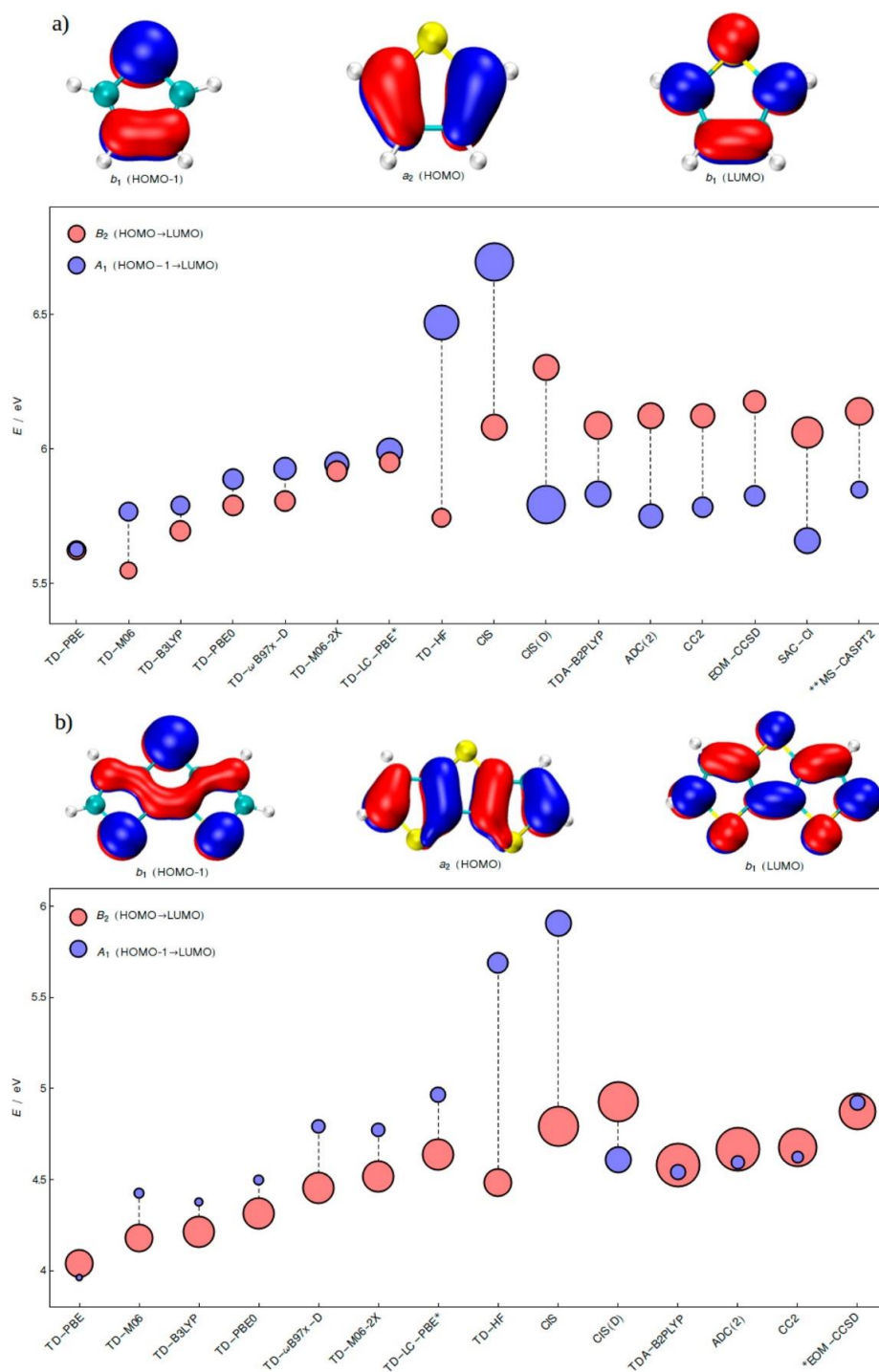


Figure 7.2 Excitation energies of the two lowest $\pi\pi^*$ states (S_1 and S_2) of (a) thiophene and (b) dithieno[2,3-*b*:2',3'-*d*]thiophene. Radii of the circles are proportional to the oscillator strengths, and the colors indicate the dominant character. Relevant M06 orbitals are shown. Note that there is no qualitative difference between Kohn–Sham and Hartree–Fock orbitals. The cc-pVQZ basis set was employed. *EOM-CCSD indicates that the energies of dithienothiophene were computed with the cc-pVTZ basis set. The **CASPT2 results for thiophene are taken from ref. [78] and correspond to experimental geometry of Bak *et al.*³¹⁰

Similar patterns are seen for the A_1 and B_2 representations of fused dithienothiophene (Figure 7.2b), which belongs to the same symmetry point group, C_{2v} , as the thiophene example discussed above. Transiting from CIS to CIS(D) inverses the energy ordering of the two $\pi\pi^*$ excitations. The TDDFT computations generally match the CIS trend, with the exception of pure PBE, which still gives too low excitation energies. On the other hand, wavefunction-based methods, along with TDA-B2PLYP, slightly improve the CIS(D) results through reduction of the energy gap between the two states. The possibility of double excitations playing a role can be excluded as diagnostic tools associated with ADC(2) and CC2 indicate that both states are dominated by single excitations from the single configurational ground state. The origin of the TDDFT problems is more subtle than that of CIS (*i.e.*, correlation effects). In fact, from the energetic perspective the HOMO-1 \rightarrow LUMO state is reasonably well positioned by both the reference wavefunction methods and TDDFT, especially when functionals with moderate amount of exact exchange are chosen. By carefully examining Figures 7.2a and 7.2b and drawing a parallel with the oligoacene example discussed above,^{300–304} it appears that the HOMO \rightarrow LUMO state is underestimated by TDDFT. Inclusion of exact exchange shifts the energy of this transition; however, it simultaneously shifts the other state, which is affected by correlation effects. The overall result being that no qualitative improvement is observed. Optimally tuned long-range corrected functional³⁰² performs no better than hybrid and long-range corrected hybrid functionals. The state inversion in the TDDFT context is certainly caused by interplay of different effects that influence each of the two states. Because none of the standard functionals (within the strict linear-response TDDFT) that are tested here provides a suitable description and the “single state engineering” through increasing the amount of exact exchange is ineffective, the error is inherently connected with subtler effects in the description of correlation for the excited state. The trends obtained with the double hybrid are qualitatively correct, emphasizing the importance of perturbative doubles corrections applied to TDA. Upon inclusion of virtual orbitals, the CIS(D)-like correction captures nonlocal correlation effects missed by conventional approximate functionals in the adiabatic approximation, as advocated by Grimme *et al.*^{263,311,312} We note, however, that the (D) correction term is only a pragmatic fix in the context of TDDFT. The mechanisms leading to an improvement between uncorrected TDDFT and TDDFT/CIS(D), in the framework of exact TDDFT, are surely more complex to grasp than those between CIS and CIS(D). In this context, we notice that even the Tamm–Dancoff approximation applied to certain functionals (for instance PBE0) may improve the results of the parent TDDFT approach.

C_{2h} thienothiophene (Figure 7.3a) is a somewhat more complicated example. CIS(D) again inverts CIS, and so does the double hybrid with respect to its underlying TDA energies. Yet the TDA-B2PLYP excitation energies do not align well with those from the post-Hartree–Fock methods. The TDDFT picture contrasts with the wavefunction-based methods with the intense state lying slightly below the second weaker state. Because of symmetry reasons (two states of B_u representation close in energy), our analysis of relaxed density differences reveals a large degree of character mixing, rather than the clear-cut inversion implied by the simplified orbital representation. The character ambiguity arises from the different extents of density increase/depletion at sulfur atoms and the central CC bond (see ESI). Nevertheless, the problematic behavior of TDDFT concerning both the excitation energies and the corresponding oscillator strengths of thienothiophene $\pi\pi^*$ states is fully in line with the two former examples (Figure 7.2). In sharp contrast, nonplanar bithiophene (Figure 7.3b) and terthiophene (ESI) are rather unproblematic, at least qualitatively. The small dependence on the exact exchange fraction and the energy lowering of the second bright state when moving from CIS and CIS(D) still holds, yet the energy gap between the two $\pi\pi^*$ states is consistently large and no inversion occurs. Such a separation arises from the limited conjugation between flexible oligothiophene units. Unlike in thiophene and thienoacenes, where we always refer to S_1 and S_2 , for bithiophene and terthiophene, the two bright transitions are typically S_1 and S_3/S_7 , respectively (see ESI).

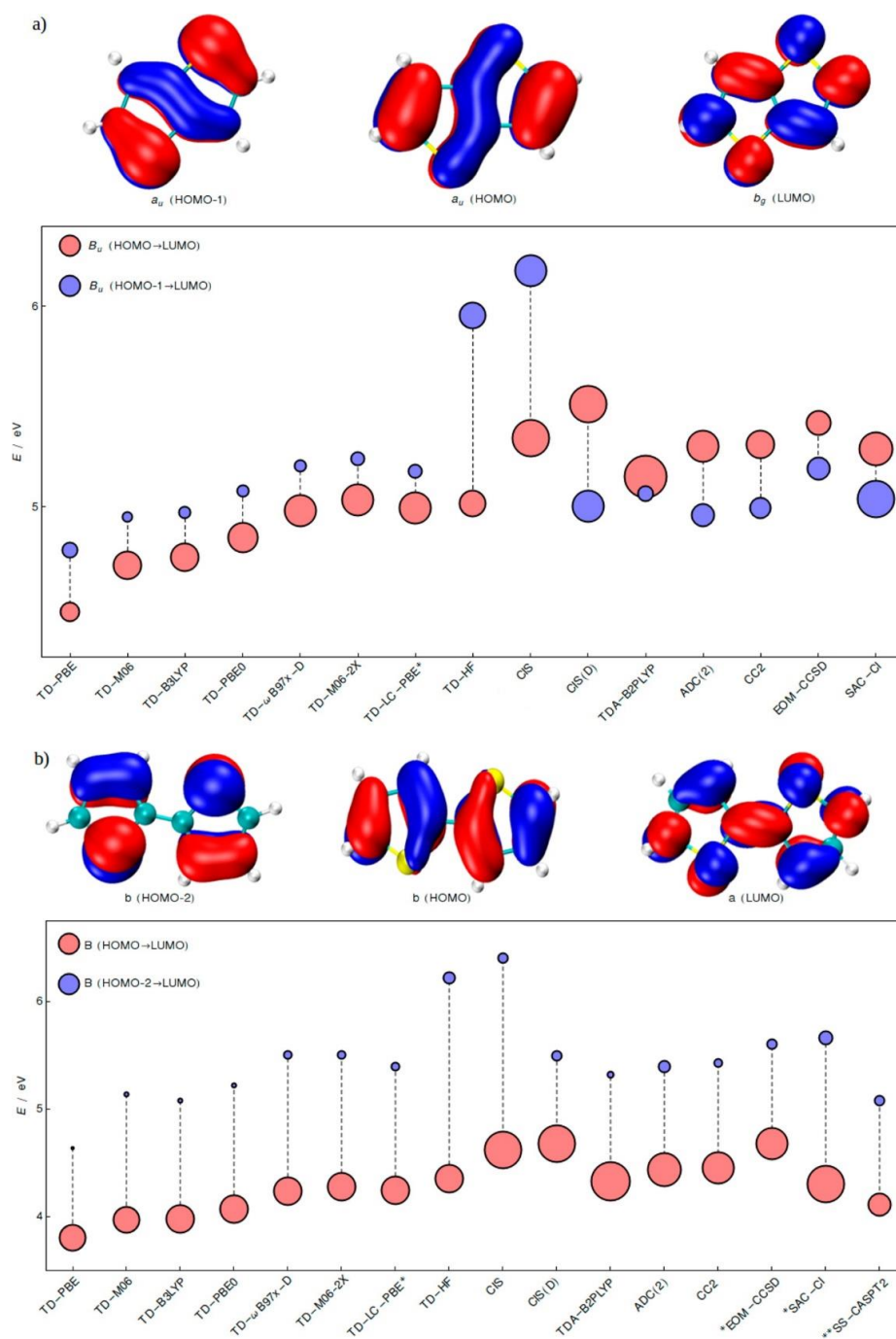


Figure 7.3 Excitation energies of the two lowest bright $\pi\pi^*$ states of (a) thieno[3,2-*b*]thiophene (S_1 and S_2) and (b) 2,2'-bithiophene (S_1 and S_3/S_4). As in Figure 7.2, radii of the circles are proportional to the oscillator strengths, and colors denote the orbital excitations with largest coefficients. The cc-pVQZ basis set was employed. The *EOM-CCSD and SAC-CI energies of bithiophene were computed at the cc-pVTZ level. The **CASPT2 results of bithiophene are taken from ref. [91] and correspond to the ground state structure optimized at CASPT2 level with C_{2h} symmetry.

The consequence of the state inversion is best illustrated by the absorption spectra of thiophene highlighted earlier (Figure 7.1) and its derivatives (Figure 7.4), which are computed using the geometries sampled from semiclassical Wigner distribution (see ESI) at three illustrative levels, PBE0, M06-2X, and ADC(2). Despite the use of an identical set of 500 initial structures generated from a Wigner distribution in the ground electronic state, the TDDFT spectra of

thiophene and dithienothiophene contrast with the ADC(2) spectra. The decomposition of the spectrum into the relevant state contributions (color coding is the same as in Figures 7.1 and 7.2) reveals that the inversion is not just an artefact of the optimized geometries: the overall peak intensities largely follow the trends given by the oscillator strengths in the static computations. For thiophene, both functionals predict two overlapping peaks, which results in a single unstructured hill, whereas the ADC(2) spectrum shows both a different state ordering and a longer tail at higher energies, consistent with experimentally measured cross sections.¹⁰⁹ The situation is similar for dithienothiophene, where ADC(2) places two states close in energy resulting in an intense peak differing from TDDFT predictions. The seemingly reliable TDDFT spectra of thienothiophene actually emerge from a peculiar mixing of states. Although we intentionally do not attribute the dominant character from the orbital contributions, the contrast between the methods is clearly visible from the small TDDFT intensities of S_2 , which is consistent with the oscillator strengths computed at the optimized geometry (Figure 7.3a). On the other hand, the dichotomy does not apply to bithiophene, for which all three methods give similar pictures with only minor difference in the position and peak intensity. Note that the two functionals give similar results in all four cases.

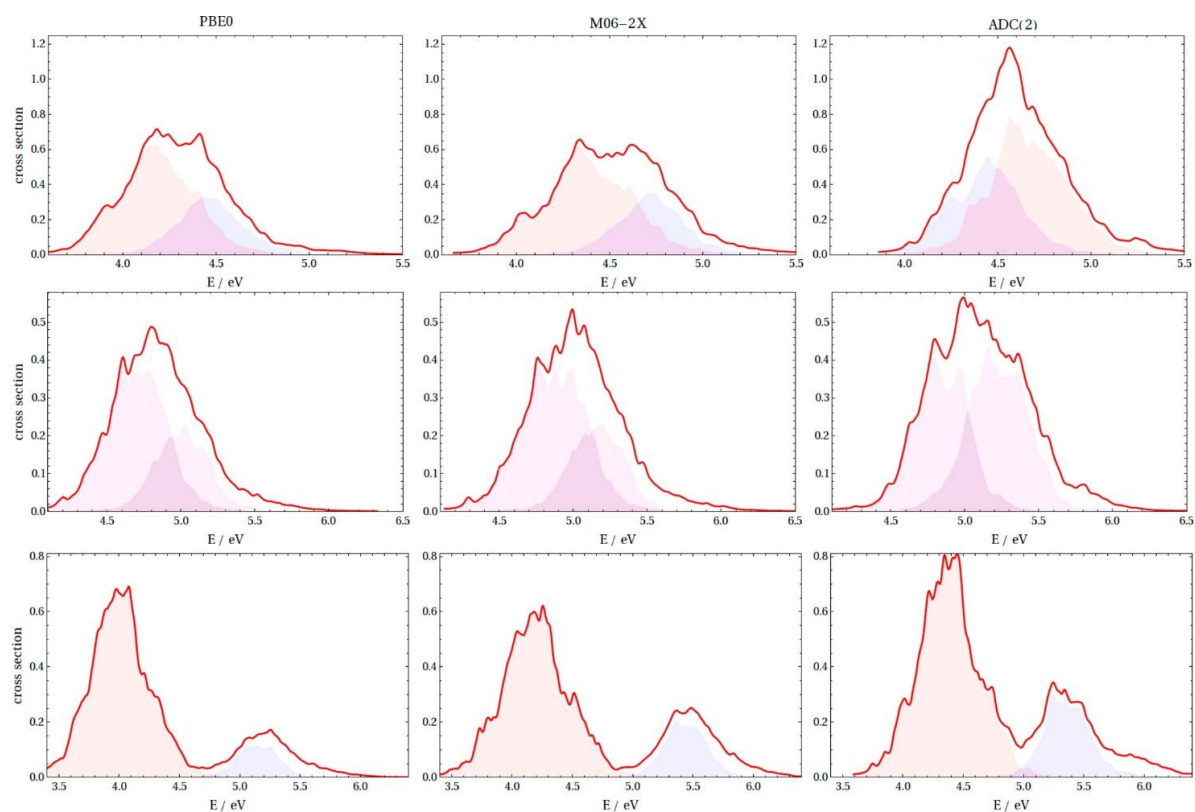


Figure 7.4 Photoabsorption spectra computed from the Wigner distribution (red line) of dithienothiophene (first row), thienothiophene (second row), and bithiophene (third row). The dithienothiophene and thienothiophene spectra were decomposed into contributions from S_1 and S_2 and S_1 and S_3+S_4 in the case of bithiophene. The color code reflects the main excitation character (in line with Figures 7.1 and 7.2). The same color is used for the bands of thienothiophene to reflect the character ambiguity. The cc-pVTZ basis set was used.

Finally, it is instructive to examine the impact of the preceding observations on the excited state geometries. The inversion of the states seen for ground state equilibrium geometries has little meaning as molecules that relax in the excited state can adopt conformations far from the Franck–Condon region. The PBE0, M06-2X, and ADC(2) optimized minima of the excited state with the initial A_1 symmetry (Figure 7.2) of thiophene are displayed in Figure 7.5a. ADC(2) predicts the S-puckered minimum, whereas TDDFT converged to the C-puckered structures. The C_s -symmetric S-puckered geometry is a transition state at the TDDFT level, as pointed out by Marian *et al.*⁷⁶ On the other hand, both DFT-MRCI⁷⁶ and CASPT2⁷⁸ ($\delta_{\text{CCCS}} = 26.7^\circ$) optimizations confirm the S-puckered structure as being a minimum. Slightly

different S-puckered minima are found when the B₂ state is optimized with both PBE0 and M06-2X (Figure 7.5b), albeit not with ADC(2). Actually, reoptimization of the TDDFT structures with ADC(2) leads to an intersection with the ground state, consistent with CASPT2 computations of Stenrup,⁷⁸ suggesting that B₂ may be unbound. Even more surprising are the S₁ geometries of thienothiophene and dithienothiophene (Figure 7.5c and 7.5d), for which large discrepancies exist for both the geometries and the vertical excitation energies when the two functionals are compared to ADC(2). For both systems, ADC(2) leads to tilted structure, whereas the two functionals prefer nearly planar frameworks. These systems were recently investigated by Jacquemin *et al.*, who looked at how solvation models affect excited state geometries.³¹³ Despite the different purpose of that work, we noticed that the quality of the results obtained with the usually reliable M06-2X functional should be taken with care. In contrast to previous examples, good agreement is achieved for the S₁ minimum of bithiophene. All three methods predict the well-known planar quinoidal structure that shows the characteristic alternation of single and double bonds with only slight disagreement in the lengths of the terminal C–C bonds (see ESI).

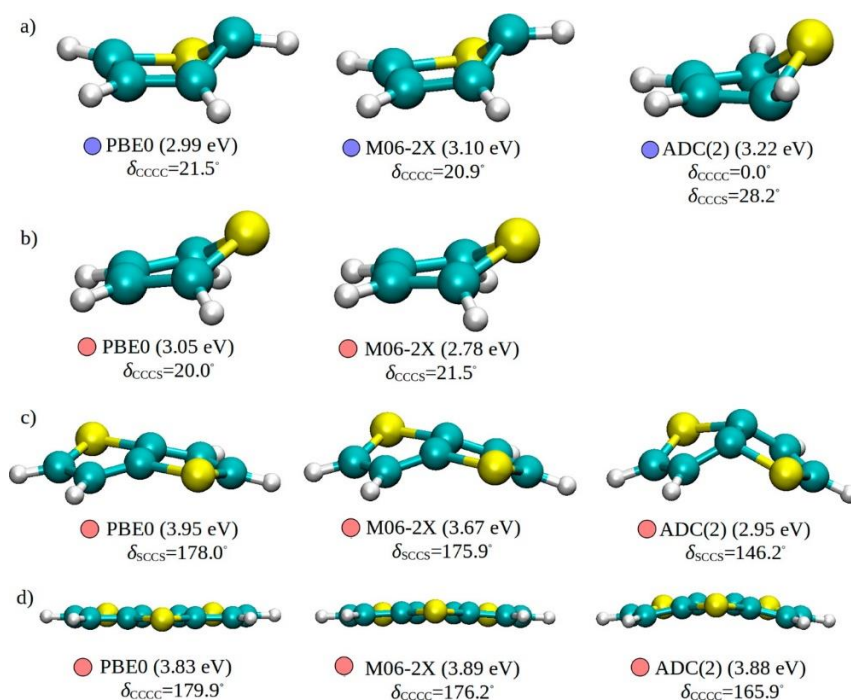


Figure 7.5 Minima at the S₁ adiabatic potential energy surface of: (a, b) thiophene, (c) thienothiophene, and (d) dithienothiophene. We report the vertical excitation energies (in parentheses), the dominant orbital excitations at given geometry (denoted by red and blue circles as in Figures 7.2 and 7.3), and the relevant dihedral angles. δ_{CCCC} of dithienothiophene denotes the dihedral angle between the middle and the side ring. The cc-pVTZ basis set was used.

To summarize, we demonstrated the problematic performance of TDDFT for the two lowest $\pi\pi^*$ states of thiophene and short thienoacenes. The failures include incorrect state ordering, poor distribution of oscillator strengths, and erroneous descriptions of critical points on the excited state potential energy surfaces. Similar trends are also identified for furan and its fused derivative (see ESI), but without the spurious inversion. What makes the thiophene example unique with respect to the furo- and oligoacene compounds is the large oscillator strengths of the two states involved and the experimental relevance. The incorrect state ordering and oscillator strengths thus notably impact the computed absorption spectra. In addition, serious discrepancies were found between TDDFT and ADC(2) optimized excited state geometries. These qualitative failures directly affect the possible prediction of adiabatic excitation energies and photoemission properties. Achieving accurate potential energy surfaces is also crucial for excited state molecular dynamics simulations, for which inexpensive TDDFT is often the method of choice. More generally, the present study

emphasizes the importance of systematically carrying out careful comparisons with more accurate wavefunction-based methods.

7.1 Computational methods

Ground state optimized structures and vibrational frequencies were obtained at the M06/DGDZVP³¹⁴ level with the Gaussian09¹⁰⁷ program package. Excited states were analyzed in their respective point groups: C_{2v} for thiophene, furan, and dithienothiophene, C_{2h} for thienothiophene and furofuran, C_2 for bithiophene, and C_s for terthiophene. Excitation energies were computed with Gaussian09 (M06, M06-2X, ω B97x-D, LC-PBE, LC-PBE*, TD-HF, CIS/CIS(D), EOM-CCSD, SAC-CI), Turbomole 6.5⁹⁸ (PBE, PBE0, TDA(PBE0), B3LYP, ADC(2), CC2), and Orca 3.0.2³¹⁵ (TDA-B2PLYP), and numerical values are given in ESI (Tables 1 and 2). In ADC(2) and CC2 computations, we apply the resolution of identity and the frozen core approximations. For the B2PLYP computations, the resolution of identity was employed. M06 and M06-2X computations use an ultrafine integration grid. SAC-CI is performed with the default parameters and convergence criteria of the Gaussian09 program. The CIS(D) oscillator strengths in Figures 7.2 and 7.3 are taken from CIS. LC-PBE* computations were performed by tuning the range separation parameter γ to match the HOMO energy and the difference between the total energies of the cation and neutral molecule. All the excitation energies were converged at the cc-pVQZ level, unless otherwise specified. Comparisons with smaller and augmented basis sets show a small and systematic deviation for two valence excitations. To reduce the computational burden, the photoabsorption spectra and excited state geometry optimizations were performed with the cc-pVTZ basis set. Excited state geometries were optimized with Turbomole 6.5 (PBE0, ADC(2)) and Gaussian09 (M06-2X) with tight convergence criteria and no symmetry constraints. The nuclear configurations used for spectral simulations were sampled by an uncorrelated Wigner distribution in the ground state,^{95,96} as implemented in Newton-X package.⁹⁷ A total of 500 structures were taken for each compound and vertical excitation energies and oscillator strengths were computed. Each transition was broadened by a Lorentzian using a phenomenological width of 0.05 eV. The spectra were decomposed into contributions from different states and the main character was assigned according to the dominant orbital excitations. Molecules, orbitals, and difference densities were visualized with VMD 1.9.1 program package.⁹⁹

Chapter 8 Low-Lying $\pi\pi^*$ States of Heteroaromatic Molecules: A Challenge for Excited State Methods

The Chapter is published as: Prlj, A.; Sandoval-Salinas, M. E.; Casanova, D.; Jacquemin, D.; Corminboeuf, C. *J. Chem. Theory Comput.* **2016**, *12*, 2652-2660.

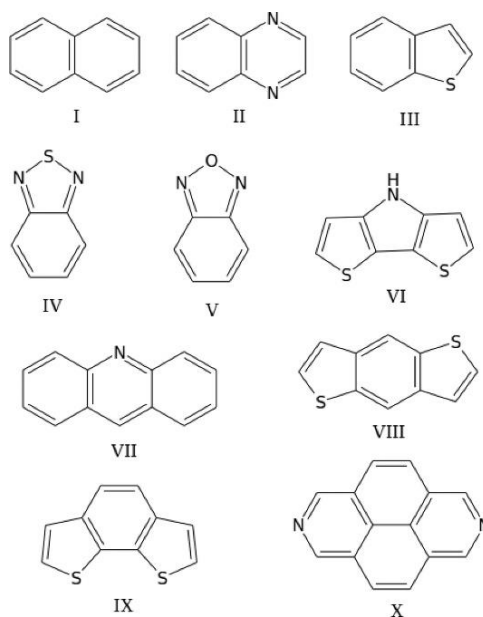
8.1 Introduction

The extensive computational investigations of (hetero)aromatic systems were prompted by the importance and broad applications of these compounds in organic electronics. In particular, the investigations of electronically excited states with theoretical tools should allow not only an in-depth understanding of the properties of known molecules but also the efficient design of new compounds. In this context, time-dependent density functional theory (TD-DFT)^{11,19} within its standard approximations (*i.e.*, the linear-response, adiabatic approximation) has become the primary framework,¹⁰⁸ mainly due to its good compromise between accuracy and computational efficiency. Out of the many distinct types of molecular excitations present in conjugated molecules, local $\pi\pi^*$ states (with prevailing single excitation character) are typically considered as the least problematic for TD-DFT. In π -conjugated systems, these states are of great relevance for both absorption and emission properties,^{113,316–318} and they play a major role in determining available decay channels.^{37,152,204,207}

Despite the general reliability of TD-DFT, several investigations uncovered sizable errors in the description of low-lying $\pi\pi^*$ states of fairly simple organic compounds. For instance, in 2001 Grimme *et al.*³⁰⁰ reported an imbalanced description of the two lowest singlet states of oligoacenes, L_a and L_b . The L_a and L_b notation³¹⁹ was originally introduced for polycyclic alternant hydrocarbons with L_a corresponding to the bright state of dominant HOMO \rightarrow LUMO character and L_b corresponding to the dark state encompassing nearly equal contributions from the HOMO–1 \rightarrow LUMO and HOMO \rightarrow LUMO+1 transitions. The low oscillator strength of the L_b state was explained by the cancellation of the transition dipole moments associated with these two contributions.³²⁰ As emphasized in ref. [300], the L_a excitations are significantly underestimated by standard local and semilocal functionals (such as the popular PBE³²¹ and B3LYP³²²), with a state order inversion in the case of naphthalene and a large excitation energy downshift for larger acenes. Due to the fundamental importance of oligoacenes, the conundrum has gained significant interest in the literature.^{301–304,316,323–333} Large improvements of the L_a excitation energies were later reported with the use of range-separated hybrid functionals,^{301–304} however at the expense of deteriorating the L_b excitation energy values.³⁰¹ The difficulty to provide a balanced description was attributed to the significant impact of contributions from double-excitation (mainly for L_b), that cannot be properly described with the standard adiabatic TD-DFT implementations.³²⁷ Therefore, the L_a - L_b problem originates from the description of both states. Indole (a building block of tryptophan amino acid) and several structurally related compounds were found to behave similarly.^{334–336} Indeed, it was shown³³⁵ that both hybrid and *meta*-GGA functionals predict a wrong ordering of the L_a and L_b $\pi\pi^*$ states, whereas range-separated hybrid functionals, despite providing a qualitatively correct ordering of the states, predict much too small energy gaps compared to the experimental values. The inversion of the L_a and L_b states was also spotted for 9H-adenine³³⁷ by comparing TD-DFT estimates to high level reference values obtained with wave function-based approaches, such as EOM-CCSD(T)³³⁸ (equation of motion-coupled cluster singles and doubles with perturbative triples) or CASPT2²⁹² (complete active space second-order perturbation theory), even though the ambiguity still remains in this case.³³⁷ More recently, two of us

have unraveled similar discrepancies for the low-lying $\pi\pi^*$ states of thiophene and thienoacenes,⁸⁰ which constitute popular building blocks in organic electronics. Regardless of the exchange-correlation functional used, we found not only a spurious state inversion but also a wrong distribution of oscillator strengths and erroneous potential energy surfaces. In contrast to TD-DFT, the performances of the several correlated single reference methods including contributions from double excitations such as CC2³⁰⁶ (approximate coupled cluster singles and doubles) and ADC(2)²² (algebraic diagrammatic construction up to second-order) were found rather satisfying.^{80,152}

The present contribution explores L_a - and L_b -like excitations in a large and diverse set of fused aromatic and heteroaromatic compounds (Scheme 8.1). These are typically the lowest $\pi\pi^*$ excited states in the spectrum and are consequently of huge chemical and physical relevance. In contrast to earlier case studies, dealing mostly with oligoacenes and occasionally with specific compounds relevant to applications, here we generalize the problem to a broader class of heteroaromatic molecules and propose a simple diagnostic for identifying these challenging excited states. Our objective is to pinpoint the excited state methods providing a properly balanced description of the two states. We critically examine the performance of standard TD-DFT, using several functionals and wave function based approaches (ADC(2) and CC2) as well as nonstandard TD-DFT based (spin flip (SF),¹⁵ double hybrid²⁶³) methods, that are all likely to be used for “real-life” applications due to their reasonable computational costs. The paper is organized as follows. In Section 8.2, we provide computational details. In Section 8.3, the naphthalene example is used as an illustrative case, followed by the examination of three exemplary heteroaromatic systems and the overall analysis of the excitation energy trends for ten different compounds. Concluding remarks are given in Section 8.4.



Scheme 8.1 Investigated Heteroaromatic Compounds

8.2 Computational Details

The optimized structures and corresponding transition energies are listed in the Electronic Supporting Information (ESI). If not stated otherwise, the *aug-cc-pVTZ*¹¹⁸ atomic basis set was used throughout.

Ground state geometries were optimized at the MP2 level (employing the resolution of identity, RI)³³⁹ using the Turbomole 6.5 package.⁹⁸ Excited state computations with TD-DFT (PBE and PBE0¹⁰⁰ functionals), CC2, and ADC(2) (which can be seen as an approximation to CC2)²⁸ were performed with Turbomole 6.5. The latter two methods were employed using the frozen core approximation and the RI approach (with an auxiliary *aug-cc-pVTZ* basis set taken from the Turbomole library).³⁴⁰

TD-DFT computations with the M06-2X,³⁴¹ M06-HF,³⁴² BHHLYP,^{343,344} ω B97X-D,³⁴⁵ and LC-PBE*³⁴⁶ functionals, as well as TD-HF calculations,¹² were performed with Gaussian09 (version D.01).¹⁰⁷ For both M06-2X and M06-HF, the *ultrafine* integration grid was employed to ensure numerical stability. Note that the long-range corrected LC-PBE functional was optimally tuned (here notation LC-PBE*) according to the nonempirical procedure described in ref. [305]. As such, the range separation parameter γ was optimized to minimize the function $|\epsilon_H^V(N)+IP^V(N)| + |\epsilon_H^V(N+1)+IP^V(N+1)|$, where ϵ_H^V is the energy of the HOMO orbital and IP^V is the vertical ionization potential of the neutral (N) and anionic ($N+1$) system, N being the number of electrons. For those systems (I, III, VI, VIII, and IX in Scheme 8.1) where the HOMO level of the anion was close to zero or positive (indicating an unbound electron), the tuning was solely based on the HOMO of the neutral system, *i.e.*, the function $|\epsilon_H^V(N)+IP^V(N)|$ was minimized by varying γ . For some systems, the default SCF convergence parameters led to higher energy solutions for the cation, typically resulting in large IPs and large optimal γ values. The Stable=Opt approach implemented in Gaussian was then used to ensure the convergence to the lower energy solution. CIS/CIS(D)³⁰⁷ and B2LYP/B2PLYP²⁶³ (within the Tamm-Dancoff approximation¹⁶⁶) computations were performed with the Orca 3.0.2 software.³¹⁵ Here B2LYP denotes a global hybrid functional (53% of exact exchange) that is underlying the B2PLYP double hybrid.

In addition, low-lying transitions were computed with the spin-flip (SF) version of TD-DFT (SF-DFT)¹⁵ in combination with BHHLYP, *i.e.*, SF-BHHLYP.¹⁵ Excitation energies were also computed with the algebraic diagrammatic construction up to third-order (ADC(3)).³⁴⁷ Due to the steep computational scaling of this method (M^6) and large memory requirements (M^4), where M is the number of basis functions, the ADC(3) computations were converged with a smaller *aug-cc-pVDZ*¹¹⁸ atomic basis set. To obtain our ADC(3) best estimates, basis set corrections based on ADC(2) computations (*i.e.*, $E(\text{aug-cc-pVTZ})-E(\text{aug-cc-pVDZ})$) were added to the ADC(3)/*aug-cc-pVDZ* values. Due to the generally weak basis set dependence of the $\pi\pi^*$ states, these ADC(3) best estimates are expected to be close to the actual ADC(3)/*aug-cc-pVTZ* values. SF-BHHLYP and ADC(3) computations were performed with the Q-Chem 4.3 package.³⁴⁸

The spectral simulations of acridine (compound VII in Scheme 8.1) were performed with the Newton-X package.⁹⁷ The nuclear configurations used for the spectral simulations were sampled by an uncorrelated Wigner distribution^{95,96} in the ground state (the Hessian was obtained by reoptimizing the structure at the PBE0/*aug-cc-pVDZ* level with the Turbomole package). 200 structures were taken, and the vertical excitation energies and oscillator strengths were computed at both the TD-PBE0 and ADC(2) levels using the *aug-cc-pVDZ* atomic basis set. The transitions were broadened by a Lorentzian using a phenomenological width of 0.05 eV.

8.3 Results and Discussion

8.3.1 The Case of Naphthalene L_a and L_b States

We selected naphthalene, an intensively studied example, to serve as a prototype example for the excitation energy trends found in fused (hetero)aromatic compounds. Naphthalene allows for the illustration of the major issues regarding the imbalanced description of the two lowest $\pi\pi^*$ states. First, let us provide an overview of the main conclusions raised in the literature. Although most of the qualitative results shown in Figure 8.1 have been described previously,^{300–304,327} they were recomputed here to minimize the impact of using different ground state geometries and diverse atomic basis sets. Additional insights are also obtained from the CIS/CIS(D), SF-BHHLYP, and ADC(3) results.

As pointed out in Grimme's seminal study,³⁰⁰ local and semilocal functionals such as PBE (generalized gradient approximation, GGA functional, 0% of exact exchange) and PBE0 (global hybrid functional, 25% of exact exchange) severely underestimate the L_a excitation energies and provide incorrect state ordering (left, Figure 8.1). As a side note, we remind that some improvements were reported when Tamm-Dancoff approximation (TDA) was used (it fixes the state order when combined with PBE0 although the energy gap remains rather inaccurate).³⁴⁹ While TDA was found beneficial in some studies,^{328,349,350} in others the improvements were attributed to a fortuitous cancellation of errors.³⁰¹ We will return to TDA later in the text. The inclusion of a larger portion of exact exchange as in M06-2X (*meta*-GGA hybrid, 54% of exact exchange) or in range-separated hybrid functionals such as ω B97X-D and LC-PBE* not only upshifts the HOMO \rightarrow LUMO (L_a) state toward the reference value but also overshoots the energy of the L_b state. Consistently

with its accurate description by range-separated functionals, the L_a state shows some similarities with charge transfer states and was called “charge transfer in disguise”³⁰¹ or “charge transfer-like excitation”.³⁰² Nevertheless, according to standard analysis tools, such as the Tozer Λ diagnostic based on the overlap between the MOs,³⁰³ there is no net charge transfer,³⁰¹ and both states can be characterized as local $\pi\pi^*$ excitations. Alternatively, the valence bond picture describes L_a and L_b as ionic and covalent states, respectively.^{323,351} The CIS/CIS(D) excitation energies bring up a relevant trend. Unlike L_a , the L_b state is highly sensitive to the differential correlation effects introduced by the perturbative correction for contribution from double excitations. We note that, in contrast, the CASSCF analysis of the L_b state wave function shows the dominant contributions from single excitations,³⁵¹ but it still misses important contributions from the dynamic correlation. A more detailed analysis with a high level post-Hartree–Fock method (CC3, coupled cluster singles, doubles, and triples³⁵²) reveals 15% of non-singles, compared to the 10% in L_a .³¹⁶ Therefore, it is not surprising that the description of the L_b state is rather problematic at the TD-DFT level. This issue was already recognized by Grimme *et al.*³²⁷ who applied double hybrid functionals to the series of linear and nonlinear acenes, obtaining significant improvements over standard TD-DFT computations. As shown in Figure 8.1, B2PLYP indeed produces excitation energies comparable to correlated single reference methods with explicit contributions from the doubles, such as CC2 and ADC(2).

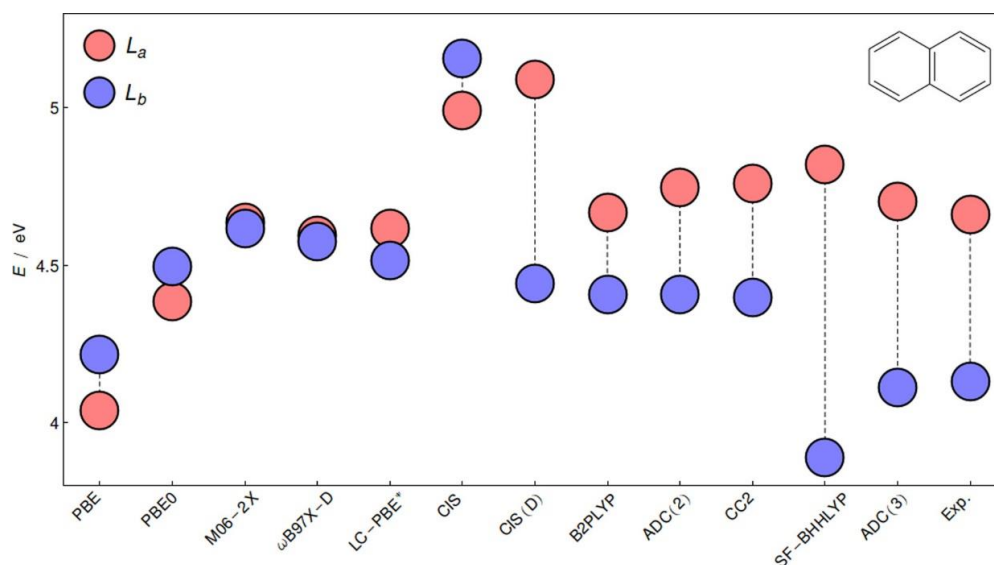


Figure 8.1 Computed excitation energies of the L_a (red) and L_b (blue) excited states of naphthalene compared to the experimental estimates taken from ref. [300]. The *aug-cc-pVTZ* basis set was used; see Computational Details for ADC(3).

While SF-BHHLYP provides a rather balanced description of the L_a/L_b states in naphthalene, these results deserve a closer analysis. The transition energy to L_a is slightly overestimated. On the other hand, SF-BHHLYP underestimates the L_b energy, *i.e.*, it shows the behavior opposite compared to TD-DFT when similar exchange-correlation functionals are used. To understand this difference, one should stress that the SF excitation scheme is best suited for the study of small HOMO to LUMO gaps and for the computation of states with the main contributions coming from HOMO \rightarrow LUMO and (HOMO)₂ \rightarrow (LUMO)₂ transitions. Although other electronic transitions can be computed with SF-DFT, the final expression for these states is not spin complete.³⁵³ This is precisely the situation for the L_b state, for which SF-BHHLYP generates a broken-symmetry solution, that is, the mixing between the singlet and triplet L_b states.

Regarding the experimental values, it is important to note that as the computed vertical excitation energies are not experimental observables, they should not be compared to the experimental band maxima directly but preferably to the results obtained with higher levels of theory.³⁵⁴ The experimental estimates of vertical excitation energies shown in Figure 8.1 were back corrected³⁰⁰ from the accurate measures of adiabatic excitation energies. The resulting energies values (4.13 eV for L_b and 4.66 eV for L_a) compare very well with our ADC(3) estimates (4.11 eV for L_b , 4.70 eV for L_a) as well as with earlier CASPT2 computations (4.03³⁵⁵/4.24³¹⁶/4.06³⁵⁶ eV for L_b , 4.56³⁵⁵/4.77³¹⁶/4.49³⁵⁶ eV for L_a).

Predictions from other high level methods include CR-EOM-CCSD(T) (4.13 eV for L_b and 4.79 eV for L_a)³²⁶ and CC3 (4.27 eV for L_b and 5.03 eV for L_a ; a triple- ζ atomic basis set with no diffuse functions was used).³¹⁶ Despite some spread of excitation energies, each of these methods predict relatively large interstate gaps, which is not the case for the lower level methods. Overall, TD-DFT energies are clearly dependent upon the extent of exact exchange, but none of the functionals provides a simultaneous good description of both states. Moderate improvements are achieved with wave function based (ADC(2), CC2) and more sophisticated TD-DFT based (double hybrid, spin flip) methods, but even these results suffer from significant errors. In the upcoming sections, we rely on ADC(3) reference values to evaluate the systematic shortcomings of different excited state methods on a larger number of heteroaromatic compounds. However, given the variations observed among high-level methods (as evident from the naphthalene example), we will restrict the forthcoming discussions to large quantitative deviations (*i.e.*, > 0.2 eV) as well as clear trends.

8.3.2 Criteria for L_a - and L_b -like States

A preliminary step necessary for the assessment of the performances of the different excited state methods is to distinguish the two states (*i.e.*, L_a - and L_b -like states) on the set of small and middle sized fused heteroaromatic systems. However, the definition of such states in terms of quasiparticle levels appears somewhat arbitrary, as in practice orbitals obtained from Hartree–Fock or generalized Kohn–Sham methods may be largely distorted when large and diffuse basis sets are used, giving rise to multiple contributions of orbital excitations with sizable coefficients.¹¹⁰ This is why we relied on natural transition orbitals (NTO) to distinguish between the states (see the ESI; also note that the NTO analysis is rather qualitative due to the neglect of correlation effects, the proper treatment of which is important for excitation energies and excited state properties). L_a is typically well described by a single pair of NTO, while L_b consists of two major configurations, which generally do not have equal weights. Also, in contrast to the oligoacenes, the L_b -like state can have oscillator strength as large as, or even larger than, the corresponding L_a state. Compounds with permanent dipole moment are characterized by a L_b state presenting a dipole of a magnitude similar to its ground state counterpart, while the values for the “ionic” L_a are typically larger (the exceptions are compounds VII and IX due to the more symmetric charge distribution).

The patterns of the L_a and L_b states for the set of Scheme 8.1 are less systematic than in the oligoacene series. The presence of heteroatom(s) induces some variations on the nature of the $\pi\pi^*$ transitions, such as character mixing with nearby $\pi\sigma^*$ and $n\pi^*$ states, or between the L_a and L_b states.³³⁶ For compound VIII, a moiety frequently found in organic electronics, there is even an ambiguity in determining the character of L_a and L_b since both states belong to the same irreducible representation and, therefore, mix (see the ESI for the assignment used herein).

8.3.3 Three Illustrative Compounds

Figure 8.2 provides the detailed analysis of three individual cases, *e.g.*, acridine, 2,1,3-benzooxadiazole, and benzo[2,1-*b*:3,4-*b'*]dithiophene (respectively VII, V, and IX in Scheme 8.1), that manifest the problem illustrated for naphthalene. The reference ADC(3) relative and absolute excitation energies of L_a and L_b differ significantly in these three compounds, which makes them interesting study cases. In particular, IX and V possess their lowest lying states at a similar energy and a similar energy gap, but the state ordering is reversed. In VII, both states are computed to be nearly degenerate at the ADC(3) level. As can be seen in Figure 8.2, the three distinct functionals, PBE, PBE0, and ω B97X-D, fail to reproduce both the absolute excitation energies and the excitation energy gaps predicted by ADC(3). There is a characteristic dependence of excitation energies on the amount of exact exchange, with a similar upshift for both L_a and L_b . For the three systems, ω B97X-D predicts the L_a state very close to ADC(3), illustrating its remarkable performance for states of dominant HOMO \rightarrow LUMO character. On the other hand, the same functional severely overestimates L_b (0.3 to 0.5 eV). The comparison between CIS and CIS(D) uncovers an essential trend: the perturbative double correction has a large impact on L_b but a much smaller impact on L_a . Considering the significant double excitation character of L_b , the apparent “good” performance of PBE and PBE0 for this state is most probably fortuitous. The double hybrid, B2PLYP, which incorporates a CIS(D)-like correction, improves upon standard TD-DFT and provides excitation energies comparable to ADC(2). Alternatively, the SF-BHHLYP results are rather unsatisfactory due to the dramatic

underestimation of the L_b excitation energy and the inconsistent description of L_a . Finally, ADC(2) (and similarly CC2), although being the closest to the reference, shows some lack of systematic behavior. Both L_a and L_b are slightly overestimated, though the trends are not perfectly equivalent for all compounds. While L_b is overestimated for VII, L_a is too high in V, whereas in IX the energy gap of ADC(3) is well reproduced due to the similar upshift for both states. In fact, this clearly shows that ADC(2)/CC2 might not be a sufficiently accurate benchmark to assess the quality of TD-DFT as already discerned in previous benchmark studies.^{316,357} Along this line, the performance of range-separated hybrid functionals might be even superior for excited states of HOMO \rightarrow LUMO character.

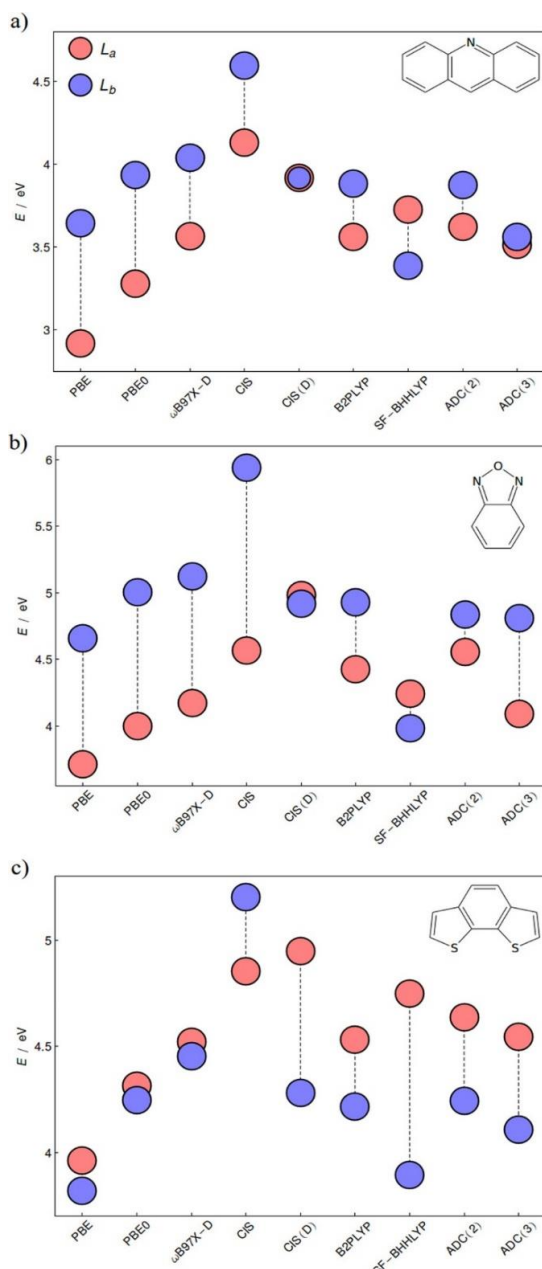


Figure 8.2 Computed excitation energies of the L_a (red) and L_b (blue) excited states of a) acridine, b) 3,1,3-benzooxadiazole, and c) benzo[2,1-*b*:3,4-*b'*]dithiophene with the *aug*-cc-pVTZ basis set; see Computational Details for ADC(3).

To further demonstrate that the discrepancies shown in Figure 8.2 have a major impact on the theoretical prediction of absorption properties, we computed the absorption spectra of acridine at two illustrative levels (Figure 8.3). Unlike anthracene, which has an optically dark L_b state, the oscillator strength of L_b in the widely used acridine dye is similar to L_a . Because of the large gap between the two states, PBE0 predicts two distinct peaks, while ADC(2) predicts two overlapping peaks, which is consistent with the experiment.³⁵⁸

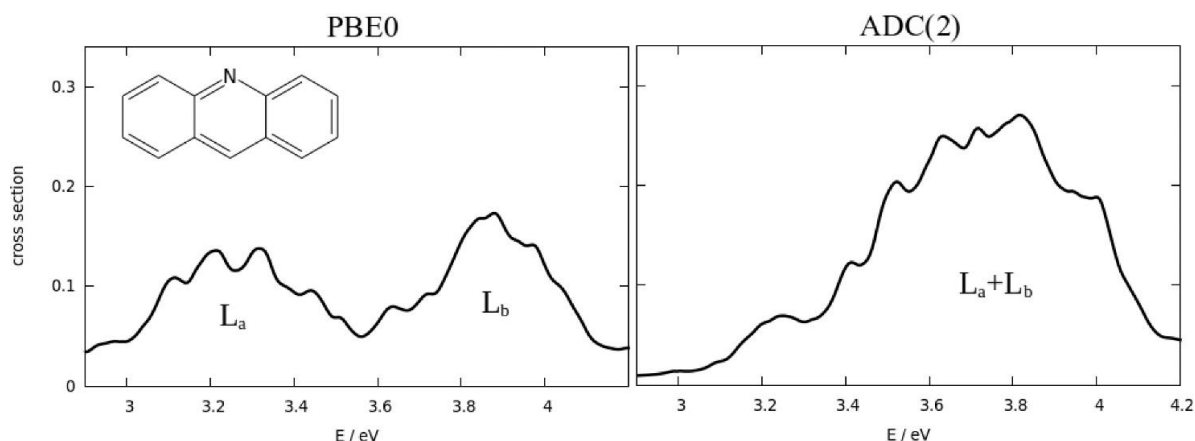


Figure 8.3 Photoabsorption spectra of acridine computed from the Wigner distribution, employing PBE0 and ADC(2) combined with *aug-cc-pVDZ*.

8.3.4 Statistical Analysis of Excitation Energy Trends

The mean signed deviation for each excited state method (Figure 8.4) best illustrates the overall performances and general trends associated with the set of compounds represented in Scheme 8.1. The corresponding mean absolute deviations can be found in the ESI. In line with the individual molecular cases, the most striking feature is the difference between CIS and CIS(D). CIS severely overestimates the excitation energies of both L_a and L_b , and the L_b state energy goes down by a large amount (*ca.* 0.8 eV) when including the correction for the contribution of the doubles. In contrast, L_a is rather constant. Given that this effect is characteristic for all the investigated compounds, the CIS/CIS(D) computations ideally serve as a simple diagnostic for identifying the L_a - and L_b -like states in real life applications: the excitation energies of L_b states are much more sensitive to the dynamical correlation effects, that are absent in CIS. In addition, the overestimation of the ionic L_a state is rationalized by the well-documented CIS large positive bias for charge transfer states.³⁵⁹ The introduction of the second order perturbative corrections clearly improves the description but remains insufficient to provide well-balanced excitation energies. A more balanced picture is achieved with CC2 and ADC(2). The two methods give practically the same energies in line with earlier studies.^{82,360} The averaged overestimations of both the L_a and L_b states are around 0.15 and 0.20 eV, respectively, indicating the reliability of both methods for practical applications on medium-sized organic molecules. Nevertheless, the shifts of each state are not systematic (see for instance the naphthalene example in Figure 8.1, where L_a is well positioned but L_b is overestimated, and the irregular deviations for the individual compounds in Figure 8.2), and the similar mean signed deviation for the two states are somewhat misleading. These scattered results illustrate that the treatment of correlation is still incomplete in ADC(2) and CC2. The correlation effects are albeit crucial (as it is apparent from CIS results) to obtain accurate energies for both states.

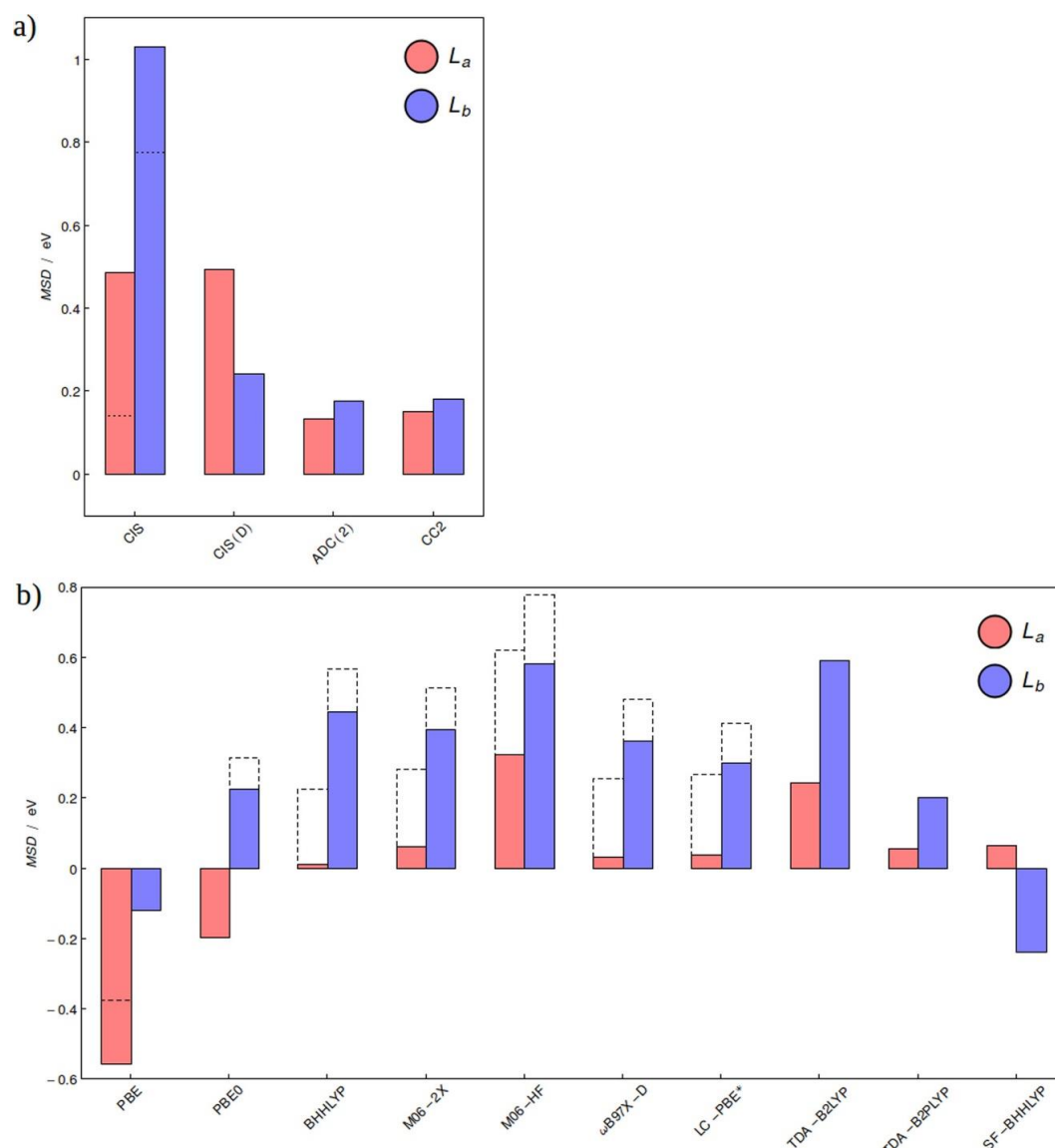


Figure 8.4 Mean signed deviations of the L_a (red) and L_b (blue) states of compounds in Scheme 8.1 obtained by comparison of a) wave function and b) TD-DFT based methods to ADC(3) reference. Bars with dashed lines correspond to the results with TDA, while dotted lines on top of the CIS correspond to TD-HF. The *aug-cc-pVTZ* atomic basis set was systematically used.

From the TD-DFT perspective, Figure 8.4b confirms that none of the tested functionals provides a balanced picture of the two relevant states. PBE severely undershoots the excitation energy of L_a , and the more accurate description of L_b is fortuitous. PBE0, which contains a moderate fraction of exact exchange, underestimates the excitation energies of the L_a states but to a smaller extent. Global hybrids with large amount of exact exchange (M06-2X and BHHLYP) as well as range-separated hybrids (ω B97X-D and LC-PBE*) improve the description of L_a , owing to its charge transfer-like character, but overshoot significantly the energy of L_b . This is valid for the optimally tuned variant, LC-PBE*, which does not improve the results in comparison with the range-separated hybrid functional with fixed γ , such as ω B97X-D (0.20 bohr⁻¹). The improvement of the HOMO \rightarrow LUMO excitation within the range-separation framework goes along with the more accurate quasiparticle energies. However, the amount of exact exchange that is optimal for L_a is not necessarily optimal for multiconfigurational L_b . It is of course possible to tune parameters to specifically minimize the L_b errors, but this is neither a practical nor satisfying solution. As noted earlier, frequency independent (*i.e.*, adiabatic) TD-DFT does

not perform well for excited states with strong configuration mixing.⁴ Alternatively a functional with 100% of exact exchange, M06-HF, severely overestimates the transition energies of both states. These results generally indicate that the TD-DFT errors for the L_a and L_b excitation energies are rather systematic and depend mainly upon the treatment of exact exchange.

Excitation energies obtained with TDA are systematically blue-shifted with respect to full TD-DFT (Figure 8.4b). The shift is similar for different functionals but somewhat larger when higher fractions of exact exchange are included. L_a is typically shifted more (~ 0.2 eV) than L_b (~ 0.1 eV). As seen earlier, CIS, being a Tamm-Dancoff approximation of the TD-HF scheme (dotted line in Figure 8.4a), also leads to an upshift of the computed excitation energies. In short, no general improvement originating from TDA can be identified as the accuracy is improved for the functionals underestimating the excitation energies but is deteriorated for the others (such as range-separated hybrids for L_a and L_b).

In comparison with standard TD-DFT, the double hybrid approach certainly delivers a more balanced treatment of L_a and L_b in heteroaromatic molecules. B2PLYP gives results similar to both CC2 and ADC(2), highlighting once again the importance of accounting for double excitations, for the L_b state. The SF-BHLYP energies follow the behavior already observed for the individual compounds, that is a slight overestimation of L_a for the same magnitude as non-SF TD-DFT energies with a similar amount of exact exchange and an underestimation of the L_b excitation energy.

The overall performance of the different approximations for the calculation of the energy gaps between the two states (see the mean absolute deviations in Figure 8.5) is also relevant given that the relative position of the excited states is sometimes more important than the absolute transition energies. Despite the uncertainty intrinsic to any excited state method, and also to the ADC(3) reference, the gap obtained from TD-DFT is systematically away from the reference values (~ 0.4 eV). Unbalanced gaps result, for various cases, in qualitatively incorrect state ordering. TDA reduces the errors for the gap between the two states, essentially because the shifts for L_a and L_b are not equivalent. CIS provides incorrect gaps, and significant improvements are achieved by CIS(D). The smallest (although still relatively large) deviations from the reference are obtained with (TDA)-B2PLYP, ADC(2), and CC2 methods.

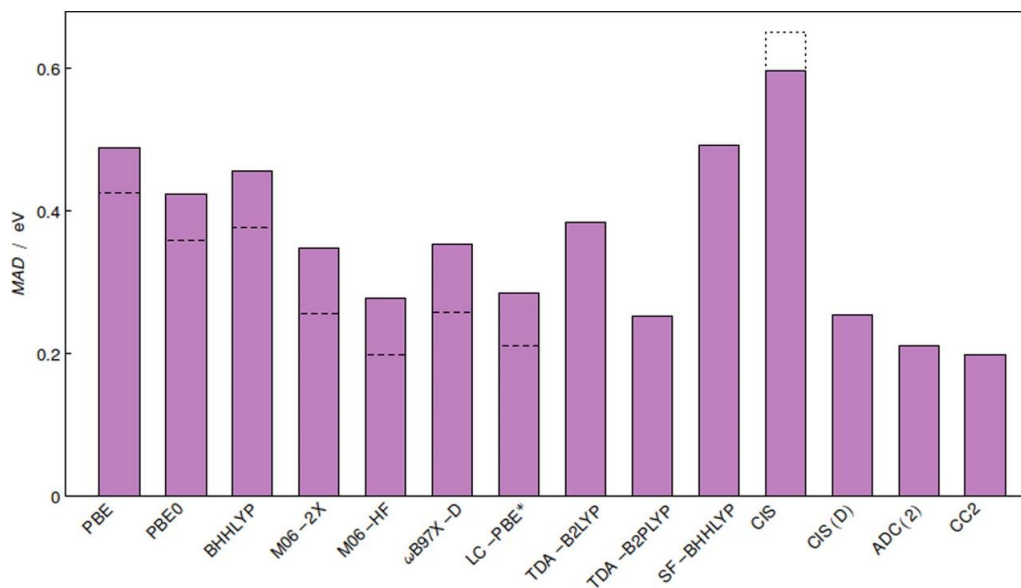


Figure 8.5 Mean absolute deviations of energy gaps (L_a - L_b) compared to the ADC(3) reference. Dashed lines correspond to the results with TDA, while dotted lines on top of the CIS correspond to TDHF. All results are obtained with the *aug-cc-pVTZ* atomic basis set.

8.4 Conclusions

We demonstrated and generalized the problem of the imbalanced description of L_a and L_b , which is well-known for oligoacenes, to a set of heteroaromatic-fused systems. A CIS/CIS(D) computational check was proposed as a simple

diagnostic for identifying these two problematic (typically lowest) excited states, with L_b being highly sensitive to the correlation effects introduced by the doubles (D) correction. A pronounced difference between the CIS/CIS(D) excitation energies is expected to foretell significant difficulties when employing the most widely used excited state methods. As a matter of fact, TD-DFT (within its standard approximations) does not provide balanced excitation energies nor accurate interstate gaps, which occasionally results in the spurious inversion of the states. Yet, TD-DFT outperforms CIS, thanks to the approximate treatment of correlation, absent in CIS. Pure DFT functionals and those with a small amount of exact exchange tend to underestimate the excitation energies of L_a . Functionals with a larger amount of Hartree–Fock-like exchange as well as range-separated hybrid functionals describe L_a very accurately but overestimate the energy of L_b . The benchmarking of such functionals exclusively on excited states with dominant HOMO \rightarrow LUMO character is therefore somewhat biased. Since changing the functional does not solve the overall issue, it is likely that the approximations used in standard TD-DFT (*i.e.*, adiabatic approximation) are at the origin of the problem. Some improvements over standard TD-DFT are achieved by using a double hybrid functional in which part of the correlation is described by *a posteriori* (D)-like correction. Spin-flip DFT, which is generally a very good approach for the description of low-lying energy states in molecules with diradical or triradical character, is not able to accurately reproduce the relative energies between L_a and L_b in heteroaromatic molecules. Better performances are obtained with ADC(2) and CC2 albeit higher levels of theory are necessary to reach high and robust accuracy.

Chapter 9 Intramolecular Symmetry-Adapted Perturbation Theory with a Single-Determinant Wavefunction

The Chapter is published as: Pastorczak, E.[†]; Prlj, A.[†]; Gonthier, J. F.; Corminboeuf, C. J. Chem. Phys. 2015, 143, 224107. (†contributed equally)

9.1 Introduction

Aside from the strong covalent and ionic bonding, there exists a plethora of powerful interactions occurring between atoms and molecules. These non-covalent interactions include hydrogen³⁶¹ and halogen³⁶² bonds, dipole-dipole interactions, charge transfer, $\pi - \pi$ stacking, dative bonds,³⁶³ agostic interactions,³⁶⁴ as well as cation- π ³⁶⁵ and anion- π ³⁶⁶ interactions and many more.³⁶⁷ Even if those interactions are more frequently associated with intermolecular complexes, their role within molecules is equally crucial, as illustrated by their impact on catalytic processes,³⁶⁸ reaction barrier heights,^{369,370} molecular geometries³⁷¹ or protein tertiary structures,³⁷² to name a few.

These interactions can be probed based on experiments^{373–377} but computational techniques have played an increasingly important role over the last two decades. Those are essentially divided into two categories: the approaches that are primarily qualitative and reveal the presence of an interaction through the visualization of electron density-based functions; and methods, which provide a quantitative description of the nature of the interaction. The former category includes, for instance, the Noncovalent Index (NCI)³⁷⁸ or the recent Density Regions Overlap Indicator (DORI).²⁵¹ A unique approach, combining both quantitative and qualitative features, is Bader's Quantum Theory of Atoms in Molecules (QTAIM),³⁷⁹ which employs topological analysis of the electron density to reveal the existence and gain some insight into the nature of non-covalent interactions. Alternatively, various quantitative approaches have been developed to decompose the total interaction energy between molecules into physically meaningful components. Among these "energy decomposition analysis" (EDA) schemes, the most prominent are: the Kitaura-Morokuma scheme,³⁸⁰ the local Møller-Plesset perturbation theory (LMP2)³⁸¹ and other linear-scaling fragment approaches.^{382–384} The interaction energy terms can also be extracted through relaxing the strictly localized molecular orbitals in a field of other molecules (*e.g.*, BLW-EDA,³⁸⁵ ALMO³⁸⁶). Symmetry Adapted perturbation theory (SAPT)³⁸⁷ is a highly popular alternative, in which the interaction between monomers is introduced as a perturbation and the components of this perturbation are interpreted as electrostatics, exchange, induction, and dispersion contributions. There exist different variants and implementations of SAPT including the highly accurate and computationally efficient version in PSI4,^{388,389} enabling the treatment of fairly large systems, such as host-guest complexes involving DNA³⁹⁰ or carbon nanotubes.³⁹¹ A clear advantage of SAPT is the easy interpretation of the results and its firm theoretical ground.³⁸⁷ Recently, Parrish and Sherrill developed a more fine-grained approach to partition the energy components into pairwise contributions from atoms or functional groups (ASAPT/FSAPT) and to visualize the results.^{392,393}

Unfortunately, none of the above approaches are ideally suited for analyzing the subtler non-covalent intramolecular interactions, although the existence of such a method would be highly valuable. The preliminary efforts to fill this gap and to expand the field of applicability of EDA schemes to a single molecule was recently accomplished by two of us with the derivation of a zeroth-order wavefunction,⁷ a necessary first step towards intramolecular SAPT (as seen later, it is this wavefunction that is exploited in the present implementation). A very practical alternative, closer to standard intermolecular SAPT methods, has recently been introduced by Parrish *et al.*³⁹⁴ This ISAPT method is built upon the

functional-group SAPT³⁹³ and adapts ideas from density matrix embedding to select the interactions and to build a zeroth-order wavefunction. The latter is then used directly in the conventional intermolecular SAPT expression. As will be seen, the method introduced here is a genuine intramolecular version of SAPT based on a novel set of expressions that makes use of the previously introduced zeroth-order expression.⁷ This preliminary work has also motivated the combination of fragmentations schemes with a generalized Kohn-Sham based EDA³⁹⁵ scheme that enable the analysis of intramolecular interactions, OH- π , and cation- π bonding. With the growing realization that non-covalent interactions play a significant role,^{396,397} even in medium-sized molecules,³⁹⁸ there is little doubt that an expanded arsenal of methods and strategies to analyze them will continue to emerge.

The paper is organized as follows: in Section 9.2, we invoke the zeroth-order wavefunction of Gonthier and Corminboeuf⁷ and construct a perturbation theory for intramolecular interactions for a single Slater determinant (SD) case. In Section 9.3, we describe the computational procedure and apply the new method to a set of illustrative molecular examples and validate its performance on intramolecular dihydrogen contacts, hydrogen bonds, $\pi - \pi$ interactions, and a positively charged host-guest complex. In Section 9.4, we discuss the abilities and limitations of the proposed method as well as the perspectives for future improvement.

9.2 Theory

9.2.1 The zeroth-order energy

The idea behind intramolecular SAPT (intra-SAPT) is analogous to the one of its intermolecular counterpart. First, the system is divided into fragments, the interaction between the fragments is then removed and subsequently brought back as a perturbation of the Hamiltonian. In comparison with the intermolecular scheme, the main difficulty here lies in the fact that the interacting fragments in question are not distinct monomers but selected regions within the same molecule. In quantum chemistry frameworks, all the electrons forming a molecule are described by a single wavefunction and therefore the electrons cannot be attributed to a particular atom. The electronic and nuclear partitioning is provided by Mayer's Chemical Hamiltonian approach (CHA).⁶ The CHA makes use of atom-centered basis set and interprets the products of the interaction operators and the one- and two-electron integral kets as the physical interactions, while the bras' role is projecting those interactions onto the basis set.

The chemical Hamiltonian approach has been originally devised to correct for the basis set superposition error (BSSE) when computing intermolecular interactions.^{399–401} In ref. [7], we showed that the same approach can be employed to probe intramolecular interactions.

As a first step toward devising a SAPT-based intramolecular energy decomposition scheme, a system (*i.e.*, a molecule or a complex) is partitioned into three fragments (note that the current implementation is limited to a three-fragment partitioning, see Figure 9.1), where the interaction of interest occurs between fragments A and B, with C acting as a linker. Fragment C is generally covalently bound to both A and B but non-covalently bound fragments can be considered as well. While the nuclear partitioning associated with fragments A, B, and C is straightforward, the trickier electronic partitioning is carried out through localizing subsets of electrons within each fragments using strictly localized orbitals (SLOs)⁴⁰² (also known under different terminology, see refs. [386,403–407]), which by definition have non-zero coefficients only on a small number of basis functions. In practice, our implementation proceeds as follows:

1. A Hartree-Fock (HF) computation is performed on the entire system.
2. The canonical HF orbitals are projected on fragments A, B, or C and then Löwdin-orthogonalized to obtain an appropriate set of guess orbitals.
3. The guess is used to build the Fock matrix \mathbf{F}_0 where interactions between A and B are eliminated according to following rules:
 - (a) The integrals where the product of the ket and the operator directly represents an interaction between A and B are deleted.

(b) For integrals representing interactions within fragment A (or fragment B), the bra basis functions on fragment B (or respectively, fragment A) are projected out.

4. To ensure that orbital locality is maintained, the Fock matrix is projected on fragment X (X = A, B, or C) using Stoll's algorithm⁴⁰² to get $\mathbf{F}_X^{\text{proj}}$.

5. The eigenequation $\mathbf{F}_X^{\text{proj}} \mathbf{S} \mathbf{C}_X = \epsilon_X \mathbf{S} \mathbf{C}_X$ is solved self-consistently for the orbitals \mathbf{C}_X with overlap matrix \mathbf{S} .

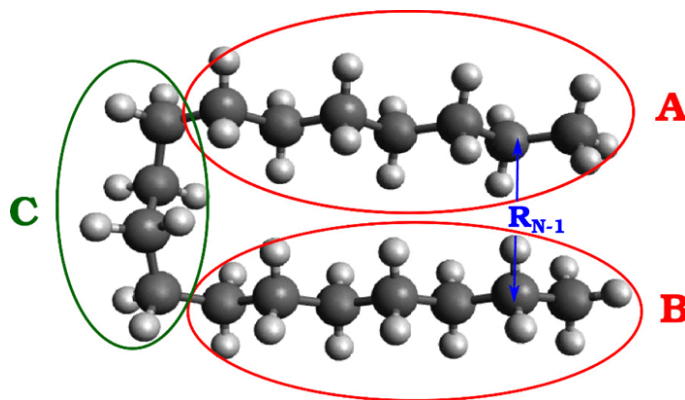


Figure 9.1 Backbone structure of a hairpin alkane partitioned into three fragments. Geometries are taken from ref. [408].

The eigenequation for the orbitals \mathbf{C}_X is solved under the constraint of strict orbital localization by employing Stoll's algorithm,⁴⁰² as described in more detail in ref. [7]. At convergence, one obtains occupied and virtual orbitals strictly localized on one fragment and their associated energies.

As shown in Appendix A (see original ref. [409]), the zeroth-order wavefunction obtained through the above equations is in fact the right eigenvector of the zeroth-order Hamiltonian \hat{H}_0 ,

$$\hat{H}_0 |\psi_0^{(0)}\rangle = E_0 |\psi_0^{(0)}\rangle \quad (9.1)$$

\hat{H}_0 is a non-Hermitian operator that can be written in closed form in second quantization (see Appendix A⁴⁰⁹). As a consequence, it possesses a left eigenvector $\tilde{\psi}_0^{(0)}$ used to rewrite the above equation,

$$E_0 = \langle \tilde{\psi}_0^{(0)} | \hat{H}_0 | \psi_0^{(0)} \rangle \quad (9.2)$$

The minimization of E_0 subject to the constraint of orbital localization yields the orbital optimization equations introduced above. Thus, our method is readily amenable to perturbation theory by examining the difference between the full Hamiltonian and \hat{H}_0 , which we do in Subsection 9.2.2. The obtained perturbation theory formulae are expressed in terms of the occupied and virtual orbitals \mathbf{C}_X and their energies.

9.2.2 Energy decomposition

Since both the zeroth-order Hamiltonian and the perturbation are non-Hermitian operators, the intramolecular perturbation is more easily formulated within a biorthogonal framework.^{399,410}

Then, the unperturbed Hamiltonian \hat{H}_0 corresponding to the 0-th order energy E_0 has different right and left eigenvectors. The right eigenvectors of \hat{H}_0 , $\{|\psi_j^{(0)}\rangle\}$, are not orthonormal to each other but are orthonormal to the left eigenvectors, $\{|\tilde{\psi}_k^{(0)}\rangle\}$ i.e.,

$$\langle \tilde{\psi}_k^{(0)} | \psi_j^{(0)} \rangle = \delta_{kj}. \quad (9.3)$$

The perturbation in the biorthogonal formulation (and second quantization notation) is expressed as a sum,

$$\hat{H} - \hat{H}^{(0)} = \hat{W}_{AB} + \hat{H}_{BE}, \quad (9.4)$$

where the first component on the right takes the following form:

$$\hat{W}_{AB} = \sum_{i \in A} \sum_k \langle \tilde{k} | \hat{V}_B | i \rangle k^+ \tilde{i}^- + \sum_{i \in B} \sum_k \langle \tilde{k} | \hat{V}_A | i \rangle k^+ \tilde{i}^- + \sum_{k \in A} \sum_{l \in B} \sum_{ij} \langle \tilde{i} \tilde{j} | kl \rangle i^+ j^+ \tilde{l}^- \tilde{k}^-, \quad (9.5)$$

where \hat{V}_A and \hat{V}_B are the electrostatic potentials of the nuclei of fragments A and B, respectively, and the biorthogonal spinorbitals $|\tilde{i}\rangle$ are defined by the relation

$$\langle \tilde{i} | j \rangle = \delta_{ij}, \quad (9.6)$$

while k^+ , \tilde{i}^- are, respectively, the non-Hermitian covariant creation and contravariant annihilation operators.⁴¹¹ Please note that in the above and the following equations where no other indication is given, the indices run over the entire set of orbitals.

The remaining component of the perturbation, \hat{H}_{BE} , is associated with basis set effects and does not contribute to the physical part of the AB interaction (see Appendix B⁴⁰⁹). It can thus be neglected.

The first order energy correction (including also the classical internuclear repulsion), $E^{(1)} = \langle \tilde{\Psi}^{(0)} | \hat{W}_{AB} | \Psi^{(0)} \rangle + \frac{1}{2} \sum_{I \in A, J \in B} \frac{Z_I Z_J}{R_{IJ}}$ then takes the form

$$E^{(1)} = \sum_{i \in A}^{occ} \langle \tilde{i} | \hat{V}_B | i \rangle + \sum_{i \in B}^{occ} \langle \tilde{i} | \hat{V}_A | i \rangle + \sum_{k \in A}^{occ} \sum_{l \in B}^{occ} \langle \tilde{k} \tilde{l} | kl \rangle + \sum_{I \in A, J \in B} \frac{Z_I Z_J}{R_{IJ}}. \quad (9.7)$$

First order correction (9.7) corresponds to the sum of Coulomb and exchange interactions between the fragments, although the exchange component cannot be isolated in the biorthogonal formulation.

The second-order correction takes the form

$$E^{(2)} = - \sum_{exc} \frac{\langle \tilde{\Psi}_{exc} | \hat{W}_{AB} | \Psi^{(0)} \rangle \langle \tilde{\Psi}^{(0)} | \hat{W}_{AB} | \Psi_{exc} \rangle}{E_{exc}^{(0)} - E_0^{(0)}} \quad (9.8)$$

where \sum_{exc} denotes a summation over all the excited determinants, and $E_{exc}^{(0)}$ are the zeroth-order energies of the excited states. It can be expressed as a sum of three components (for an extended description see Appendix C⁴⁰⁹),

$$E^{(2)} = E_{pol} + E_{deloc} + E_{disp}, \quad (9.9)$$

where

$$E_{pol} = - \sum_{a \in A} \sum_{b \in B}^{occ \text{ virt}} \frac{(\langle \tilde{a} | \hat{V}_B | b \rangle + \sum_{l \in B}^{occ} \langle \tilde{a} \tilde{l} | bl \rangle)(\langle \tilde{b} | \hat{V}_B | a \rangle + \sum_{l \in B}^{occ} \langle \tilde{b} \tilde{l} | al \rangle)}{\varepsilon_b - \varepsilon_a} - \sum_{a \in B} \sum_{b \in A}^{occ \text{ virt}} \frac{(\langle \tilde{a} | \hat{V}_A | b \rangle + \sum_{l \in A}^{occ} \langle \tilde{a} \tilde{l} | bl \rangle)(\langle \tilde{b} | \hat{V}_A | a \rangle + \sum_{l \in A}^{occ} \langle \tilde{b} \tilde{l} | al \rangle)}{\varepsilon_b - \varepsilon_a} \quad (9.10)$$

corresponds to the polarization energy,

$$E_{deloc} = - \sum_{a \in A} \sum_{b \in B}^{occ} \frac{(\langle \tilde{a} | \hat{V}_A | b \rangle + \sum_{l \in A}^{occ} \langle \tilde{a} \tilde{l} | b l \rangle)(\langle \tilde{b} | \hat{V}_B | a \rangle + \sum_{l \in B}^{occ} \langle \tilde{b} \tilde{l} | a l \rangle)}{\varepsilon_b - \varepsilon_a} - \sum_{a \in B} \sum_{b \in A}^{occ} \frac{(\langle \tilde{a} | \hat{V}_B | b \rangle + \sum_{l \in B}^{occ} \langle \tilde{a} \tilde{l} | b l \rangle)(\langle \tilde{b} | \hat{V}_A | a \rangle + \sum_{l \in A}^{occ} \langle \tilde{b} \tilde{l} | a l \rangle)}{\varepsilon_b - \varepsilon_a} \quad (9.11)$$

to the delocalization or charge-transfer energy and

$$E_{disp} = - \sum_{a \in A} \sum_{c \in B}^{occ} \sum_{b \in A}^{virt} \sum_{d \in B}^{virt} \frac{\langle \tilde{a} \tilde{c} | b d \rangle \langle \tilde{b} \tilde{d} | a c \rangle}{\varepsilon_d - \varepsilon_c + \varepsilon_b - \varepsilon_a} - \sum_{a \in A} \sum_{c \in B}^{occ} \sum_{b \in B}^{virt} \sum_{d \in A}^{virt} \frac{\langle \tilde{a} \tilde{c} | b d \rangle \langle \tilde{b} \tilde{d} | a c \rangle}{\varepsilon_d - \varepsilon_c + \varepsilon_b - \varepsilon_a} \quad (9.12)$$

to the London dispersion term. In eqs. (9.10)-(9.12), $\{\varepsilon_x\}_{x=a,b,c,d}$ denote orbital energies associated with the zeroth-order wavefunction.

The expressions for intramolecular interaction components (9.7) and (9.10)-(9.12) resemble the ones obtained by Surján *et al.*³⁹⁹ for intermolecular interactions (in fact they are identical in cases for which the linker is absent), but in the intra-SAPT formulas the presence of the middle fragment manifests itself through the orbitals and their energies. In the single-determinant approximation, the three- and higher-body terms are equal to zero in the first and second-order corrections. Note also that, in principle, it is possible to introduce higher-order correction (although it is very cumbersome, see ref. [412]). Without these, the convergence of the perturbation series is difficult to assess. However, we expect a similar rate of convergence seen in other unrestricted variants, *e.g.*, UMP2. The convergence of unrestricted methods is generally poorer than in their restricted counterparts, a fact that is generally attributed to spin contamination of the wavefunction.^{413,414} Regardless, the energy components should be less sensitive to these features (see, *e.g.*, ref. [415]) than binding energies and reaction barriers, properties on which the convergence rate is usually probed.

9.3 Illustrative examples

The zeroth-order wavefunction and perturbative expressions introduced above lead to a unique perturbation theory-based scheme specifically tailored for decomposing non-covalent interactions within molecules.

Of course, the simplicity associated with approximating the wavefunction as a single Slater determinant is appealing but it imposes certain limitations when using intra-SAPT. A single SD wavefunction is, for instance, not suitable for systems with significant multi-configuration character. Additionally, within the SD approximation, the partitioning of the system into fragments induces a spin contamination of the zeroth-order wavefunction. The contamination will be most problematic in situations where the linker is very small, leading to fictitious interactions near the border of the fragment partitioning, such as a too attractive first-order term or even a slightly positive induction contribution.

Another limitation inherent to any PT scheme is that the perturbation representing the interaction should be small. In line with the issue associated with the spin-contamination, this condition imposes that the fragments should lie fairly far from each other, *i.e.*, the covalently bound linker fragment should correspond to more than one heavy atom.

Finally, the choice of the basis set can be rather sensitive. On one hand, it is known⁴¹⁶ that the SLO-based approaches lack a complete basis set (CBS) limit and that only moderate size basis sets should be used. On the other hand, the proper description of dispersion interaction depends on the presence of sufficient number of virtual orbitals. Akin to other EDA schemes exploiting atom-centered basis sets,^{417,418} double zeta (polarized) basis sets with no diffuse functions are generally recommended.

In the following sections, we provide applications of intra-SAPT for a few illustrative systems in which the previously mentioned limitations are minimal.

9.3.1 Computational details

In each of the proposed examples, the zeroth-order wavefunction was obtained as described in ref. [7] based on an unrestricted spin formalism. The formulas were implemented in a developer version of the Molpro software package.⁴¹⁹

First, the method is validated on prototypical rare gas dimer systems (see Electronic Supporting Information, ESI), showing that when no linker is present, the method reduces to an intermolecular method similar to that of Surján *et al.*³⁹⁹

Unless otherwise stated, all the computations were done with the 6-31G⁴²⁰ basis set on an MP2/6-31G* geometry. The limitation of the current, developer version of the code prevented the use of larger basis sets for all of the investigated systems but results for larger basis sets are provided whenever it was possible (see Table 9.1 in Section 9.3.2 as well as Tables S3 and S4 and Figures S1 and S2 in the ESI). For the sake of clarity, the terms E_{deloc} and E_{pot} were summed and labeled as an “induction” term, E_{ind} , in most plots and tables.

In all the investigated systems, the linker (see fragment C from Figure 9.1) is bonded either non-covalently or through single covalent bonds to the fragments A and B. To minimize spurious ionic interactions, the occupied spinorbitals were distributed in such a way that each of the fragments corresponds to an open-shell system (as opposed to closed-shell ionic fragments).

9.3.2 Hairpin alkanes-stabilizing effect of dihydrogen contacts

Structurally simple and ubiquitous in nature^{421,422} unbranched alkanes are a perfect illustration of the importance of London dispersion interactions within molecules. In particular, the question regarding at which carbon chain length the folded, “hairpin”-like, conformation is favored over its linear counterpart has been recently addressed by both experimentalists⁴²³ and theoreticians.^{408,424} According to the current consensus, the last globally stable extended alkane is either C₁₇H₃₆ or C₁₈H₃₈. However, the reason for which the alkane molecules do fold has not yet received a direct answer. In analogy to dimers of *n*-alkanes, polyhedranes,⁴²⁵ and spatially aligned [*n*]ladderanes,⁴²⁶ it is assumed that the cumulated dispersion interactions arising from the parallel fragments of chains are at the origin of this conformational isomeric process. In this present context, intra-SAPT can directly reveal the nature of the interactions between the carbon chains in the folded forms.

Here, we investigate carbon chains of lengths from $N = 8$ to $N = 19$. The geometries taken from ref. [408] show three well-defined fragments (see Figure 9.1) with a middle C₄H₈ fragment in each alkane, which naturally serves as the linker between the two interacting hydrocarbon chains of either equal length (when N is an even number) or differing by one CH₂ carbon atom (when N is odd).

We must distinguish (see Figure 9.2) between the odd- and even- alkane chains, differing by their number of carbon atoms and of hydrogen atom contacts, which potentially dictate the nature of the interactions. Actually, the overall trends for the energy terms with respect to the number of carbon atoms remain similar for both the odd and even cases. The induction term is obviously very small as both fragments are neutral, symmetric or nearly symmetric, and spatially distinct. Figure 9.2 shows that up to $N = 12$ the fragments are short and far from each other which results in a near-zero dispersion term. At medium chain lengths, up to $N = 16$ the increase in attractive dispersion contribution is compensated by the growth of the repulsive first-order term. This result is essentially in line with the latest theoretical assessments⁴⁰⁸ that place C₁₆H₃₄ as the largest globally stable unfolded alkane.

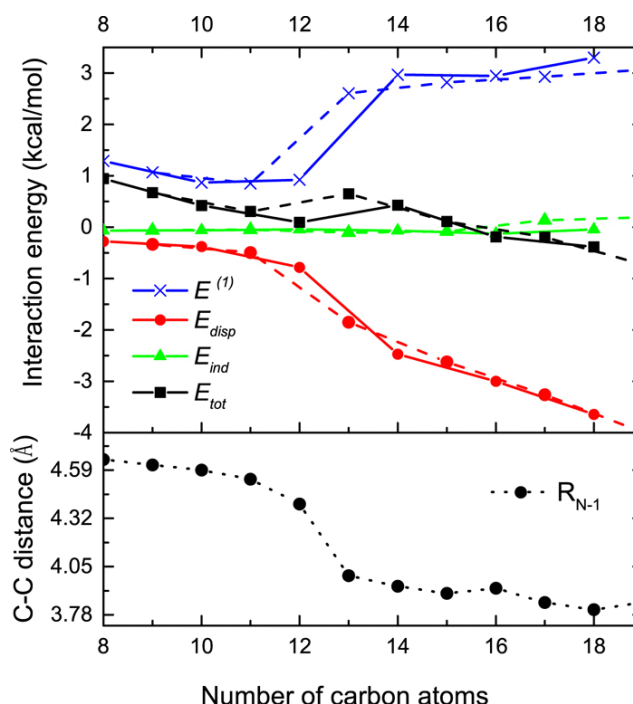


Figure 9.2 Interaction energy components in hairpin alkanes between fragments A and B (see Figure 9.1), 6-31G basis set (upper plot) and the distances of the closest C–C pair in the opposite chains (lower plot, see Figure 9.1) plotted against the number of carbons. The dashed lines are used for the odd-numbered alkanes, the continuous ones for the even-numbered alkanes. Geometries are taken from ref. [408].

As the energetic penalty associated with further distortion of the interfragment bond angles decreases with increasing the chain length, the fragments get closer. Dispersion interactions start to dominate from $C_{16}H_{34}$, resulting in a slightly attractive total interaction. The increase of the dispersion energy originating from the elongation of the carbon chains (*i.e.*, the increased number of interacting electron pairs) causes the side chains to approach one another even more such as to maximize the non-covalent interactions.

Considering that all the investigated geometries (see ref. [408]) were optimized with dispersion-corrected density functionals, it is clear that while for short chains the covalent interfragment bonds play a decisive role in shaping the geometry, the non-covalent interaction (originating from the interplay of Pauli repulsion, electrostatic interaction, and London dispersion) becomes increasingly determinant for longer and more flexible chains. This realization is likely to be relevant for other hairpin-like structures, *e.g.*, phospholipids and hairpin peptides.

It is worthwhile noting that the total interaction arises from a balance of relatively small energy contributions of opposite sign and that it is certainly more reasonable to analyze the trends than an energy value for a specific alkane.

The dependence on the basis set is tested through computing the energies of the small hairpin alkanes ($N = 8, \dots, 14$) with the 6-31G^{*427} basis set (see Figure S1 in ESI). The first order term is less repulsive with 6-31G^{*}, but the trends are identical. The interaction energy components obtained for C_8H_{18} , with a wider selection of basis sets, are presented in Table 9.1. The tested basis sets of comparable size produce similar outcome. To examine the sensitivity of intra-SAPT method to small geometry changes, supplementary computations using the geometries presented in ref. [424] (optimized at MP2/cc-pVTZ level) were performed. The results turned out to be very similar to the ones presented in Figure 9.2 (less than 0.4 kcal/mol of difference in a single component). Those additional tests demonstrate the robustness of the qualitative intra-SAPT trends applied to the hairpin alkanes.

Table 9.1 Components of the intramolecular interaction between C₂H₅ groups in C₈H₁₈ in kcal/mol.

Basis set	$E^{(1)}$	E_{ind}	E_{disp}	E_{tot}
6-31G	1.29	-0.07	-0.28	0.94
6-31G*	0.98	-0.06	-0.30	0.62
6-311G	2.49	0.02	-0.33	2.18
def2-SVP ⁹³	2.06	0.03	-0.49	1.73
cc-pVDZ ⁴²⁸	1.34	0.07	-0.32	1.09

9.3.3 $\pi - \pi$ stacking interactions

π -stacked aromatic chromophores is another appealing class of geometrical patterns that leads to unique properties.⁴²⁹ Their interaction is often analyzed using simpler model systems such as benzene⁴³⁰ and substituted benzene dimers.^{431,432} With intra-SAPT, however, it is possible to access information regarding the same interaction occurring within a molecule. This intramolecular framework opens the possibilities to study closer interchromophore distances that go below van der Waals radii and, which would not be possible with distinct molecules.

Here, we present two examples featuring intramolecular $\pi - \pi$ stacking: 3-phenyl-2(2-phenylacetyl-amino)propionic acid (Phe-L-PHA) (see Figure 9.3, left) and an analogous molecule with the lower phenyl ring replaced by a perfluorophenyl ring (PFB-L-PHA, see Figure 9.3, right). The latter system is employed as a typical building block in supramolecular hydrogelators,⁴³³ the architecture of which is triggered by the intramolecular interaction between the phenyl and the perfluorophenyl ring. Both structures were optimized at the MP2/6-31G* level. The interacting fragments A and B in Phe-L-PHA and PFB-L-PHA are the two aromatic rings.

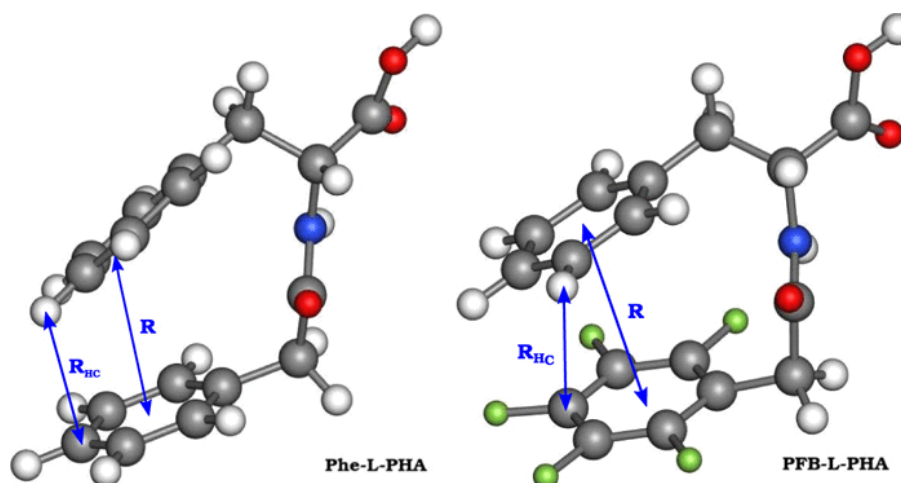


Figure 9.3 Backbone structures of Phe-L-PHA (left) and PFB-L-PHA (right). Color code: O - red, N - blue, F - green, C - grey, H - white. Geometries optimized at the MP2/6-31G* level. Distances between ring centers: Phe-L-PHA - $R = 4.201$ Å, PFB-L-PHA - $R = 3.268$ Å, distances between the closest C-H pair: Phe-L-PHA - $R_{HC} = 2.932$ Å, PFB-L-PHA - $R_{HC} = 3.268$ Å.

As illustrated in Table 9.2, the interaction between the two phenyl rings in Phe-L-PHA is slightly repulsive, with an attractive contribution arising from dispersion and, to a lesser extent, from induction that is compensated by the repulsive first-order term. Note that the phenyl rings in this optimized geometry are rather close, the distance between

the ring centers is $R = 4.201 \text{ \AA}$ (see Figure 9.3), but the upper ring is tilted, which results in one of the H–C distances being as close as $R_{HC} = 2.932 \text{ \AA}$. This geometry is quite far from the typical $\pi - \pi$ stacking “sandwich” conformation (with the rings about 3.8 \AA apart) and does not correspond to any minimum or saddle point of a benzene dimer.⁴³⁰ This situation is reminiscent of that of the medium-size hairpin alkanes and suggests that most medium-size apolar molecules use the attractive dispersion forces to fight against the repulsive wall and form more compact geometries in which the total attraction between fragments is fairly small. The intra-SAPT trend is fully consistent with a SAPT(HF) computation performed on a benzene dimer constrained in the geometry of the Phe-L-PHA phenyl rings using the same basis set (6-31G). SAPT(HF) also reveals a slight repulsion (0.97 kcal/mol) with the first-order term of 4.33 kcal/mol and the dispersion contribution of -3.36 kcal/mol .

Table 9.2 Interaction energy components in kcal/mol between the phenyl rings (Phe-L-PHA) and between the phenyl and pentafluorobenzyl ring (PFB-L-PHA). Computations at the 6-31G level.

	$E^{(1)}$	E_{ind}	E_{disp}	E_{tot}
Phe-L-PHA	5.04	−0.44	−2.07	1.97
PFB-L-PHA	3.88	−0.60	−3.10	0.18

The PFB-L-PHA conformation is closer to a parallel ring arrangement, which is characterized by a larger dispersion energy term. In line with the benzene-pentafluorobenzene complex, the first-order term is less repulsive than for Phe-L-PHA. This difference has often been attributed to the opposite sign of the quadrupole moments of the phenyl ring and perfluorophenyl ring,⁴³⁴ respectively, but has more recently been explained in terms of local dipole-dipole interactions between the substituents and the phenyl ring.⁴³⁵ The two aforementioned effects lead to a negligible total interaction between PFB and Phe rings, which is again consistent with the SAPT(HF)/6-31G result for a phenyl-pentafluorophenyl complex in the same configuration (the first order energy component 4.88 kcal/mol is compensated by the dispersion contribution -5.44 kcal/mol summing up to a total of -0.56 kcal/mol). The small induction and induction-exchange contributions lower the interaction energy further to -0.49 kcal/mol .

The remarkable agreement of intra-SAPT and SAPT(HF) results in this case does not only validate the intra-SAPT results but also indicates that, in this case, the linker does not significantly influence the $\pi - \pi$ interactions. Nevertheless, the linker plays a decisive role in placing the aromatic rings in an orientation that is dictated by the bond and angle strain and not by the maximization of non-covalent interactions. In this respect, the two systems presented here are similar to short hairpin alkanes, where the interaction between the side chains is slightly repulsive.

9.3.4 Intramolecular hydrogen bonds

In its simplest picture, the physical nature of intermolecular hydrogen bonds is essentially discussed in terms of electrostatic interactions, which differs significantly from the previous examples. While the consensus is that the electrostatic contribution accounts for most of the interaction energy, EDA analysis has also highlighted the importance of contributions such as charge transfer, exchange, and dispersion.^{436–439} The intramolecular case is even more controversial as there is no straightforward way to establish its attractive character within a molecule (see *e.g.*, refs. [439,440]). The aminoalcohol series (*i.e.*, 2-aminoethanol, 3-aminopropanol, 4-aminobutanol, and 5-aminopentanol) is a good test case giving access to different orientations and distances between the hydroxyl and the amine group. In fact, the H-bond within small aminoalcohols is believed to be one of the strongest.

The geometries were optimized at the MP2/6-31G* level. The studied interactions were between the hydroxyl group, fragment A, and the NH_2 group, fragment B.

As illustrated in Figure 9.4, the hydrogen bond is strongly attractive due to the electrostatic interaction, with almost no contribution from the second-order terms. The total interaction in the smallest 2-aminoethanol ($N = 4$), $E_{tot} = -6.51$

kcal/mol, is of similar strength as the one in the ammonia-water complex (-6.36 kcal/mol).⁴⁴¹ The hydrogen bond distance shortens from 2.165 Å in 2-aminoethanol down to 1.851 Å in 4-aminobutanol. The bond angle is also dramatically affected going from the pseudo-4- to 6-membered ring as illustrated by the opening of the OHN angle (from 118° to 158°). However, the position and orientation of the hydroxyl group with respect to NH_2 change very slightly between 4-aminobutanol and 5-aminopentanol ($N = 7$) as evidenced by their similar interactions. Akin to the former examples (Section 9.3.2) the maximization of the non-covalent interaction only occurs once sufficient flexibility is achieved within a molecule. Still, the aminoalcohol series shows that those interactions can have a strong impact even on the geometry of small systems. This is a distinctive feature from the hairpin alkane case, which originates from the different nature of the dominant non-covalent interactions. Aminoalcohols are essentially held together by stronger, electrostatic contributions that do not depend on the number of interacting electron pairs and are already efficient in small systems. In contrast, alkane chains must reach a critical length to benefit from the stabilization arising from dispersion.

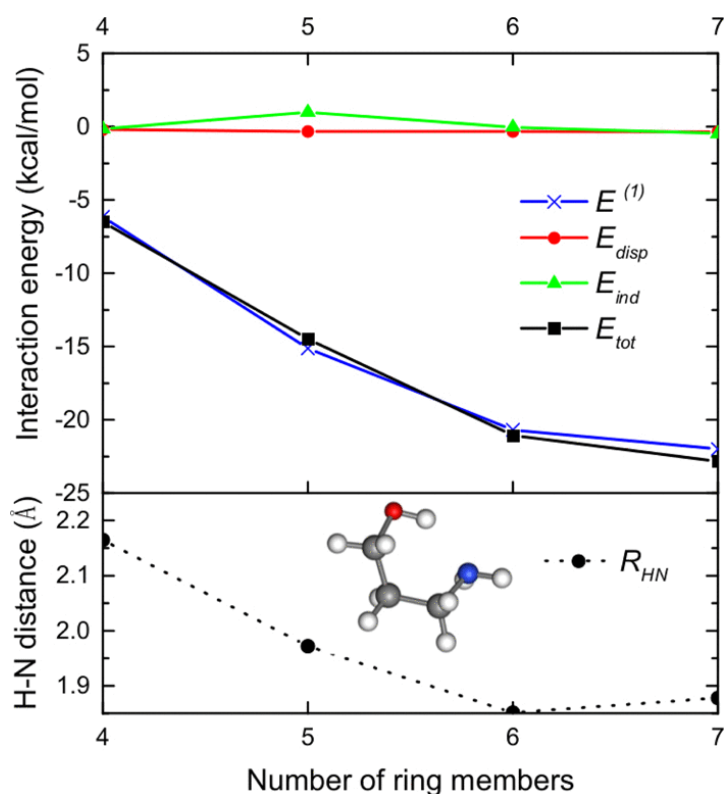


Figure 9.4 Interaction contributions between the hydroxyl and the amine groups in aminoalcohols (upper plot) and the H-N distances (lower plot) in the hydrogen bond, plotted against number of the ring members, 6-31G basis set. Geometries optimized at the MP2/6-31G* level.

The more pronounced hydrogen bond interaction in 3-aminopropanol as compared to the smaller aminoalcohol is consistent with the red shift frequency measured in the vibrational gas phase spectra of the former compound.^{442,443} The magnitude of the total interaction energy for the last two compounds ($E_{tot} = -21.06$ kcal/mol and $E_{tot} = -22.84$ kcal/mol for 4-aminobutanol and 5-aminopentanol, respectively) is in the range of the strongest hydrogen bonds⁴⁴⁴ but one cannot exclude an underestimation of the Pauli repulsion owing to the fragment partitioning. The description of the interfragment bond could however be improved by introducing a spin-coupling scheme,⁴⁴⁵ which is planned.

9.3.5 Host-guest complexes with a cationic guest

While intra-SAPT is essentially designed to decompose intramolecular interactions, it is also highly valuable for probing the competing non-covalent interaction between two functional groups belonging to the same molecule and a particular fragment such as another molecule, ion.

Two examples of such systems are provided in Figure 9.5, where a cationic atom intercalated between two neutral functional groups generates complexes **1** and **2**.

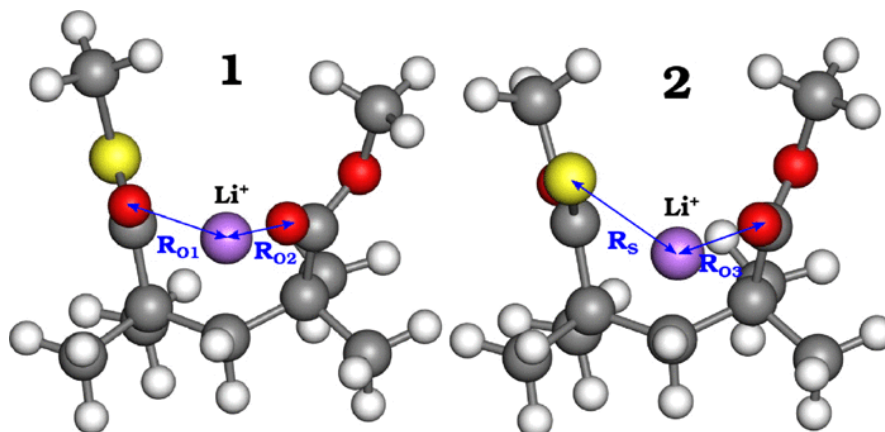


Figure 9.5 Backbone structures of the host-guest complexes. Color code: O - red, S - yellow, Li - purple, C - grey, H - white. Geometries optimized at the MP2/6-31G* level. Distances $R_{01} = 1.849 \text{ \AA}$, $R_{02} = 1.845 \text{ \AA}$, $R_{03} = 1.835 \text{ \AA}$, $R_s = 2.388 \text{ \AA}$.

For each complex two computations are performed: one to probe the interaction between the cationic lithium and the sulfur-containing fragment (*e.g.*, thioester or thionoester, see Table 9.3 and Figure 9.5) and another with Li^+ interacting with the ester functional group. In both cases the middle CH_2 fragment was taken as the linker.

Table 9.3 Interaction energy components between Li^+ and fragments of molecules A and B in kcal/mol. $\text{R}=\text{C}(\text{Me})_2$. Computations with the 6-31G basis set.

System	Fragment A	Fragment B	$E^{(1)}$	E_{deloc}	E_{pol}	E_{disp}	E_{tot}
1	$\text{Li}^+{}^a$	$\text{O}=\text{C}-\text{S}-\text{Me}$ R	-8.00	-17.11	-10.44	-0.03	-35.58
		$\text{O}=\text{C}-\text{O}-\text{Me}$ R	-11.80	-10.18	-12.90	-0.04	-34.92
2	$\text{Li}^+{}^a$	$\text{S}=\text{C}-\text{O}-\text{Me}$ R	54.50	-47.28	-7.98	-0.11	-0.88
		$\text{O}=\text{C}-\text{O}-\text{Me}$ R	-8.39	-18.61	-10.99	-0.03	-38.03

^a Within our scheme it is the whole system positively charged rather than the single lithium atom.

It is apparent from the data in Table 9.3 that the competition between the guest and the functional groups is larger in complex **1** than in **2**. In **1**, both the ester and thioester fragments bound strongly to the lithium with a marginal advantage to the electron-rich thioester. The decomposition *via* intra-SAPT indicates a large electronic redistribution within the ester-type groups engendered by the presence of the cationic lithium causing both their polarization (large E_{pol} contributions) and a large delocalization (*i.e.*, charge transfer). The delocalization is significantly larger with the case

of the richer thioester group, which is more prone to donate. The electrostatic terms are in the same range as the polarization contributions, whereas the binding contribution from dispersion is negligible in both interactions.

Intra-SAPT also indicates that **2** featuring the thionoester group is somewhat trickier and more frustrated chemically.⁴⁴⁶ The guest can interact with both an oxygen or sulfur atom but the interaction with the ester group is clearly stronger and very similar to the interactions observed in complex **1**. To interpret the much lower binding affinity with the thionoester function and the behavior of the individual energy component, one first needs to analyze what happens in the zeroth-order energy computations. When the guest and the sulfur-containing functional group are taken as the interacting fragments A and B, respectively, the relatively strong interaction between them is removed in the zeroth-order computation. In the absence of interacting cationic lithium, the electrons within fragment B are pulled away from sulfur to the more electronegative oxygen atom, creating a dipole with the sulfur atom as the positive pole. Once the interaction is brought back by the perturbation, this polarization engenders a repulsive first-order energy component that is largely compensated by the delocalization term, associated with the ion pulling the electrons towards itself. The polarization term also brings significant attractive contribution, like in all the interactions for both complexes, but is slightly smaller.

The difference between these two complexes agrees with the distinct chemical properties of the two sulfur functional groups.⁴⁴⁶ The presence of the charged lithium atom induces a larger perturbation (and frustration) in the thionoester case, in which the sulfur atom is positioned between the more electron-demanding oxygen atom and the cationic lithium. In contrast, the thioester oxygen atom benefits from the close proximity and electron sharing of the richer sulfur atom without compromise. In a sense, complex **2** may illustrate the limit of the applicability of a perturbation-based method: the electrostatic interaction between the cationic lithium guest and the fragments is so large that it does affect the electron density distribution. This results in an overestimation of the electrostatic repulsion, which is then compensated by the delocalization term. While it is reasonable to interpret the total interaction energies between the cationic lithium and the thionoester group as much weaker than the other interactions, the interpretation of the individual energy terms is delicate in this limiting case.

9.4 Conclusions

We introduced a unique intramolecular variant of SAPT capable of describing the nature of non-covalent intramolecular interactions. The method is clearly different from other existing methods and relies upon a new wavefunction and set of expressions specifically developed for the decomposition of non-covalent intramolecular interactions. This decomposition scheme complements the recently introduced ISAPT method of Parrish *et al.*³⁹⁴ which makes use of the standard two-body SAPT methodology *via* Hartree-Fock embedding.

The approach was used to decompose the interaction energy of hydrogen bonds, $\pi - \pi$ stacked rings and alkane chains within molecules. These illustrative examples along with others involving the competing interaction between a cation and different functional groups belonging to the same molecules demonstrate that intra-SAPT is able to treat both inter- and intramolecular phenomena on an equal footing.

While the present implementation suffers from certain limitations associated with the use of a single Slater determinant wavefunction and the imperfect description of the interfragment bonds, the issue could be overcome through the introduction of spin-coupling scheme.⁴⁴⁵ Akin to other EDA schemes that make use of strictly localized orbitals,^{416,447} intra-SAPT remains ill-defined in the CBS limit but this should not prevent its applications and ability to uncover insightful information previously inaccessible.

In fact, the current implementation has already been able to identify how the role of dispersion evolves with elongating the carbon chain in hairpin alkanes: from being negligible in the short chains up to being the driving force for the formation of the hairpin pattern in the long chains. Similar maximization of the non-covalent interactions was observed in the aminoalcohol series.

Overall the afore-mentioned trends indicate that once a critical size is reached, an optimal molecular conformation should coincide with a local (broadly understood) van der Waals energy minimum. This phenomenon would certainly be worth further examination.

There is no doubt that both ISAPT and intra-SAPT have opened the door to a broad range of new exciting applications. The forthcoming comparisons of these methods not only will illustrate their usefulness and complementarity but also will assist in the development of future improvements.

Chapter 10 Conclusions and Outlook

In this thesis a threefold aim was pursued:

- Examination of structure-property relationships based on excited state dynamics of common organic chromophores, including thiophene and its shortest oligomer – bithiophene, *meso*-substituted BODIPYs and the AIE (aggregation-induced emission) active tetraphenylethylene, with a focus on their ultrafast deactivation pathways and eventual fluorescence quenching.
- Assessment of the accuracy of quantum chemical methods for the computation of excited state energies and properties, with a focus on the limitations of the standard TDDFT approximations for the low-lying $\pi\pi^*$ singlet excited states of thiophene and its derivatives, as well as related L_a and L_b excited states of acenes and heteroacenes.
- Development of a theoretical scheme, intra-SAPT, for quantifying intramolecular interactions in a manner that resembles standard symmetry-adapted perturbation theory (SAPT),³⁸⁷ routinely used for energy decomposition analysis of intermolecular interactions.

Excited state molecular dynamics computations based on the trajectory surface hopping (TSH) scheme³⁴ offer an efficient and reliable way to examine processes occurring on ultrafast timescales, beyond the Born-Oppenheimer approximation. In 2014 Plasser *et al.* adopted a TSH scheme based on the single-reference ADC(2) method for treating the electronic structure problem.³⁷ ADC(2) offers a good balance of accuracy and computational efficiency for many small-to-middle-sized organic molecules and represents a viable alternative to earlier employed multireference and TDDFT methods (the former being reliable but computationally cumbersome, the latter being computationally efficient but its accuracy is difficult to guarantee). Our surface hopping work on thiophene and bithiophene was among the earliest employing the ADC(2) method, and as such offered a useful case study with this relatively novel approach. Thiophene was, furthermore, an important molecular system whose photochemistry triggered a number of articles in the literature. Our aim was to investigate the mechanisms of (singlet) excited state decay occurring upon photoexcitation. Indeed, we brought new qualitative insights to the photochemistry of these compounds, which were missing in earlier theoretical studies that mostly relied on “static” explorations of potential energy surfaces. This illustrates the significance of a “dynamics” perspective – it offers an unbiased way to discern different decay mechanisms and their relative ratios. Furthermore, none of these are directly available from experiment. We also addressed an important question of how much the excited state dynamics of simple model systems (such as thiophene) resembles the dynamics of its derivatives (*e.g.* oligothiophenes). This issue is actively discussed in the literature, for example in the context of whether the excited state dynamics of isolated nucleobases, being certainly well explored, could be extrapolated to the behavior of DNA.⁴⁴⁸ Bithiophene is less prone to nonradiative decay compared to the thiophene monomer, which is due to a larger energy splitting between the low-lying $\pi\pi^*$ singlet states (in which the dynamics mainly takes place) and the $\pi\sigma^*$ states, which provide efficient nonradiative decay channels. Since oligothiophenes are used in many optoelectronic applications, increased photostability is generally a desirable property. In our future research, the investigation should be extended to longer oligothiophenes and oligothienoacenes. Although some work on oligothiophenes (up to quaterthiophene) was recently published,^{79,449} multiple different perspectives are generally welcome since approximations employed by different research groups rarely provide a complete or definitive picture for a particular system. Intersystem crossing in bithiophene (and longer oligothiophenes) certainly deserves more attention, ideally from molecular dynamics perspective. The latter could explain how relatively small spin-orbit couplings can induce an efficient excited state population transfer to the triplet states. Some of the newly developed schemes for TSH, including both the singlet and triplet excited states,^{129,450,451} may be useful in this regard. Overall, thiophene and its oligomers can be employed as realistic model systems for testing new excited state molecular dynamics methods, both

due to their experimental relevance and rich photochemistry. For that reason, it is important to establish benchmark results to which more approximate methods will be compared. One of the computationally viable benchmark approaches is *ab initio* multiple spawning, which, in contrast to TSH, is a formally exact nonadiabatic dynamics theory.⁵⁰

Systems exhibiting an aggregation-induced emission (AIE) effect have recently gained significant research attention,⁴⁵² predominantly due to their applications in imaging, sensing and organic light-emitting diodes. These systems are not fluorescent in the gas phase or in solution, but become highly fluorescent in aggregates and the solid phase. The mechanisms of AIE are not fully understood and are still a matter of debate. Recently, the most widely accepted explanation, the so called restricted intramolecular motion (RIM) concept,⁴⁵² was challenged by the (less general) model of a restricted access to the conical intersection (RACI).²⁴² Here we focused on tetraphenylethylene, one of the foremost and earliest known AIE fluorophores. By employing excited state molecular dynamics we showed that the non-emissive behavior of tetraphenylethylene in the gas phase could be assigned to the accessibility of a conical intersection between the first excited singlet state and the ground state. Two major mechanisms of deactivation through the conical intersection were identified: the ethylenic twist, occasionally assumed earlier, and the dominant, yet unforeseen, mechanism of photocyclization. Moreover, our work prompted further research: for instance a recent study conducted at the CASPT2 level, confirmed the mechanisms we predicted using TDDFT.⁴⁵³ Although our analysis does not extend to the aggregate, it strongly implies the importance of the RACI model. The impact of the aggregate confinement or the crystal structure may be explicitly considered using a QM-MM scheme,¹⁶³ which is an obvious future extension of our work. Additionally, it will be necessary in the future to provide more evidence of the generality of the (RACI) model, *i.e.* to locate critical conical intersections for other AIE dyes, some of which were examined earlier within the Fermi golden rule approximation.^{454,455} As the assumptions behind the Fermi golden rule are not compatible with the existence of the channels involving conical intersections, further research is required to clarify the mechanistic picture behind the AIE. Nevertheless, the methodology we proposed here, combining both static and molecular dynamics computations, has considerable potential for predicting structure-property relationships of novel AIE fluorophores. However, the typical extended size of such molecular systems remains the primary obstacle for predictive computational work. For that reason, it will be necessary to apply and test more approximate excited state methods which could open a way for efficient computational screening, such as newly developed TDDFTB approach.⁴⁵⁶

Our work on *meso*-substituted BODIPY derivatives unraveled the physical reasons behind their contrasting fluorescence properties. BODIPY compounds are highly important organic fluorophores, with vast applications in bio/chemosensing and other fields.¹⁷⁰ The conundrum of fluorescence quenching in certain *meso*-derivatives triggered significant experimental interest, however, without a general – or sometimes even satisfactory – explanation of such phenomena. The theoretical investigations of BODIPY excited state dynamics were previously not feasible, partly due to their challenging cyanine-like electronic structure, which requires the application of correlated quantum chemical methods. Despite the significant computational burden, recent developments made such applications available. We combined both static and dynamic computational approaches to unveil the mechanisms of excited state decay in five different BODIPY derivatives (including the parent dye). The concept of conical intersection accessibility elegantly explains the fluorescence properties of these dyes, *i.e.* energetically accessible conical intersection allows efficient non-radiative deactivation, along with the quenching of radiative pathways. More importantly, we identified two major effects – excited state charge transfer and non-covalent interactions – which shape the excited state potential energy surfaces and influence the accessibility of the conical intersection. Curiously, the role of conical intersections is not well established in the vast BODIPY-related literature and this new concept will be useful for interpreting future experimental findings. Due to the large versatility of BODIPY derivatives, computational protocol which could predict their fluorescence (and other properties) could be a useful tool for rational design. The methodology we proposed opens the way for *in silico* screening and prediction of BODIPY fluorescence properties, prior to their experimental synthesis. Certainly, this is not exclusively restricted to BODIPY derivatives – it applies also to other, similar dyes. Future work should, furthermore, focus more thoroughly on solvation effects, which can affect both the fluorescence quantum yields (for instance, viscous solvents tend to increase fluorescence) and induce solvatochromic shifts. While the latter may be addressed by continuum solvation models, the former requires the use of explicit solvation. Nevertheless, since solvent

tends to extend the excited state decay timescales, the main future challenge will be to efficiently address the long-time (*i.e.*, picoseconds) dynamics of these systems.

The effect of approximate electronic structure methods on the prediction of chemical phenomena cannot be overemphasized. In the context of molecular excited states, the outcome of the computation, say a molecular dynamics simulation, is often highly dependent on the choice of the quantum mechanical model employed for the description of the electronic degrees of freedom. Consequently, we paid particular attention to some of the more challenging cases. Furche *et al.*⁴⁵⁷ correctly assert that: “it is (always) possible to construct excited state benchmarks that favor or disfavor a particular method or conclusion”. However, our opinion is that pinpointing (and rationalizing) the problematic examples is still highly relevant, especially if it affects a large number of applications. We focused on the challenge in predicting the absolute and relative positions of the $\pi\pi^*$ excited singlet states in the spectrum of common (hetero)aromatic molecules. In our early work on thiophene and its derivatives, we identified systematic deficiencies of adiabatic TDDFT with different functional approximations. We analyzed the two lowest $\pi\pi^*$ states and found that for thiophene and fused thiophenes (oligothienoacenes) the sizable errors in both the excited state energies and the interstate gaps (sometimes resulting in incorrect order of the electronic states) occur on a regular basis. The problem also extends to excited state geometries, which turned out to be different from those predicted by more accurate benchmark methods. In general, correlated wavefunction-based methods provide a consistent and qualitatively correct picture, leaving TDDFT at odds. The similarity of such issues with the known problem of L_a and L_b states of acenes³⁰⁰ motivated us to extend the analysis to a broader class of heteroaromatic molecules (*e.g.*, heteroacenes). The so called L_a - and L_b -like states of heteroacenes exhibit disparate electronic characters, which can be hardly captured by approximate quantum chemical methods. In particular, explicit treatment of double excitations is needed for a balanced description of (predominantly singly) excited states. While it is commonly believed that the performance of TDDFT can be optimized by changing the functional approximation, we speculate that the problems of (adiabatic) TDDFT do not originate from the ground state potential (*i.e.*, the functional that is employed) but from the framework of the adiabatic approximation (*i.e.*, the exchange-correlation kernel that is not memory dependent). In our future work, the L_a and L_b states of acenes will be systematically compared to the excited states of heteroaromatics and polyenes based on qualitative molecular orbital theory and valence bond considerations. Such analysis will provide a broader and more fundamental overview of the problems we described earlier. The performance of TDDFT methods going beyond (or “around”)¹⁴ the adiabatic approximation will be systematically investigated. Some of the novel and recently emerging methods (at least in the context of organic molecules), such as the BSE-GW (Bethe-Salpeter equation – GW),⁴⁵⁸ will be tested. Promising developments of new methods combining GW and ADC framework are ongoing in our research lab, and their applications to the challenging excited state problems will be presented in the near future. Such new approaches are generally needed, since performance of the well-established correlated single-reference methods such as ADC(2) and CC2 was found to be system dependent when compared to higher levels of theory. Finally, the impact of the deficiencies of approximate electronic structure methods on excited state geometries and potential energy surfaces needs careful investigation. For instance, a range of such approximate methods should be combined with excited state molecular dynamics to determine how much the quality of potential energy surfaces affects the outcome of dynamics simulations.

As a final topic, we turned to intramolecular non-covalent interactions. Standard methodologies for quantifying weak interactions, *e.g.* symmetry-adapted perturbation theory (SAPT), are only designed for intermolecular situations, which has motivated us to explore the challenging intramolecular counterpart. Some new ideas for the intramolecular aspect have been introduced only recently.³⁹⁴ Here we presented an original approach for intramolecular energy decomposition analysis, built on specifically constructed single Slater determinant wavefunction, which is subject to perturbational corrections. The method is coined intramolecular SAPT (intra-SAPT) due to the similarities, and despite the differences, with standard SAPT. In fact, the present method enables the treatment of both intramolecular and intermolecular interactions on equal footing. The intra-SAPT scheme allows us to extract physically meaningful components of interaction energies, such as the electrostatics-exchange, induction and dispersion contributions. The method was applied to several realistic examples of molecules featuring hydrogen bonds, dihydrogen contacts, and π - π stacking,

providing previously unattainable insights into the nature of these interactions. While the general picture was satisfying, several limitations arose that called for further improvement. In particular, the method is not well defined in the complete basis set limit. Since fragmentation requires the cutting of covalent bonds, large spin contamination may also arise. This may be overcome, for example, by introducing the spin-coupling scheme. In addition, the method is based on the single reference ground state, which is tempting for its simplicity but certainly limits accuracy. Therefore, one of our future goals is to design the multiconfigurational flavor of intra-SAPT. This will open a way to investigate broader classes of molecular systems. From a more general viewpoint, non-covalent interactions are not only relevant for the ground state chemistry, but also for the photochemical and photophysical phenomena taking place in excited states (as shown in Chapter 6). Therefore, future developments should focus on quantifying interactions in the excited states. This is almost an entirely new research avenue, which awaits seminal contributions.

Overall, this thesis has covered a broad spectrum of topics in computational and theoretical chemistry and generated significant outlook. We believe that this work has opened several doors for further investigation and will trigger future research, both by ourselves and other research groups.

References

- (1) Dirac, P. A. M. *Proc. R. Soc. A* **1929**, *123*, 714–733.
- (2) Hoffmann, R. *Chem. Eng. News* **1974**, *52*, 32–34.
- (3) Robb, M. A.; Garavelli, M.; Olivucci, M.; Bernardi, F. In *Reviews in Computational Chemistry, Volume 15*; Lipkowitz, K. B., Boyd, D. B., Eds.; Wiley-VCH, 2007; pp 87–146.
- (4) C. A. Ullrich. *Time-Dependent Density Functional Theory*; Oxford University Press, 2012.
- (5) Dreuw, A.; Wormit, M. *Wiley Interdiscip. Rev. Comput. Mol. Sci.* **2015**, *5*, 82–95.
- (6) Mayer, I. *Int. J. Quantum Chem.* **1983**, *23*, 341–363.
- (7) Gonthier, J. F.; Corminboeuf, C. *J. Chem. Phys.* **2014**, *140*, 154107.
- (8) Marques, M. A. L.; Gross, E. K. U. *Annu. Rev. Phys. Chem.* **2004**, *55*, 427–455.
- (9) Elliott, P.; Burke, K.; Furche, F. In *Reviews in Computational Chemistry*; Lipkowitz, K. B., Cundari, T. R., Eds.; Wiley, 2009; pp 91–165.
- (10) Hohenberg, R.; Kohn, W. *Phys. Rev. B* **1964**, *136*, 864–871.
- (11) Runge, E.; Gross, E. K. U. *Phys. Rev. Lett.* **1984**, *52*, 997–1000.
- (12) Dreuw, A.; Head-Gordon, M. *Chem. Rev.* **2005**, *105*, 4009–4037.
- (13) Kohn, W.; Sham, L. J. *Phys. Rev.* **1965**, *164*, A1133.
- (14) Casida, M. E.; Huix-Rotllant, M. *Annu. Rev. Phys. Chem.* **2012**, *63*, 287–323.
- (15) Shao, Y.; Head-Gordon, M.; Krylov, A. I. *J. Chem. Phys.* **2003**, *118*, 4807–4818.
- (16) Ziegler, T.; Seth, M.; Krykunov, M.; Autschbach, J.; Wang, F. *J. Chem. Phys.* **2009**, *130*, 154102.
- (17) Castro, A.; Appel, H.; Oliveira, M.; Rozzi, C. A.; Andrade, X.; Lorenzen, F.; Marques, M. A. L.; Gross, E. K. U.; Rubio, A. *Phys. Status Solidi B* **2006**, *243*, 2465–2488.
- (18) Lopata, K.; Govind, N. *J. Chem. Theory Comput.* **2011**, *7*, 1344–1355.
- (19) Casida, M. E. In *Recent Advances in Density Functional Methods, Part I*; Chong, D. P., Ed.; World Scientific: Singapore, 1995; pp 155–192.
- (20) Fetter, A. L.; Walecka, J. D. *Quantum Theory of Many-Particle Systems*; Dover Publications, 2003.
- (21) Schirmer, J. *Phys. Rev. A* **1982**, *26*, 2395–2416.
- (22) Trofimov, A. B.; Schirmer, J. *J. Phys. B At. Mol. Opt. Phys.* **1999**, *28*, 2299–2324.
- (23) Hättig, C.; Weigend, F. *J. Chem. Phys.* **2000**, *113*, 5154–5161.
- (24) Schirmer, J. *Phys. Rev. A* **1991**, *43*, 4647–4659.
- (25) Mertins, F.; Schirmer, J. *Phys. Rev. A* **1996**, *53*, 2140–2152.
- (26) Schirmer, J.; Trofimov, A. B. *J. Chem. Phys.* **2004**, *120*, 11449–11464.
- (27) Trofimov, A. B.; Stelter, G.; Schirmer, J. *J. Chem. Phys.* **1999**, *111*, 9982–9999.

- (28) Hättig, C. *Adv. Quantum Chem.* **2005**, *50*, 37–60.
- (29) Tully, J. C. *J. Chem. Phys.* **2012**, *137*, 22A301.
- (30) Born, M.; Oppenheimer, R. *Ann. Phys.* **1927**, *389*, 457–484.
- (31) Born, M.; Huang, K. *Dynamical Theory of Crystal Lattices*; Clarendon Press, 1998.
- (32) De Carvalho, F. F.; Bouduban, M. E. F.; Curchod, B. F. E.; Tavernelli, I. *Entropy* **2014**, *16*, 62–85.
- (33) M. Baer. *Beyond Born-Oppenheimer: Electronic Nonadiabatic Coupling Terms and Conical Intersections*; Wiley-Interscience, 2006.
- (34) Tully, J. C. *J. Chem. Phys.* **1990**, *93*, 1061–1071.
- (35) Tully, J. C. In *Modern Methods for Multidimensional Dynamics Computations in Chemistry*; D. L. Thompson, Ed.; World Scientific: Singapore, 1998; pp 34–72.
- (36) Hammes-Schiffer, S.; Tully, J. C. *J. Chem. Phys.* **1994**, *101*, 4657–4667.
- (37) Plasser, F.; Crespo-Otero, R.; Pederzoli, M.; Pittner, J.; Lischka, H.; Barbatti, M. *J. Chem. Theory Comput.* **2014**, *10*, 1395–1405.
- (38) Schwartz, B. J.; Bittner, E. R.; Prezhdo, O. V.; Rossky, P. J. *J. Chem. Phys.* **1996**, *104*, 5942–5955.
- (39) Zhu, C.; Jasper, A. W.; Truhlar, D. G. *J. Chem. Theory Comput.* **2005**, *1*, 527–540.
- (40) Granucci, G.; Persico, M.; Zocante, A. *J. Chem. Phys.* **2010**, *133*, 134111.
- (41) Subotnik, J. E.; Shenvi, N. *J. Chem. Phys.* **2011**, *134*, 24105.
- (42) Drukker, K. *J. Comput. Phys.* **1999**, *153*, 225–272.
- (43) Jasper, A. W.; Zhu, C.; Nangia, S.; Truhlar, D. G. *Faraday Discuss.* **2004**, *127*, 1–22.
- (44) Granucci, G.; Persico, M. *J. Chem. Phys.* **2007**, *126*, 134114.
- (45) Barbatti, M. *Wiley Interdiscip. Rev. Comput. Mol. Sci.* **2011**, *1*, 620–633.
- (46) Curchod, B. F. E.; Rothlisberger, U.; Tavernelli, I. *ChemPhysChem* **2013**, *14*, 1314–1340.
- (47) Meyer, H. D.; Manthe, U.; Cederbaum, L. S. *Chem. Phys. Lett.* **1990**, *165*, 73–78.
- (48) Worth, G. A.; Meyer, H. D.; Köppel, H.; Cederbaum, L. S.; Burghardt, I. *Int. Rev. Phys. Chem.* **2008**, *27*, 569–606.
- (49) Meyer, H.-D.; Gatti, F.; Worth, G. A. *Multidimensional Quantum Dynamics: MCTDH Theory and Applications*; Wiley-VCH, 2009.
- (50) Ben-Nun, M.; Quenneville, J.; Martínez, T. J. *J. Phys. Chem. A* **2000**, *104*, 5161–5175.
- (51) Snyder, J. W.; Curchod, B. F. E.; Martínez, T. J. *J. Phys. Chem. Lett.* **2016**, *7*, 2444–2449.
- (52) Curchod, B. F. E.; Sisto, A.; Martínez, T. J. *J. Phys. Chem. A* **2017**, *121*, 265–276.
- (53) Abedi, A.; Maitra, N. T.; Gross, E. K. U. *Phys. Rev. Lett.* **2010**, *105*, 123002.
- (54) Sun, X.; Wang, H.; Miller, W. H. *J. Chem. Phys.* **1998**, *109*, 7064–7074.
- (55) Thoss, M.; Stock, G. *Phys. Rev. A* **1999**, *59*, 64–79.
- (56) Bonella, S.; Coker, D. F. *J. Chem. Phys.* **2001**, *114*, 7778–7789.

- (57) Donoso, A.; Martens, C. C. *J. Chem. Phys.* **2000**, *112*, 3980–3989.
- (58) Michl, J.; Bonačić-Koutecký, V. *Electronic Aspects of Organic Photochemistry*; Wiley-Interscience, 1990.
- (59) Klessinger, M.; Michl, J. *Excited States and Photochemistry of Organic Molecules*; Wiley-VCH, 1995.
- (60) Domcke, W.; Yarkony, D. R.; Koppel, H. *Conical Intersections: Theory, Computation and Experiment*; World Scientific Publishing Company, 2011.
- (61) Barbatti, M.; Pittner, J.; Pederzoli, M.; Werner, U.; Mitrić, R.; Bonačić-Koutecký, V.; Lischka, H. *Chem. Phys.* **2010**, *375*, 26–34.
- (62) Makhov, D. V.; Saita, K.; Martinez, T. J.; Shalashilin, D. V. *Phys. Chem. Chem. Phys.* **2015**, *17*, 3316–3325.
- (63) Fuji, T.; Suzuki, Y. I.; Horio, T.; Suzuki, T.; Mitrić, R.; Werner, U.; Bonačić-Koutecký, V. *J. Chem. Phys.* **2010**, *133*, 234303.
- (64) Stenrup, M.; Larson, Å. *Chem. Phys.* **2011**, *379*, 6–12.
- (65) Crespo-Otero, R.; Barbatti, M.; Yu, H.; Evans, N. L.; Ullrich, S. *ChemPhysChem* **2011**, *12*, 3365–3375.
- (66) Crespo-Hernández, C. E.; Cohen, B.; Hare, P. M.; Kohler, B. *Chem. Rev.* **2004**, *104*, 1977–2019.
- (67) Perepichka, I. F.; Perepichka, D. F. *Handbook of Thiophene-based Materials: Applications in Organic Electronics and Photonics*; John Wiley & Sons Ltd, 2009.
- (68) Mishra, A.; Ma, C.; Bäuerle, P. *Chem. Rev.* **2009**, *109*, 1141–1276.
- (69) Zhang, F.; Wu, D.; Xu, Y.; Feng, X. *J. Mater. Chem.* **2011**, *21*, 17590–17600.
- (70) Rupert, B. L.; Mitchell, W. J.; Ferguson, A. J.; Köse, M. E.; Rance, W. L.; Rumbles, G.; Ginley, D. S.; Shaheen, S. E.; Kopidakis, N. *J. Mater. Chem.* **2009**, *19*, 5311–5324.
- (71) Gigli, G.; Inganäs, O.; Anni, M.; De Vittorio, M.; Cingolani, R.; Barbarella, G.; Favaretto, L. *Appl. Phys. Lett.* **2001**, *78*, 1493–1495.
- (72) Mazzeo, M.; Pisignano, D.; Favaretto, L.; Barbarella, G.; Cingolani, R.; Gigli, G. *Synth. Met.* **2003**, *139*, 671–673.
- (73) Irie, M.; Fukaminato, T.; Matsuda, K.; Kobatake, S. *Chem. Rev.* **2014**, *114*, 12174–12277.
- (74) Becker, R. S.; Seixas de Melo, J.; Maçanita, A. L.; Elisei, F. *J. Phys. Chem.* **1996**, *100*, 18683–18695.
- (75) Weinkauff, R.; Lehr, L.; Schlag, E. W.; Salzmann, S.; Marian, C. M. *Phys. Chem. Chem. Phys.* **2008**, *10*, 393–404.
- (76) Salzmann, S.; Kleinschmidt, M.; Tatchen, J.; Weinkauff, R.; Marian, C. M. *Phys. Chem. Chem. Phys.* **2008**, *10*, 380–392.
- (77) Cui, G.; Fang, W. *J. Phys. Chem. A* **2011**, *115*, 11544–11550.
- (78) Stenrup, M. *Chem. Phys.* **2012**, *397*, 18–25.
- (79) Fazzi, D.; Barbatti, M.; Thiel, W. *Phys. Chem. Chem. Phys.* **2015**, *17*, 7787–7799.
- (80) Prlj, A.; Curchod, B. F. E.; Fabrizio, A.; Floryan, L.; Corminboeuf, C. *J. Phys. Chem. Lett.* **2015**, *6*, 13–21.
- (81) Cocchi, C.; Draxl, C. *Phys. Rev. B - Condens. Matter Mater. Phys.* **2015**, *92*, 205126.
- (82) Winter, N. O. C.; Graf, N. K.; Leutwyler, S.; Hättig, C. *Phys. Chem. Chem. Phys.* **2013**, *15*, 6623–6630.
- (83) Knippenberg, S.; Rehn, D. R.; Wormit, M.; Starcke, J. H.; Rusakova, I. L.; Trofimov, A. B.; Dreuw, A. *J. Chem. Phys.* **2012**, *136*, 64107.

- (84) Li, H.; Nieman, R.; Aquino, A. J. A.; Lischka, H.; Tretiak, S. *J. Chem. Theory Comput.* **2014**, *10*, 3280–3289.
- (85) Köppel, H.; Gromov, E. V.; Trofimov, A. B. *Chem. Phys.* **2004**, *304*, 35–49.
- (86) Barbatti, M. *J. Am. Chem. Soc.* **2014**, *136*, 10246–10249.
- (87) Rubio, M.; Merchan, M.; Orti, E.; Roos, B. O. *J. Chem. Phys.* **1995**, *99*, 3580–3586.
- (88) Beljonne, D.; Cornil, J.; Friend, R. H.; Janssen, R. A. J.; Brédas, J. L. *J. Am. Chem. Soc.* **1996**, *118*, 6453–6461.
- (89) Rubio, M.; Merchán, M.; Pou-Amérigo, R.; Ortí, E. *ChemPhysChem* **2003**, *4*, 1308–1315.
- (90) Siegert, S.; Vogeler, F.; Marian, C. M.; Weinkauff, R. *Phys. Chem. Chem. Phys.* **2011**, *13*, 10350–10363.
- (91) Andrzejak, M.; Witek, H. A. *Theor. Chem. Acc.* **2011**, *129*, 161–172.
- (92) Stendardo, E.; Avila Ferrer, F.; Santoro, F.; Improta, R. *J. Chem. Theory Comput.* **2012**, *8*, 4483–4493.
- (93) Weigend, F.; Ahlrichs, R. *Phys. Chem. Chem. Phys.* **2005**, *7*, 3297–3305.
- (94) Rappoport, D.; Furche, F. *J. Chem. Phys.* **2010**, *133*, 134105.
- (95) Barbatti, M.; Aquino, A. J. A.; Lischka, H. *Phys. Chem. Chem. Phys.* **2010**, *12*, 4959–4967.
- (96) Crespo-Otero, R.; Barbatti, M. *Theor. Chem. Acc.* **2012**, *131*, 1237.
- (97) Barbatti, M.; Ruckebauer, M.; Plasser, F.; Pittner, J.; Granucci, G.; Persico, M.; Lischka, H. *Wiley Interdiscip. Rev. Comput. Mol. Sci.* **2014**, *4*, 26–33.
- (98) Furche, F.; Ahlrichs, R.; Hättig, C.; Klopper, W.; Sierka, M.; Weigend, F. *Wiley Interdiscip. Rev. Comput. Mol. Sci.* **2014**, *4*, 91–100.
- (99) Humphrey, W.; Dalke, A.; Schulten, K. *J. Mol. Graph.* **1996**, *14*, 33–38.
- (100) Adamo, C.; Barone, V. *J. Chem. Phys.* **1999**, *110*, 6158–6170.
- (101) Van Lenthe, E.; Baerends, E. J. *J. Comput. Chem.* **2003**, *24*, 1142–1156.
- (102) Wang, F.; Ziegler, T. *J. Chem. Phys.* **2005**, *123*, 154102.
- (103) te Velde, G.; Bickelhaupt, F. M.; Baerends, E. J.; Fonseca Guerra, C.; van Gisbergen, S. J. A.; Snijders, J. G.; Ziegler, T. *J. Comput. Chem.* **2001**, *22*, 931–967.
- (104) Fonseca Guerra, C.; Snijders, J. G.; Te Velde, G.; Baerends, E. J. *Theor. Chem. Acc.* **1998**, *99*, 391–403.
- (105) ADF2013, SCM, Theoretical Chemistry, Vrije Universiteit, Amsterdam, The Netherlands, <http://scm.com>.
- (106) Papajak, E.; Zheng, J.; Xu, X.; Leverentz, H. R.; Truhlar, D. G. *J. Chem. Theory Comput.* **2011**, *7*, 3027–3034.
- (107) Frisch, M. J.; Trucks, G. W.; Schlegel, H. B.; Scuseria, G. E.; Robb, M. A.; Cheeseman, J. R.; Scalmani, G.; Barone, V.; Mennucci, B.; Petersson, G. A.; Nakatsuji, H.; Caricato, M.; Li, X.; Hratchian, H. P.; Izmaylov, A. F.; Bloino, J.; Zheng, G.; Sonnenberg, J. L.; Hada, M.; Ehara, M.; Toyota, K.; Fukuda, R.; Hasegawa, J.; Ishida, M.; Nakajima, T.; Honda, Y.; Kitao, O.; Nakai, H.; Vreven, T.; Montgomery, J. A.; Peralta, J. E.; Ogliaro, F.; Bearpark, M.; Heyd, J. J.; Brothers, E.; Kudin, K. N.; Staroverov, V. N.; Kobayashi, R.; Normand, J.; Raghavachari, K.; Rendell, A.; Burant, J. C.; Iyengar, S. S.; Tomasi, J.; Cossi, M.; Rega, N.; Millam, J. M.; Klene, M.; Knox, J. E.; Cross, J. B.; Bakken, V.; Adamo, C.; Jaramillo, J.; Gomperts, R.; Stratmann, R. E.; Yazyev, O.; Austin, A. J.; Cammi, R.; Pomelli, C.; Ochterski, J. W.; Martin, R. L.; Morokuma, K.; Zakrzewski, V. G.; Voth, G. A.; Salvador, P.; Dannenberg, J. J.; Dapprich, S.; Daniels, A. D.; Farkas, Foresman, J. B.; Ortiz, J. V.; Cioslowski, J.; Fox, D. J. *Gaussian 09, Revision D.01*, Gaussian, Inc., Wallingford CT. 2009.

- (108) González, L.; Escudero, D.; Serrano-Andrés, L. *ChemPhysChem* **2012**, *13*, 28–51.
- (109) Holland, D. M. P.; Trofimov, A. B.; Seddon, E. A.; Gromov, E. V.; Korona, T.; de Oliveira, N.; Archer, L. E.; Joyeux, D.; Nahon, L. *Phys. Chem. Chem. Phys.* **2014**, *16*, 21629–21644.
- (110) Baerends, E. J.; Gritsenko, O. V.; van Meer, R. *Phys. Chem. Chem. Phys.* **2013**, *15*, 16408–16425.
- (111) Flicker, W. M.; Mosher, O. A.; Kuppermann, A. *J. Chem. Phys.* **1976**, *64*, 1315–1321.
- (112) Håkansson, R.; Nordén, B.; Thulstrup, E. W. *Chem. Phys. Lett.* **1977**, *50*, 305–308.
- (113) Dierksen, M.; Grimme, S. *J. Phys. Chem. A* **2004**, *108*, 10225–10237.
- (114) Jacquemin, D.; Planchat, A.; Adamo, C.; Mennucci, B. *J. Chem. Theory Comput.* **2012**, *8*, 2359–2372.
- (115) Palmer, M. H.; Walker, I. C.; Guest, M. F. *Chem. Phys.* **1999**, *241*, 275–296.
- (116) Wu, X. F.; Zheng, X.; Wang, H. G.; Zhao, Y. Y.; Guan, X.; Phillips, D. L.; Chen, X.; Fang, W. *J. Chem. Phys.* **2010**, *133*, 134507.
- (117) Bloom, J. W. G.; Wheeler, S. E. *J. Chem. Theory Comput.* **2014**, *10*, 3647–3655.
- (118) Woon, D. E.; Dunning, T. H. *J. Chem. Phys.* **1993**, *98*, 1358–1371.
- (119) Serrano-Andrés, L.; Merchán, M.; Fülischer, M.; Roos, B. O. *Chem. Phys. Lett.* **1993**, *211*, 125–134.
- (120) Buma, W. J.; Kohler, B. E.; Shaler, T. A. *J. Phys. Chem.* **1994**, *98*, 4990–4992.
- (121) Lap, D. V.; Grebner, D.; Rentsch, S. *J. Phys. Chem. A* **1997**, *101*, 107–112.
- (122) Seixas de Melo, J.; Silva, L. M.; Arnaut, L. G.; Becker, R. S. *J. Chem. Phys.* **1999**, *111*, 5427–5433.
- (123) Beljonne, D.; Shuai, Z.; Pourtois, G.; Bredas, J. L. *J. Phys. Chem. A* **2001**, *105*, 3899–3907.
- (124) Fabiano, E.; Sala, F. Della; Cingolani, R.; Weimer, M.; Görling, A. *J. Phys. Chem. A* **2005**, *109*, 3078–3085.
- (125) Samdal, S.; Samuelsen, E. J.; Volden, H. V. *Synth. Met.* **1993**, *59*, 259–265.
- (126) Kleinschmidt, M.; Tatchen, J.; Marian, C. M. *J. Comput. Chem.* **2002**, *23*, 824–833.
- (127) Becker, R. S.; Seixas De Melo, J.; Maganita, L.; Elisei, F. *Pure Appl. Chem.* **1995**, *67*, 9–16.
- (128) Persico, M.; Granucci, G. *Theor. Chem. Acc.* **2014**, *133*, 1526.
- (129) Richter, M.; Marquetand, P.; González-Vázquez, J.; Sola, I.; González, L. *J. Chem. Theory Comput.* **2011**, *7*, 1253–1258.
- (130) Cui, G.; Thiel, W. *J. Chem. Phys.* **2014**, *141*, 124101.
- (131) Luo, J.; Xie, Z.; Lam, J. W. Y.; Cheng, L.; Tang, B. Z.; Chen, H.; Qiu, C.; Kwok, H. S.; Zhan, X.; Liu, Y.; Zhu, D. *Chem. Commun.* **2001**, *381*, 1740–1741.
- (132) Tong, H.; Hong, Y.; Dong, Y.; Häußler, M.; Lam, J. W. Y.; Li, Z.; Guo, Z.; Guo, Z.; Tang, B. Z. *Chem. Commun.* **2006**, 3705–3707.
- (133) Hong, Y.; Lam, J. W. Y.; Tang, B. Z. *Chem. Commun.* **2009**, 4332–4353.
- (134) Hong, Y.; Lam, J. W. Y.; Tang, B. Z. *Chem. Soc. Rev.* **2011**, *40*, 5361–5388.
- (135) Zhao, Z.; Lam, J. W. Y.; Tang, B. Z. *J. Mater. Chem.* **2012**, *22*, 23726.

- (136) Zhao, Z.; Lu, P.; Lam, J. W. Y.; Wang, Z.; Chan, C. Y. K.; Sung, H. H. Y.; Williams, I. D.; Ma, Y.; Tang, B. Z. *Chem. Sci.* **2011**, *2*, 672–675.
- (137) Chang, Z.; Jiang, Y.; He, B.; Chen, J.; Yang, Z.; Lu, P.; Kwok, H. S.; Zhao, Z.; Qiu, H.; Tang, B. Z. *Chem. Commun.* **2013**, *49*, 594–596.
- (138) Huang, J.; Jiang, Y.; Yang, J.; Tang, R.; Xie, N.; Li, Q.; Kwok, H. S.; Tang, B. Z.; Li, Z. *J. Mater. Chem. C* **2014**, *2*, 2028–2036.
- (139) Chen, Y.; Lam, J. W. Y.; Chen, S.; Tang, B. Z. *J. Mater. Chem. C* **2014**, *2*, 6192–6198.
- (140) Shustova, N. B.; McCarthy, B. D.; Dincă, M. *J. Am. Chem. Soc.* **2011**, *133*, 20126–20129.
- (141) Wei, Z.; Gu, Z. Y.; Arvapally, R. K.; Chen, Y. P.; McDougald, R. N.; Ivy, J. F.; Yakovenko, A. A.; Feng, D.; Omary, M. A.; Zhou, H. C. *J. Am. Chem. Soc.* **2014**, *136*, 8269–8276.
- (142) Zhang, J.; Yang, Q.; Zhu, Y.; Liu, H.; Chi, Z.; Su, C.-Y. *Dalt. Trans.* **2014**, *43*, 15785–15790.
- (143) Wang, M.; Zhang, G.; Zhang, D.; Zhu, D.; Tang, B. Z. *J. Mater. Chem.* **2010**, *20*, 1858–1867.
- (144) Zhang, G.; Hu, F.; Zhang, D. *Langmuir* **2015**, *31*, 4593–4604.
- (145) Lenderink, E.; Duppen, K.; Wiersma, D. A. *J. Phys. Chem.* **1995**, *99*, 8972–8977.
- (146) Zijlstra, R. W. J.; van Duijnen, P. T.; Feringa, B. L.; Steffen, T.; Duppen, K.; Wiersma, D. A. *J. Phys. Chem. A* **1997**, *101*, 9828–9836.
- (147) Zhao, G. J.; Han, K. L.; Lei, Y. B.; Dou, Y. S. *J. Chem. Phys.* **2007**, *127*, 94307.
- (148) Shultz, D. A.; Fox, M. A. *J. Am. Chem. Soc.* **1989**, *111*, 6311–6320.
- (149) Shustova, N. B.; Ong, T. C.; Cozzolino, A. F.; Michaelis, V. K.; Griffin, R. G.; Dincă, M. *J. Am. Chem. Soc.* **2012**, *134*, 15061–15070.
- (150) Mališ, M.; Loquais, Y.; Gloaguen, E.; Biswal, H. S.; Piuze, F.; Tardivel, B.; Brenner, V.; Broquier, M.; Jouvet, C.; Mons, M.; Došlić, N. D. S.; Ljubić, I. *J. Am. Chem. Soc.* **2012**, *134*, 20340–20351.
- (151) Tuna, D.; Došlić, N.; Mališ, M.; Sobolewski, A. L.; Domcke, W. *J. Phys. Chem. B* **2015**, *119*, 2112–2124.
- (152) Prlj, A.; Curchod, B. F. E.; Corminboeuf, C. *Phys. Chem. Chem. Phys.* **2015**, *17*, 14719–14730.
- (153) Sapunar, M.; Ponzi, A.; Chaiwongwattana, S.; Mališ, M.; Prlj, A.; Decleva, P.; Došlić, N. *Phys. Chem. Chem. Phys.* **2015**, *17*, 19012–19020.
- (154) Kosma, K.; Trushin, S. A.; Fuss, W.; Schmid, W. E. *J. Phys. Chem. A* **2008**, *112*, 7514–7529.
- (155) Mori, T.; Glover, W. J.; Schuurman, M. S.; Martinez, T. J. *J. Phys. Chem. A* **2012**, *116*, 2808–2818.
- (156) Sellner, B.; Barbatti, M.; Müller, T.; Domcke, W.; Lischka, H. *Mol. Phys.* **2013**, *111*, 2439–2450.
- (157) Rodier, J. M.; Myers, A. B. *J. Am. Chem. Soc.* **1993**, *115*, 10791–10795.
- (158) Harabuchi, Y.; Keipert, K.; Zahariev, F.; Taketsugu, T.; Gordon, M. S. *J. Phys. Chem. A* **2014**, *118*, 11987–11998.
- (159) Aldred, M. P.; Li, C.; Zhu, M. Q. *Chem. Eur. J.* **2012**, *18*, 16037–16045.
- (160) Kharasch, N.; Alston, T. G.; Lewis, H. B.; Wolf, W. *Chem. Commun.* **1965**, 242–243.
- (161) Molloy, M. S.; Snyder, J. A.; Bragg, A. E. *J. Phys. Chem. A* **2014**, *118*, 3913–3925.
- (162) Guiglion, P.; Zwijnenburg, M. A. *Phys. Chem. Chem. Phys.* **2015**, *17*, 17854–17863.

- (163) Li, Q.; Blancafort, L. *Chem. Commun.* **2013**, *49*, 5966–5968.
- (164) Ruiz-Barragan, S.; Morokuma, K.; Blancafort, L. *J. Chem. Theory Comput.* **2015**, *11*, 1585–1594.
- (165) Novak, J.; Mališ, M.; Prlj, A.; Ljubić, I.; Kühn, O.; Došlić, N. *J. Phys. Chem. A* **2012**, *116*, 11467–11475.
- (166) Hirata, S.; Head-Gordon, M. *Chem. Phys. Lett.* **1999**, *314*, 291–299.
- (167) Wu, W.; Zhang, H.; Braïda, B.; Shaik, S.; Hiberty, P. C. *Theor. Chem. Acc.* **2014**, *133*, 1441.
- (168) Barbatti, M.; Crespo-Otero, E. *Top. Curr. Chem.* **2016**, *368*, 415–444.
- (169) Ioffe, I. N.; Granovsky, A. A. *J. Chem. Theory Comput.* **2013**, *9*, 4973–4990.
- (170) Boens, N.; Leen, V.; Dehaen, W. *Chem. Soc. Rev.* **2012**, *41*, 1130–1172.
- (171) Kolemen, S.; Yusuf Cakmak; Erten-Ela, S.; Altay, Y.; Brendel, J.; Thelakkat, M.; Akkaya, E. U. *Org. Lett.* **2010**, *12*, 3812–3815.
- (172) Kolemen, S.; Bozdemir, O. A.; Cakmak, Y.; Barin, G.; Erten-Ela, S.; Marszalek, M.; Yum, J.-H.; Zakeeruddin, S. M.; Nazeeruddin, M. K.; Grätzel, M.; Akkaya, E. U. *Chem. Sci.* **2011**, *2*, 949–954.
- (173) Nepomnyashchii, A. B.; Bard, A. J. *Acc. Chem. Res.* **2012**, *45*, 1844–1853.
- (174) Shi, W. J.; Lo, P. C.; Singh, A.; Ledoux-Rak, I.; Ng, D. K. P. *Tetrahedron* **2012**, *68*, 8712–8718.
- (175) Ulrich, G.; Barsella, A.; Boeglin, A.; Niu, S.; Ziesel, R. *ChemPhysChem* **2014**, *15*, 2693–2700.
- (176) Jagtap, K. K.; Shivran, N.; Mula, S.; Naik, D. B.; Sarkar, S. K.; Mukherjee, T.; Maity, D. K.; Ray, A. K. *Chem. Eur. J.* **2013**, *19*, 702–708.
- (177) Duran-Sampedro, G.; Esnal, I.; Agarrabeitia, A. R.; Bañuelos Prieto, J.; Cerdán, L.; García-Moreno, I.; Costela, A.; Lopez-Arbeloa, I.; Ortiz, M. J. *Chem. Eur. J.* **2014**, *20*, 2646–2653.
- (178) Ulrich, G.; Ziesel, R.; Harriman, A. *Angew. Chemie - Int. Ed.* **2008**, *47*, 1184–1201.
- (179) Umezawa, K.; Matsui, A.; Nakamura, Y.; Citterio, D.; Suzuki, K. *Chem. Eur. J.* **2009**, *15*, 1096–1106.
- (180) Wu, W.; Guo, H.; Wu, W.; Ji, S.; Zhao, J. *J. Org. Chem.* **2011**, *76*, 7056–7064.
- (181) Nepomnyashchii, A. B.; Bröring, M.; Ahrens, J.; Bard, A. J. *J. Am. Chem. Soc.* **2011**, *133*, 8633–8645.
- (182) Kölmel, D. K.; Hörner, A.; Castañeda, J. A.; Ferencz, J. A. P.; Bihlmeier, A.; Nieger, M.; Bräse, S.; Padilha, L. A. *J. Phys. Chem. C* **2016**, *120*, 4538–4545.
- (183) Saikawa, M.; Nakamura, T.; Uchida, J.; Yamamura, M.; Nabeshima, T. *Chem. Commun.* **2016**, *52*, 10727–10730.
- (184) Chibani, S.; Le Guennic, B.; Charaf-Eddin, A.; Laurent, A. D.; Jacquemin, D. *Chem. Sci.* **2013**, *4*, 1950–1963.
- (185) Le Guennic, B.; Maury, O.; Jacquemin, D. *Phys. Chem. Chem. Phys.* **2012**, *14*, 157–164.
- (186) Momeni, M. R.; Brown, A. J. *J. Phys. Chem. A* **2016**, *120*, 2550–2560.
- (187) Liu, X.; Zhang, J.; Li, K.; Sun, X.; Wu, Z.; Ren, A.; Feng, J. *Phys. Chem. Chem. Phys.* **2013**, *15*, 4666–4676.
- (188) Mukherjee, S.; Thilagar, P. *RSC Adv.* **2015**, *5*, 2706–2714.
- (189) Wang, J.-N.; Jin, J.-L.; Geng, Y.; Sun, S.-L.; Xu, H.-L.; Lu, Y.-H.; Su, Z.-M. *J. Comput. Chem.* **2013**, *34*, 566–575.
- (190) Ziesel, R.; Ulrich, G.; Harriman, A. *New J. Chem.* **2007**, *31*, 496–501.

- (191) Bañuelos, J. *Chem. Rec.* **2016**, *16*, 335–348.
- (192) Kee, H. L.; Kirmaier, C.; Yu, L.; Thamyongkit, P.; Youngblood, W. J.; Calder, M. E.; Ramos, L.; Noll, B. C.; Bocian, D. F.; Scheldt, W. R.; Birge, R. R.; Lindsey, J. S.; Holten, D. *J. Phys. Chem. B* **2005**, *109*, 20433–20443.
- (193) Hu, R.; Lager, E.; Aguilar-Aguilar, A.; Liu, J.; Lam, J. W. Y.; Sung, H. H. Y.; Williams, I. D.; Zhong, Y.; Wong, K. S.; Peña-Cabrera, E.; Tang, B. Z. *J. Phys. Chem. C* **2009**, *113*, 15845–15853.
- (194) Bañuelos, J.; Arroyo-Córdoba, I. J.; Valois-Escamilla, I.; Alvarez-Hernández, A.; Peña-Cabrera, E.; Hu, R.; Tang, B. Z.; Esnal, I.; Martínez, V.; López Arbeloa, I. *RSC Adv.* **2011**, *1*, 677–684.
- (195) Pakhomov, A. A.; Kononevich, Y. N.; Korlyukov, A. A.; Martynov, V. I.; Muzafarov, A. M. *Mendeleev Commun.* **2016**, *26*, 196–198.
- (196) Arroyo, I. J.; Hu, R.; Tang, B. Z.; López, F. I.; Peña-Cabrera, E. *Tetrahedron* **2011**, *67*, 7244–7250.
- (197) Lincoln, R.; Greene, L. E.; Bain, C.; Flores-Rizo, J. O.; Bohle, D. S.; Cosa, G. *J. Phys. Chem. B* **2015**, *119*, 4758–4765.
- (198) Krumova, K.; Cosa, G. *J. Am. Chem. Soc.* **2010**, *132*, 17560–17569.
- (199) Jiao, L.; Yu, C.; Wang, J.; Briggs, E. A.; Besley, N. A.; Robinson, D.; Ruedas-Rama, M. J.; Orte, A.; Crovetto, L.; Talavera, E. M.; Alvarez-Pez, J. M.; Van der Auweraer, M.; Boens, N. *RSC Adv.* **2015**, *5*, 89375–89388.
- (200) Lu, H.; Mack, J.; Yang, Y.; Shen, Z. *Chem. Soc. Rev.* **2014**, *43*, 4778–4823.
- (201) Atchity, G. J.; Xantheas, S. S.; Ruedenberg, K. *J. Chem. Phys.* **1991**, *95*, 1862–1876.
- (202) Matsika, S.; Krause, P. *Annu. Rev. Phys. Chem.* **2011**, *62*, 621–643.
- (203) Domcke, W.; Yarkony, D. R. *Annu. Rev. Phys. Chem.* **2012**, *63*, 325–352.
- (204) Harabuchi, Y.; Taketsugu, T.; Maeda, S. *Phys. Chem. Chem. Phys.* **2015**, *17*, 22561–22565.
- (205) Barbatti, M.; Lischka, H. *Phys. Chem. Chem. Phys.* **2015**, *17*, 15452–15459.
- (206) Brazard, J.; Bizimana, L. A.; Gellen, T.; Carbery, W. P.; Turner, D. B. *J. Phys. Chem. Lett.* **2016**, *7*, 14–19.
- (207) Prlj, A.; Došlić, N.; Corminboeuf, C. *Phys. Chem. Chem. Phys.* **2016**, *18*, 11606–11609.
- (208) Blancafort, L. *ChemPhysChem* **2014**, *15*, 3166–3181.
- (209) Buyuktemiz, M.; Duman, S.; Dede, Y. *J. Phys. Chem. A* **2013**, *117*, 1665–1669.
- (210) Weigend, F. *Phys. Chem. Chem. Phys.* **2006**, *8*, 1057–1065.
- (211) Tuna, D.; Sobolewski, A. L.; Domcke, W. *J. Phys. Chem. A* **2014**, *118*, 122–127.
- (212) Liu, X.; Karsili, T. N. V.; Sobolewski, A. L.; Domcke, W. *J. Phys. Chem. B* **2015**, *119*, 10664–10672.
- (213) Karsili, T. N. V.; Tuna, D.; Ehrmaier, J.; Domcke, W. *Phys. Chem. Chem. Phys.* **2015**, *17*, 32183–32193.
- (214) Tuna, D.; Domcke, W. *Phys. Chem. Chem. Phys.* **2016**, *18*, 947–955.
- (215) Kochman, M. A.; Tajti, A.; Morrison, C. A.; Miller, R. J. D. *J. Chem. Theory Comput.* **2015**, *11*, 1118–1128.
- (216) Chaiwongwattana, S.; Sapunar, M.; Ponzi, A.; Decleva, P.; Došlić, N. *J. Phys. Chem. A* **2015**, *119*, 10637–10644.
- (217) Szabla, R.; Gora, R. W.; Sponer, J. *Phys. Chem. Chem. Phys.* **2016**, *18*, 20208–20218.
- (218) Charaf-Eddin, A.; Le Guennic, B.; Jacquemin, D. *RSC Adv.* **2014**, *4*, 49449–49456.

- (219) Le Guennic, B.; Jacquemin, D. *Acc. Chem. Res.* **2015**, *48*, 530–537.
- (220) Momeni, M. R.; Brown, A. J. *J. Chem. Theory Comput.* **2015**, *11*, 2619–2632.
- (221) Levine, B. G.; Coe, J. D.; Martínez, T. J. *J. Phys. Chem. B* **2008**, *112*, 405–413.
- (222) Tuna, D.; Lefrancois, D.; Wolański, Ł.; Gozem, S.; Schapiro, I.; Andruniów, T.; Dreuw, A.; Olivucci, M. *J. Chem. Theory Comput.* **2015**, *11*, 5758–5781.
- (223) Kowada, T.; Maeda, H.; Kikuchi, K. *Chem. Soc. Rev.* **2015**, *44*, 4953–4972.
- (224) Erten-Ela, S.; Yilmaz, M. D.; Icli, B.; Dede, Y.; Icli, S.; Akkaya, E. U. *Org. Lett.* **2008**, *10*, 3299–3302.
- (225) Lu, Z.; Liang, M.; Dai, P.; Miao, K.; Zhang, C.; Sun, Z.; Xue, S. *J. Phys. Chem. C* **2016**, *120*, 25657–25667.
- (226) López Arbeloa, F.; Bañuelos, J.; Martínez, V.; Arbeloa, T.; López Arbeloa, I. *Int. Rev. Phys. Chem.* **2005**, *24*, 339–374.
- (227) Li, W.; Li, L.; Xiao, H.; Qi, R.; Huang, Y.; Xie, Z.; Jing, X.; Zhang, H. *RSC Adv.* **2013**, *3*, 13417–13421.
- (228) Magagnano, G.; Gualandi, A.; Marchini, M.; Mengozzi, L.; Ceroni, P.; Cozzi, P. G. *Chem. Commun.* **2017**, *53*, 1591–1594.
- (229) Awuah, S. G.; You, Y. *RSC Adv.* **2012**, *2*, 11169–11183.
- (230) Treibs, A.; Kreuzer, F. H. *Justus Liebigs Ann. Chem.* **1968**, *718*, 208–223.
- (231) Arroyo, I. J.; Hu, R.; Merino, G.; Tang, B. Z.; Peña-Cabrera, E. *J. Org. Chem.* **2009**, *74*, 5719–5722.
- (232) Loudet, A.; Burgess, K. *Chem. Rev.* **2007**, *107*, 4891–4932.
- (233) Jiang, X. D.; Zhao, J.; Xi, D.; Yu, H.; Guan, J.; Li, S.; Sun, C. L.; Xiao, L. *J. Chem. Eur. J.* **2015**, *21*, 6079–6082.
- (234) Yang, Y.; Su, X.; Carroll, C. N.; Aprahamian, I. *Chem. Sci.* **2012**, *3*, 610–613.
- (235) Tamgho, I. S.; Hasheminasab, A.; Engle, J. T.; Nemykin, V. N.; Ziegler, C. J. *J. Am. Chem. Soc.* **2014**, *136*, 5623–5626.
- (236) Lee, B.; Park, B. G.; Cho, W.; Lee, H. Y.; Olasz, A.; Chen, C. H.; Park, S. B.; Lee, D. *Chem. Eur. J.* **2016**, *22*, 17321–17328.
- (237) Yang, Y.; Hughes, R. P.; Aprahamian, I. *J. Am. Chem. Soc.* **2012**, *134*, 15221–15224.
- (238) Santos, F. M. F.; Rosa, J. N.; Candeias, N. R.; Carvalho, C. P.; Matos, A. I.; Ventura, A. E.; Florindo, H. F.; Silva, L. C.; Pischel, U.; Gois, P. M. P. *Chem. Eur. J.* **2016**, *22*, 1631–1637.
- (239) Mikysek, T.; Kvapilová, H.; Doušová, H.; Josefík, F.; Šimůnek, P.; Růžicková, Z.; Ludvík, J. *Inorganica Chim. Acta* **2016**, *455*, 465–472.
- (240) Li, F.; Yang, S. I.; Ciringh, Y.; Seth, J.; Martin, C. H.; Singh, D. L.; Kim, D.; Birge, R. R.; Bocian, D. F.; Holten, D.; Lindsey, J. S. *J. Am. Chem. Soc.* **1998**, *120*, 10001–10017.
- (241) Prlj, A.; Fabrizio, A.; Corminboeuf, C. *Phys. Chem. Chem. Phys.* **2016**, *18*, 32668–32672.
- (242) Peng, X.-L.; Ruiz-Barragan, S.; Li, Z.-S.; Li, Q.-S.; Blancafort, L. *J. Mater. Chem. C* **2016**, *4*, 2802–2810.
- (243) Dommett, M.; Crespo-Otero, R. *Phys. Chem. Chem. Phys.* **2017**, *19*, 2409–2416.
- (244) Nguyen, Q. L.; Spata, V. A.; Matsika, S. *Phys. Chem. Chem. Phys.* **2016**, *18*, 20189–20198.
- (245) Qian, H.; Cousins, M. E.; Horak, E. H.; Wakefield, A.; Liptak, M. D.; Aprahamian, I. *Nat. Chem.* **2016**, *9*, 83–87.

- (246) Zhao, J.; Xu, K.; Yang, W.; Wang, Z.; Zhong, F. *Chem. Soc. Rev.* **2015**, *44*, 8904–8939.
- (247) De Simone, B. C.; Mazzone, G.; Pirillo, J.; Russo, N.; Sicilia, E. *Phys. Chem. Chem. Phys.* **2017**, *19*, 2530–2536.
- (248) Ji, S.; Ge, J.; Escudero, D.; Wang, Z.; Zhao, J.; Jacquemin, D. *J. Org. Chem.* **2015**, *80*, 5958–5963.
- (249) Mazzone, G.; Quartarolo, A. D.; Russo, N. *Dye. Pigment.* **2016**, *130*, 9–15.
- (250) Cakmak, Y.; Kolemen, S.; Duman, S.; Dede, Y.; Dolen, Y.; Kilic, B.; Kostereli, Z.; Yildirim, L. T.; Dogan, A. L.; Guc, D.; Akkaya, E. U. *Angew. Chemie - Int. Ed.* **2011**, *50*, 11937–11941.
- (251) De Silva, P.; Corminboeuf, C. *J. Chem. Theory Comput.* **2014**, *10*, 3745–3756.
- (252) Vannay, L.; Bremond, E.; de Silva, P.; Corminboeuf, C. *Chem. Eur. J.* **2016**, *22*, 18442–18449.
- (253) Orte, A.; Debroye, E.; Ruedas-Rama, M. J.; Garcia-Fernandez, E.; Robinson, D.; Crovetto, L.; Talavera, E. M.; Alvarez-Pez, J. M.; Leen, V.; Verbelen, B.; Cunha Dias de Rezende, L.; Dehaen, W.; Hofkens, J.; Van der Auweraer, M.; Boens, N. *RSC Adv.* **2016**, *6*, 102899–102913.
- (254) Kuimova, M. K.; Yahioğlu, G.; Levitt, J. A.; Suhling, K. **2008**, *130*, 6672–6673.
- (255) Adamo, C.; Jacquemin, D. *Chem. Soc. Rev.* **2013**, *42*, 845–856.
- (256) Jacquemin, D.; Chibani, S.; Le Guennic, B.; Mennucci, B. *J. Phys. Chem. A* **2014**, *118*, 5343–5348.
- (257) Briggs, E. A.; Besley, N. A.; Robinson, D. *J. Phys. Chem. A* **2013**, *117*, 2644–2650.
- (258) Komoto, K. T.; Kowalczyk, T. *J. Phys. Chem. A* **2016**, *120*, 8160–8168.
- (259) Spiegel, J. D.; Kleinschmidt, M.; Larbig, A.; Tatchen, J.; Marian, C. M. *J. Chem. Theory Comput.* **2015**, *11*, 4316–4327.
- (260) Knippenberg, S.; Bohnwagner, M. V.; Harbach, P. H. P.; Dreuw, A. *J. Phys. Chem. A* **2015**, *119*, 1323–1331.
- (261) Valiev, R. R.; Sinelnikov, A. N.; Aksenova, Y. V.; Kuznetsova, R. T.; Berezin, M. B.; Semeikin, A. S.; Cherepanov, V. N. *Spectrochim. Acta - Part A Mol. Biomol. Spectrosc.* **2014**, *117*, 323–329.
- (262) Schulten, K.; Dinur, U.; Honig, B. *J. Chem. Phys.* **1980**, *73*, 3927–3835.
- (263) Grimme, S.; Neese, F. *J. Chem. Phys.* **2007**, *127*, 154116.
- (264) Send, R.; Valsson, O.; Filippi, C. *J. Chem. Theory Comput.* **2011**, *7*, 444–455.
- (265) Moore, B.; Autschbach, J. *J. Chem. Theory Comput.* **2013**, *9*, 4991–5003.
- (266) Filatov, M.; Huix-Rotllant, M. *J. Chem. Phys.* **2014**, *141*, 24112.
- (267) Novak, J.; Prlj, A.; Basarić, N.; Corminboeuf, C.; Došlić, N. *Chem. Eur. J.* **2017**, *23*, 8244–8251.
- (268) Lunkenheimer, B.; Köhn, A. *J. Chem. Theory Comput.* **2013**, *9*, 977–994.
- (269) De Silva, P.; Korchowiec, J.; Wesolowski, T. A. *ChemPhysChem* **2012**, *13*, 3462–3465.
- (270) Saleh, G.; Lo Presti, L.; Gatti, C.; Ceresoli, D. *J. Appl. Crystallogr.* **2013**, *46*, 1513–1517.
- (271) Takimiya, K.; Shinamura, S.; Osaka, I.; Miyazaki, E. *Adv. Mater.* **2011**, *23*, 4347–4370.
- (272) Wang, Z. S.; Koumura, N.; Cui, Y.; Takahashi, M.; Sekiguchi, H.; Mori, A.; Kubo, T.; Furube, A.; Hara, K. *Chem. Mater.* **2008**, *20*, 3993–4003.
- (273) Mishra, A.; Pootrakulchote, N.; Wang, M.; Moon, S. J.; Zakeeruddin, S. M.; Grätzel, M.; Bäuerle, P. *Adv. Funct.*

- Mater.* **2011**, *21*, 963–970.
- (274) Gao, P.; Tsao, H. N.; Grätzel, M.; Nazeeruddin, M. K. *Org. Lett.* **2012**, *14*, 4330–4333.
- (275) Ellinger, S.; Graham, K. R.; Shi, P.; Farley, R. T.; Steckler, T. T.; Brookins, R. N.; Taranekar, P.; Mei, J.; Padilha, L. A.; Ensley, T. R.; Hu, H.; Webster, S.; Hagan, D. J.; Van Stryland, E. W.; Schanze, K. S.; Reynolds, J. R. *Chem. Mater.* **2011**, *23*, 3805–3817.
- (276) Sun, X.; Zhou, Y.; Wu, W.; Liu, Y.; Tian, W.; Yu, G.; Qiu, W.; Chen, S.; Zhu, D. *J. Phys. Chem. B* **2006**, *110*, 7702–7707.
- (277) Lim, E.; Jung, B. J.; Shim, H. K. *Macromolecules* **2003**, *36*, 4288–4293.
- (278) Evenson, S. J.; Mumm, M. J.; Pokhodnya, K. I.; Rasmussen, S. C. *Macromolecules* **2011**, *44*, 835–841.
- (279) Zhao, Z.; Deng, C.; Chen, S.; Lam, J. W. Y.; Qin, W.; Lu, P.; Wang, Z.; Kwok, H. S.; Ma, Y.; Qiu, H.; Tang, B. Z. *Chem. Commun.* **2011**, *47*, 8847–8849.
- (280) Zhang, L.; Tan, L.; Wang, Z.; Hu, W.; Zhu, D. *Chem. Mater.* **2009**, *21*, 1993–1999.
- (281) Liu, Y.; Wang, Y.; Wu, W.; Liu, Y.; Xi, H.; Wang, L.; Qiu, W.; Lu, K.; Du, C.; Yu, G. *Adv. Funct. Mater.* **2009**, *19*, 772–778.
- (282) Kang, M. J.; Miyazaki, E.; Osaka, I.; Takimiya, K.; Nakao, A. *ACS Appl. Mater. Interfaces* **2013**, *5*, 2331–2336.
- (283) Li, R.; Dong, H.; Zhan, X.; Li, H.; Wen, S.-H.; Deng, W.-Q.; Han, K.-L.; Hu, W. *J. Mater. Chem.* **2011**, *21*, 11335–11339.
- (284) Kim, H. S.; Kim, Y. H.; Kim, T. H.; Noh, Y. Y.; Pyo, S.; Yi, M. H.; Kim, D. Y.; Kwon, S. K. *Chem. Mater.* **2007**, *19*, 3561–3567.
- (285) Zhang, Y.; Cai, X.; Bian, Y.; Li, X.; Jiang, J. *J. Phys. Chem. C* **2008**, *112*, 5148–5159.
- (286) Wan, J.; Hada, M.; Ehara, M.; Nakatsuji, H. *J. Chem. Phys.* **2001**, *114*, 842–850.
- (287) Rubio, M.; Ortí, E.; Pou-Amérigo, R.; Merchán, M. *J. Phys. Chem. A* **2001**, *105*, 9788–9794.
- (288) Della Sala, F.; Heinze, H. H.; Görling, A. *Chem. Phys. Lett.* **2001**, *339*, 343–350.
- (289) Osuna, R. M.; Zhang, X.; Matzger, A. J.; Hernández, V.; Navarrete, J. T. L. *J. Phys. Chem. A* **2006**, *110*, 5058–5065.
- (290) Aragón, J.; Viruela, P. M.; Gierschner, J.; Ortí, E.; Milián-Medina, B. *Phys. Chem. Chem. Phys.* **2011**, *13*, 1457–1465.
- (291) Laurent, A. D.; Adamo, C.; Jacquemin, D. *Phys. Chem. Chem. Phys.* **2014**, *16*, 14334–14356.
- (292) Andersson, K.; Malmqvist, P. A.; Roos, B. O.; Sadlej, A. J.; Wolinski, K. *J. Phys. Chem.* **1990**, *94*, 5483–5488.
- (293) Nakano, H. *J. Chem. Phys.* **1993**, *99*, 7983–7992.
- (294) Dreuw, A.; Weisman, J. L.; Head-Gordon, M. *J. Chem. Phys.* **2003**, *119*, 2943–2946.
- (295) Tozer, D. J.; Handy, N. C. *Phys. Chem. Chem. Phys.* **2000**, *2*, 2117–2121.
- (296) Casida, M. E.; Jamorski, C.; Casida, K. C.; Salahub, D. R. *J. Chem. Phys.* **1998**, *108*, 4439–4449.
- (297) Maitra, N. T.; Zhang, F.; Cave, R. J.; Burke, K. *J. Chem. Phys.* **2004**, *120*, 5932–5937.
- (298) Levine, B. G.; Ko, C.; Quenneville, J.; Martínez, T. J. *Mol. Phys.* **2006**, *104*, 1039–1051.
- (299) Ziegler, T.; Krykunov, M. *J. Chem. Phys.* **2010**, *133*, 74104.

- (300) Grimme, S.; Parac, M. *ChemPhyschem* **2003**, *4*, 292–295.
- (301) Richard, R. M.; Herbert, J. M. *J. Chem. Theory Comput.* **2011**, *7*, 1296–1306.
- (302) Kuritz, N.; Stein, T.; Baer, R.; Kronik, L. *J. Chem. Theory Comput.* **2011**, *7*, 2408–2415.
- (303) Peach, M. J. G.; Benfield, P.; Helgaker, T.; Tozer, D. J. *J. Chem. Phys.* **2008**, *128*, 44118.
- (304) Wong, B. M.; Hsieh, T. H. *J. Chem. Theory Comput.* **2010**, *6*, 3704–3712.
- (305) Stein, T.; Kronik, L.; Baer, R. *J. Am. Chem. Soc.* **2009**, *131*, 2818–2820.
- (306) Christiansen, O.; Koch, H.; Jørgensen, P. *Chem. Phys. Lett.* **1995**, *243*, 409–418.
- (307) Head-Gordon, M.; Rico, R. J.; Oumi, M.; Lee, T. J. *Chem. Phys. Lett.* **1994**, *219*, 21–29.
- (308) Sekino, H.; Bartlett, R. J. *Int. J. Quant. Chem.* **1984**, *26*, 255–265.
- (309) Nakatsuji, H.; Hirao, K. *J. Chem. Phys.* **1978**, *68*, 2053–2065.
- (310) Bak, B.; Christensen, D.; Hansen-Nygaard, L.; Rastrup-Andersen, J. *J. Mol. Spectrosc.* **1961**, *7*, 58–63.
- (311) Goerigk, L.; Moellmann, J.; Grimme, S. *Phys. Chem. Chem. Phys.* **2009**, *11*, 4611–4620.
- (312) Goerigk, L.; Grimme, S. *Wiley Interdiscip. Rev. Comput. Mol. Sci.* **2014**, *4*, 576–600.
- (313) Chibani, S.; Laurent, A. D.; Blondel, A.; Mennucci, B.; Jacquemin, D. *J. Chem. Theory Comput.* **2014**, *10*, 1848–1851.
- (314) Kantchev, E. A. B.; Norsten, T. B.; Sullivan, M. B. *Org. Biomol. Chem.* **2012**, *10*, 6682–6692.
- (315) Neese, F. *Wiley Interdiscip. Rev. Comput. Mol. Sci.* **2012**, *2*, 73–78.
- (316) Schreiber, M.; Silva-Junior, M. R.; Sauer, S. P. A.; Thiel, W. *J. Chem. Phys.* **2008**, *128*, 134110.
- (317) Jacquemin, D.; Adamo, C. *Top. Curr. Chem.* **2016**, *368*, 347–375.
- (318) Charaf-Eddin, A.; Cauchy, T.; Felpin, F.-X.; Jacquemin, D. *RSC Adv.* **2014**, *4*, 55466–55472.
- (319) Platt, J. R. *J. Chem. Phys.* **1949**, *17*, 484–496.
- (320) Guidez, E. B.; Aikens, C. M. *J. Phys. Chem. C* **2013**, *117*, 21466–21475.
- (321) Perdew, J. P.; Burke, K.; Ernzerhof, M. *Phys. Rev. Lett.* **1996**, *77*, 3865–3868.
- (322) Becke, A. D. *J. Chem. Phys.* **1993**, *98*, 5648–5652.
- (323) Parac, M.; Grimme, S. *Chem. Phys.* **2003**, *292*, 11–21.
- (324) Rohrdanz, M. A.; Herbert, J. M. *J. Chem. Phys.* **2008**, *129*, 34107.
- (325) Knippenberg, S.; Starcke, J. H.; Wormit, M.; Dreuw, A. *Mol. Phys.* **2010**, *108*, 2801–2813.
- (326) Lopata, K.; Reslan, R.; Kowalska, M.; Neuhauser, D.; Govind, N.; Kowalski, K. *J. Chem. Theory Comput.* **2011**, *7*, 3686–3693.
- (327) Goerigk, L.; Grimme, S. *J. Chem. Theory Comput.* **2011**, *7*, 3272–3277.
- (328) Krykunov, M.; Grimme, S.; Ziegler, T. *J. Chem. Theory Comput.* **2012**, *8*, 4434–4440.
- (329) Peng, W. T.; Chai, J. D. *Phys. Chem. Chem. Phys.* **2014**, *16*, 21564–21569.

- (330) Moore, B.; Sun, H.; Govind, N.; Kowalski, K.; Autschbach, J. *J. Chem. Theory Comput.* **2015**, *11*, 3305–3320.
- (331) Senn, F.; Krykunov, M. *J. Phys. Chem. A* **2015**, *119*, 10575–10581.
- (332) Mewes, S. A.; Plasser, F.; Dreuw, A. *J. Chem. Phys.* **2015**, *143*, 171101.
- (333) Shirai, S.; Kurashige, Y.; Yanai, T. *J. Chem. Theory Comput.* **2016**, *12*, 2366–2372.
- (334) Svartsov, Y. N.; Schmitt, M. *J. Chem. Phys.* **2008**, *128*, 214310.
- (335) Arulmozhiraja, S.; Coote, M. L. *J. Chem. Theory Comput.* **2012**, *8*, 575–584.
- (336) Arulmozhiraja, S.; Coote, M. L.; Hasegawa, J. Y. *J. Chem. Phys.* **2015**, *143*, 204304.
- (337) Santoro, F.; Improta, R.; Fahleson, T.; Kauczor, J.; Norman, P.; Coriani, S. *J. Phys. Chem. Lett.* **2014**, *5*, 1806–1811.
- (338) Bartlett, R. J.; Musiał, M. *Rev. Mod. Phys.* **2007**, *79*, 291–352.
- (339) Weigend, F.; Häser, M. *Theor. Chem. Acc.* **1997**, *97*, 331–340.
- (340) Weigend, F.; Häser, M.; Patzelt, H.; Ahlrichs, R. *Chem. Phys. Lett.* **1998**, *294*, 143–152.
- (341) Zhao, Y.; Truhlar, D. G. *Theor. Chem. Acc.* **2008**, *120*, 215–241.
- (342) Zhao, Y.; Truhlar, D. G. *J. Phys. Chem. A* **2006**, *110*, 13126–13130.
- (343) Becke, A. D. *Phys. Rev. A* **1988**, *38*, 3098–3100.
- (344) Lee, C.; Yang, W.; Parr, R. G. *Phys. Rev. B* **1988**, *37*, 785–789.
- (345) Chai, J.-D.; Head-Gordon, M. *Phys. Chem. Chem. Phys.* **2008**, *10*, 6615–6620.
- (346) Iikura, H.; Tsuneda, T.; Yanai, T.; Hirao, K. *J. Chem. Phys.* **2001**, *115*, 3540–3544.
- (347) Harbach, P. H. P.; Wormit, M.; Dreuw, A. *J. Chem. Phys.* **2014**, *141*, 64113.
- (348) Shao, Y.; Gan, Z.; Epifanovsky, E.; Gilbert, A. T. B.; Wormit, M.; Kussmann, J.; Lange, A. W.; Behn, A.; Deng, J.; Feng, X.; Ghosh, D.; Goldey, M.; Horn, P. R.; Jacobson, L. D.; Kaliman, I.; Khaliullin, R. Z.; Kuś, T.; Landau, A.; Liu, J.; Proynov, E. I.; Rhee, Y. M.; Richard, R. M.; Rohrdanz, M. A.; Steele, R. P.; Sundstrom, E. J.; Woodcock, H. L.; Zimmerman, P. M.; Zuev, D.; Albrecht, B.; Alguire, E.; Austin, B.; Beran, G. J. O.; Bernard, Y. A.; Berquist, E.; Brandhorst, K.; Bravaya, K. B.; Brown, S. T.; Casanova, D.; Chang, C.-M.; Chen, Y.; Chien, S. H.; Closser, K. D.; Crittenden, D. L.; Didenhofen, M.; DiStasio, R. A.; Do, H.; Dutoi, A. D.; Edgar, R. G.; Fatehi, S.; Fusti-Molnar, L.; Ghysels, A.; Golubeva-Zadorozhnaya, A.; Gomes, J.; Hanson-Heine, M. W. D.; Harbach, P. H. P.; Hauser, A. W.; Hohenstein, E. G.; Holden, Z. C.; Jagau, T.-C.; Ji, H.; Kaduk, B.; Khistyayev, K.; Kim, J.; Kim, J.; King, R. A.; Klunzinger, P.; Kosenkov, D.; Kowalczyk, T.; Krauter, C. M.; Lao, K. U.; Laurent, A. D.; Lawler, K. V.; Levchenko, S. V.; Lin, C. Y.; Liu, F.; Livshits, E.; Lochan, R. C.; Luenser, A.; Manohar, P.; Manzer, S. F.; Mao, S.-P.; Mardirossian, N.; Marenich, A. V.; Maurer, S. A.; Mayhall, N. J.; Neuscamman, E.; Oana, C. M.; Olivares-Amaya, R.; O'Neill, D. P.; Parkhill, J. A.; Perrine, T. M.; Peverati, R.; Prociuk, A.; Rehn, D. R.; Rosta, E.; Russ, N. J.; Sharada, S. M.; Sharma, S.; Small, D. W.; Sodt, A.; Stein, T.; Stück, D.; Su, Y.-C.; Thom, A. J. W.; Tsuchimochi, T.; Vanovschi, V.; Vogt, L.; Vydrov, O.; Wang, T.; Watson, M. A.; Wenzel, J.; White, A.; Williams, C. F.; Yang, J.; Yeganeh, S.; Yost, S. R.; You, Z.-Q.; Zhang, I. Y.; Zhang, X.; Zhao, Y.; Brooks, B. R.; Chan, G. K. L.; Chipman, D. M.; Cramer, C. J.; Goddard, W. A.; Gordon, M. S.; Hehre, W. J.; Klamt, A.; Schaefer, H. F.; Schmidt, M. W.; Sherrill, C. D.; Truhlar, D. G.; Warshel, A.; Xu, X.; Aspuru-Guzik, A.; Baer, R.; Bell, A. T.; Besley, N. A.; Chai, J.-D.; Dreuw, A.; Dunietz, B. D.; Furlani, T. R.; Gwaltney, S. R.; Hsu, C.-P.; Jung, Y.; Kong, J.; Lambrecht, D. S.; Liang, W.; Ochsenfeld, C.; Rassolov, V. A.; Slipchenko, L. V.; Subotnik, J. E.; Van Voorhis, T.; Herbert, J. M.; Krylov, A. I.; Gill, P. M. W.; Head-Gordon, M. *Mol. Phys.* **2015**, *113*, 184–215.
- (349) Peach, M. J. G.; Williamson, M. J.; Tozer, D. J. *J. Chem. Theory Comput.* **2011**, *7*, 3578–3585.
- (350) Peach, M. J. G.; Tozer, D. J. *J. Phys. Chem. A* **2012**, *116*, 9783–9789.

- (351) Hashimoto, T.; Nakano, H.; Hirao, K. *J. Chem. Phys.* **1996**, *104*, 6244–6258.
- (352) Koch, H.; Christiansen, O.; Jørgensen, P.; Sanchez de Merás, A. M.; Helgaker, T. *J. Chem. Phys.* **1997**, *106*, 1808–1818.
- (353) Casanova, D.; Head-Gordon, M. *J. Chem. Phys.* **2008**, *129*, 64104.
- (354) Laurent, A. D.; Jacquemin, D. *Int. J. Quantum Chem.* **2013**, *113*, 2019–2039.
- (355) Rubio, M.; Merchà, M.; Orti, E.; Roos, B. O. *Chem. Phys.* **1994**, *179*, 395–409.
- (356) Silva-Junior, M. R.; Schreiber, M.; Sauer, S. P. A.; Thiel, W. *J. Chem. Phys.* **2010**, *133*, 174318.
- (357) Silva-Junior, M. R.; Schreiber, M.; Sauer, S. P. A.; Thiel, W. *J. Chem. Phys.* **2008**, *129*, 104103.
- (358) Zanker, V.; Schmid, W. *Chem. Ber.* **1957**, *90*, 2253–2265.
- (359) Subotnik, J. E. *J. Chem. Phys.* **2011**, *135*, 71104.
- (360) Jacquemin, D.; Duchemin, I.; Blase, X. *J. Chem. Theory Comput.* **2015**, *11*, 5340–5359.
- (361) Jeffrey, G. A. *An Introduction to Hydrogen Bonding*; Oxford University Press: New York, 1997.
- (362) Metrangolo, P.; Meyer, F.; Pilati, T.; Resnati, G.; Terraneo, G. *Angew. Chemie - Int. Ed.* **2008**, *47*, 6114–6127.
- (363) Hagemann, M.; Berger, R. J. F.; Hayes, S. A.; Stammli, H. G.; Mitzel, N. W. *Chem. Eur. J.* **2008**, *14*, 11027–11038.
- (364) Scherer, W.; Sirsch, P.; Shorokhov, D.; Tafipolsky, M.; McGrady, G. S.; Gullo, E. *Chem. Eur. J.* **2003**, *9*, 6057–6070.
- (365) Dougherty, D. A.; Stauffer, D. A. *Science.* **1990**, *250*, 1558–1560.
- (366) Schneider, H. J. *Angew. Chemie - Int. Ed.* **2009**, *48*, 3924–3977.
- (367) Scheiner, S. *Noncovalent Forces*; Cham Springer International Publishing, 2015.
- (368) Raynal, M.; Ballester, P.; Vidal-Ferran, A.; van Leeuwen, P. W. N. M. *Chem. Soc. Rev.* **2014**, *43*, 1660–1733.
- (369) McMullin, C. L.; Jover, J.; Harvey, J. N.; Fey, N. *Dalt. Trans.* **2010**, *39*, 10833–10836.
- (370) McMullin, C. L.; Fey, N.; Harvey, J. N. *Dalt. Trans.* **2014**, *43*, 13545–13556.
- (371) Ehrlich, S.; Bettinger, H. F.; Grimme, S. *Angew. Chemie - Int. Ed.* **2013**, *52*, 10892–10895.
- (372) Scheraga, H. A. In *The Proteins Composition, Structure, and Function, Volume 1*; Neurath, H., Ed.; Elsevier, 2012; p 477.
- (373) Brillante, A.; Bilotti, I.; Della Valle, R. G.; Venuti, E.; Girlando, A. *CrystEngComm* **2008**, *10*, 937–946.
- (374) Ferella, L.; Rosato, A.; Turano, T.; Plavec, J. *What Can be Learned About the Structure and Dynamics of Biomolecules from NMR*; Wiley Online Library, 2012.
- (375) Lin, S.; Chen, J.-L.; Huang, L.-S.; Lin, H.-W. *Curr. Proteomics* **2005**, *2*, 55–81.
- (376) Munshi, P.; Row, T. N. G. *J. Phys. Chem. A* **2005**, *109*, 659–672.
- (377) van Oijen, A. M. *Curr. Opin. Biotechnol.* **2011**, *22*, 75–80.
- (378) Johnson, E. R.; Keinan, S.; Mori Sánchez, P.; Contreras García, J.; Cohen, A. J.; Yang, W. *J. Am. Chem. Soc.* **2010**, *132*, 6498–6506.
- (379) Bader, R. F. W. *Chem. Rev.* **1991**, *91*, 893–928.

- (380) Kitaura, K.; Morokuma, K. *Int. J. Quantum Chem.* **1976**, *10*, 325–340.
- (381) Schütz, M.; Rauhut, G.; Werner, H.-J. *J. Phys. Chem. A* **1998**, *102*, 5997–6003.
- (382) Day, P. N.; Jensen, J. H.; Gordon, M. S.; Webb, S. P.; Stevens, W. J.; Krauss, M.; Garmer, D.; Basch, H.; Cohen, D. *J. Chem. Phys.* **1996**, *105*, 1968–1986.
- (383) Addicoat, M. A.; Collins, M. A. *J. Chem. Phys.* **2009**, *131*, 104103.
- (384) Mochizuki, Y.; Fukuzawa, K.; Kato, A.; Tanaka, S.; Kitaura, K.; Nakano, T. *Chem. Phys. Lett.* **2005**, *410*, 247–253.
- (385) Mo, Y.; Gao, J.; Peyerimhoff, S. D. *J. Chem. Phys.* **2000**, *112*, 5530–5538.
- (386) Khaliullin, R. Z.; Head-Gordon, M.; Bell, A. T. *J. Chem. Phys.* **2006**, *124*, 204105.
- (387) Jeziorski, B.; Moszynski, R.; Szalewicz, K. *Chem. Rev.* **1994**, *94*, 1887–1930.
- (388) Hohenstein, E. G.; Sherrill, C. D. *J. Chem. Phys.* **2010**, *133*, 104107.
- (389) Hohenstein, E. G.; Jaeger, H. M.; Carrell, E. J.; Tschumper, G. S.; Sherrill, C. D. *J. Chem. Theory Comput.* **2011**, *7*, 2842–2851.
- (390) Hohenstein, E. G.; Parrish, R. M.; Sherrill, C. D.; Turney, J. M.; Schaefer, H. F. *J. Chem. Phys.* **2011**, *135*, 174107.
- (391) Dodziuk, H.; Korona, T.; Lomba, E.; Bores, C. *J. Chem. Theory Comput.* **2012**, *8*, 4546–4555.
- (392) Parrish, R. M.; Sherrill, C. D. *J. Chem. Phys.* **2014**, *141*, 44115.
- (393) Parrish, R. M.; Parker, T. M.; Sherrill, C. D. *J. Chem. Theory Comput.* **2014**, *10*, 4417–4431.
- (394) Parrish, R. M.; Gonthier, J. F.; Corminbœuf, C.; Sherrill, C. D. *J. Chem. Phys.* **2015**, *143*, 51103.
- (395) Su, P.; Chen, Z.; Wu, W. *Chem. Phys. Lett.* **2015**, *635*, 250–256.
- (396) Hobza, P.; Zahradnik, R.; Müller-Dethlefs, K. *Collect. Czechoslov. Chem. Commun.* **2006**, *71*, 443–531.
- (397) Černý, J.; Hobza, P. *Phys. Chem. Chem. Phys.* **2007**, *9*, 5291–5303.
- (398) Wagner, J. P.; Schreiner, P. R. *Angew. Chemie - Int. Ed.* **2015**, *54*, 12274–12296.
- (399) Surján, P. R.; Mayer, I.; Lukovits, I. *Chem. Phys. Lett.* **1985**, *119*, 538–542.
- (400) Mayer, I. *Int. J. Quantum Chem.* **1998**, *70*, 41–63.
- (401) Mayer, I.; Vibok, A. *Mol. Phys.* **1997**, *92*, 503–510.
- (402) Stoll, H.; Wagenblast, G.; Preuss, H. *Theor. Chim. Acta* **1980**, *57*, 169–178.
- (403) Smits, G. F.; Altona, C. *Theor. Chim. Acta* **1985**, *67*, 461–475.
- (404) Gianinetti, E.; Raimondi, M.; Tornaghi, E. *Int. J. Quantum Chem.* **1996**, *60*, 157–166.
- (405) Mo, Y.; Peyerimhoff, S. D. *J. Chem. Phys.* **1998**, *109*, 1687–1697.
- (406) Sironi, M.; Famulari, A. *Theor. Chem. Acc.* **2000**, *103*, 417–422.
- (407) Nagata, T.; Takahashi, O.; Saito, K.; Iwata, S. *J. Chem. Phys.* **2001**, *115*, 3553–3560.
- (408) Liakos, D. G.; Neese, F. *J. Chem. Theory Comput.* **2015**, *11*, 2137–2143.
- (409) Pastorczak, E.; Prlj, A.; Gonthier, J. F.; Corminbœuf, C. *J. Chem. Phys.* **2015**, *143*, 224107.

- (410) Kaplan, I. G. *Theory of Molecular Interactions*; Elsevier Science Ltd., 1986.
- (411) Wilson, S. *Electron Correlation in Molecules*; Courier Corporation, 2014.
- (412) Vibók, Á.; Mayer, I. *Acta Phys. Hungarica* **1990**, *68*, 241–251.
- (413) Gill, P. M. W.; Radom, L. *Chem. Phys. Lett.* **1986**, *132*, 16–22.
- (414) Beran, G. J. O.; Gwaltney, S. R.; Head-Gordon, M. *Phys. Chem. Chem. Phys.* **2003**, *5*, 2488–2493.
- (415) Su, P.; Li, H. *J. Chem. Phys.* **2009**, *131*, 14102.
- (416) Azar, R. J.; Horn, P. R.; Sundstrom, E. J.; Head-Gordon, M. *J. Chem. Phys.* **2013**, *138*, 84102.
- (417) Mayer, I. *Chem. Phys. Lett.* **2000**, *332*, 381–388.
- (418) Steinmann, S. N.; Corminboeuf, C.; Wu, W.; Mo, Y. *J. Phys. Chem. A* **2011**, *115*, 5467–5477.
- (419) Werner, H.-J.; Knowles, P. J.; Knizia, G.; Manby, F. R.; Schütz, M. *WIREs Comput. Mol. Sci.* **2012**, *2*, 242–253.
- (420) Hehre, W. J.; Ditchfield, R.; Pople, J. A. *J. Chem. Phys.* **1972**, *56*, 2257–2261.
- (421) Brassell, S.; Eglinton, G.; Maxwell, J.; Philp, R. *Aquatic Pollutants: Transformation and Biological Effects*; Elsevier, 1978.
- (422) Eichmann, R.; Neuling, P.; Ketseridis, G.; Hahn, J.; Jaenicke, R.; Junge, C. *Atmos. Environ.* **1979**, *13*, 587–599.
- (423) Lüttschwager, N. O. B.; Wassermann, T. N.; Mata, R. A.; Suhm, M. A. *Angew. Chemie - Int. Ed.* **2013**, *52*, 463–466.
- (424) Byrd, J. N.; Bartlett, R. J.; Montgomery, J. A. *J. Phys. Chem. A* **2014**, *118*, 1706–1712.
- (425) Echeverría, J.; Aullón, G.; Danovich, D.; Shaik, S.; Alvarez, S. *Nat. Chem.* **2011**, *3*, 323–330.
- (426) Wagner, J. P.; Schreiner, P. R. *J. Chem. Theory Comput.* **2014**, *10*, 1353–1358.
- (427) Hariharan, P. C.; Pople, J. A. *Theor. Chim. Acta* **1973**, *28*, 213–222.
- (428) Dunning, T. H. *J. Chem. Phys.* **1989**, *90*, 1007–1023.
- (429) Wu, W.; Liu, Y.; Zhu, D. *Chem. Soc. Rev.* **2010**, *39*, 1489–1502.
- (430) Podeszwa, R.; Bukowski, R.; Szalewicz, K. *J. Phys. Chem. A* **2006**, *110*, 10345–10354.
- (431) Sinnokrot, M. O.; Sherrill, C. D. *J. Phys. Chem. A* **2003**, *107*, 8377–8379.
- (432) Sinnokrot, M. O.; Sherrill, C. D. *J. Am. Chem. Soc.* **2004**, *126*, 7690–7697.
- (433) Hsu, S. M.; Lin, Y. C.; Chang, J. W.; Liu, Y. H.; Lin, H. C. *Angew. Chemie - Int. Ed.* **2014**, *53*, 1921–1927.
- (434) Tsuzuki, S.; Uchimaru, T.; Mikami, M. *J. Phys. Chem. A* **2006**, *110*, 2027–2033.
- (435) Wheeler, S. E.; Houk, K. N. *J. Am. Chem. Soc.* **2008**, *130*, 10854–10855.
- (436) Umeyama, H.; Morokuma, K. *J. Am. Chem. Soc.* **1977**, *99*, 1316–1332.
- (437) Beck, J. F.; Mo, Y. *J. Comput. Chem.* **2007**, *28*, 455–466.
- (438) Hoja, J.; Sax, A. F.; Szalewicz, K. *Chem. Eur. J.* **2014**, *20*, 2292–2300.
- (439) Jabłoński, M.; Kaczmarek, A.; Sadlej, A. J. *J. Phys. Chem. A* **2006**, *110*, 10890–10898.

- (440) Lane, J. R.; Contreras-García, J.; Piquemal, J. P.; Miller, B. J.; Kjaergaard, H. G. *J. Chem. Theory Comput.* **2013**, *9*, 3263–3266.
- (441) Tsuzuki, S.; Lüthi, H. P. *J. Chem. Phys.* **2001**, *114*, 3949–3957.
- (442) Kharitonov, Y.; Rodnikova, M. N.; Khoshabova, E. *Bull. Acad. Sci. USSR, Div. Chem. Sci.* **1990**, *39*, 1190–1199.
- (443) Thomsen, D. L.; Axson, J. L.; Schrøder, S. D.; Lane, J. R.; Vaida, V.; Kjaergaard, H. G. *J. Phys. Chem. A* **2013**, *117*, 10260–10273.
- (444) Grabowski, S. J. *Annu. Rep. Prog. Chem., Sect. C* **2006**, *102*, 131–165.
- (445) Cooper, D. L.; Karadakov, P. B. *Int. Rev. Phys. Chem.* **2009**, *28*, 169–206.
- (446) Hadad, C. M.; Rablen, P. R.; Wiberg, K. B. *J. Org. Chem.* **1998**, *63*, 8668–8681.
- (447) Khaliullin, R. Z.; Bell, A. T.; Head-Gordon, M. *Chem. Eur. J.* **2009**, *15*, 851–855.
- (448) Middleton, C. T.; de La Harpe, K.; Su, C.; Law, Y. K.; Crespo-Hernández, C. E.; Kohler, B. *Annu. Rev. Phys. Chem.* **2009**, *60*, 217–239.
- (449) Kölle, P.; Schnappinger, T.; de Vivie-Riedle, R. *Phys. Chem. Chem. Phys.* **2016**, *18*, 7903–7915.
- (450) Pederzoli, M.; Pittner, J. *J. Chem. Phys.* **2017**, *146*, 114101.
- (451) De Carvalho, F. F.; Tavernelli, I. *J. Chem. Phys.* **2015**, *143*, 224105.
- (452) Mei, J.; Leung, N. L. C.; Kwok, R. T. K.; Lam, J. W. Y.; Tang, B. Z. *Chem. Rev.* **2015**, *115*, 11718–11940.
- (453) Gao, Y. J.; Chang, X. P.; Liu, X. Y.; Li, Q. S.; Cui, G.; Thiel, W. *J. Phys. Chem. A* **2017**, *121*, 2572–2579.
- (454) Wu, Q.; Peng, Q.; Niu, Y.; Gao, X.; Shuai, Z. *J. Phys. Chem. A* **2012**, *116*, 3881–3888.
- (455) Wu, Q.; Deng, C.; Peng, Q.; Niu, Y.; Shuai, Z. *J. Comput. Chem.* **2012**, *33*, 1862–1869.
- (456) Trani, F.; Scalmani, G.; Zheng, G.; Carnimeo, I.; Frisch, M. J.; Barone, V. *J. Chem. Theory Comput.* **2011**, *7*, 3304–3313.
- (457) Send, R.; Kühn, M.; Furche, F. *J. Chem. Theory Comput.* **2011**, *7*, 2376–2386.
- (458) Bruneval, F.; Hamed, S. M.; Neaton, J. B. *J. Chem. Phys.* **2015**, *142*, 244101.

Curriculum Vitae

Antonio Prlj

École polytechnique fédérale de Lausanne

Institute of Chemical Science and Engineering

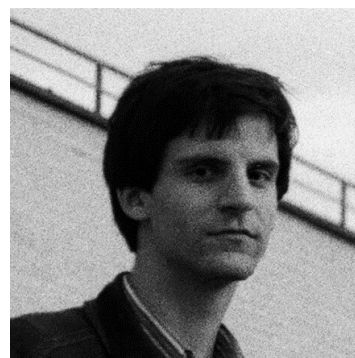
Laboratory for Computational Molecular Design

Tel. +385 (0)98 196 3324

E-mail : antonioprlj@gmail.com

Birth date : June 14, 1989

Nationality : Croatian



Education

- | | |
|---------------------|--|
| 2013-present | PhD in Theoretical and Computational Chemistry , Laboratory for Computational Molecular Design, EPFL, Lausanne, Switzerland <ul style="list-style-type: none">• Advisor : Prof. Clemence Corminboeuf• Main research topics : excited states and nonadiabatic phenomena, organic electronics, non-covalent interactions |
| 2010-2013 | MSc in Chemistry , University of Zagreb (UNIZG), Faculty of Science, Zagreb, Croatia <ul style="list-style-type: none">• Orientation : Physical and organic chemistry• Master thesis under supervision of Dr. Nađa Došlić (Institute Ruđer Bošković, Zagreb) : <i>Nonadiabatic Dynamics of Pyrrole</i> |
| 2007-2010 | BSc in Chemistry , UNIZG, Zagreb, Croatia |

Awards

- | | |
|-------------|--|
| 2015 | Chemistry Travel Award by Swiss Academy of Science / Swiss Chemical Society |
| 2012 | Rector's Award for best student paper, UNIZG |
| 2012 | Medal of the Department of Chemistry, Faculty of Science, UNIZG |

Skills

- **OS** : Linux, Microsoft Windows
- **Programming languages** : Fortran 90, Python, Mathematica
- **Chemistry software** : Turbomole, Gaussian, Gamess, QChem, ADF, Orca, Terachem, Newton-X, VOTCA-CTP, VMD, Gausview
- **Languages** : Croatian (native), English (fluent), French (basic)

Publications

1. Lin, K. H.;[†] **Prlj, A.**;[†] Corminboeuf, C. A Rising Star: Truxene as a Promising Hole Transport Material in Perovskite Solar Cells. *J. Phys. Chem. C* **2017**, *121*, 21729-21739. ([†] contributed equally)
2. Novak, J.; **Prlj, A.**; Basarić, N.; Corminboeuf, C.; Došlić, N. Photochemistry of 1- and 2-Naphthols and Their Water Clusters: The Role of $^1\pi\pi^*(L_a)$ Mediated Hydrogen Transfer to Carbon Atoms. *Chem. Eur. J.* **2017**, *23*, 8244–8251.
3. **Prlj, A.**; Vannay, L.; Corminboeuf, C. Fluorescence Quenching in BODIPY Dyes: The Role of Intramolecular Interactions and Charge Transfer. *Helv. Chim. Acta* **2017**, *100*, e1700093.
4. Gryn'ova, G.; Nicolaï, A.; **Prlj, A.**; Ollitrault, P.; Andrienko, D.; Corminboeuf, C. Charge transport in highly ordered organic nanofibrils: lessons from modelling. *J. Mater. Chem. C* **2017**, *5*, 350-361.
5. Li, J.-H.; Gryn'ova, G.; **Prlj, A.**; Corminboeuf, C. Enhancing the power conversion efficiency of dye-sensitized solar cells *via* molecular plasmon-like excitations. *Chem. Commun.* **2017**, *53*, 2423-2426.
6. **Prlj, A.**; Sandoval-Salinas, M. E.; Casanova, D.; Jacquemin, D.; Corminboeuf, C. Low-Lying $\pi\pi^*$ States of Heteroaromatic Molecules: A Challenge for Excited State Methods *J. Chem. Theory Comput.* **2016**, *12*, 2652–2660.
7. **Prlj, A.**;[†] Fabrizio, A.;[†] Corminboeuf, C. Rationalizing fluorescence quenching in *meso*-BODIPY dyes. *Phys. Chem. Chem. Phys.* **2016**, *18*, 32668-32672. ([†] contributed equally)
8. **Prlj, A.**; Došlić, N.; Corminboeuf, C. How does tetraphenylethylene relax from its excited states? *Phys. Chem. Chem. Phys.* **2016**, *18*, 11606-11609.
9. Pastorczak, E.;[†] **Prlj, A.**;[†] Gonthier, J. F.; Corminboeuf, C. Intramolecular symmetry-adapted perturbation theory with a single-determinant wavefunction. *J. Chem. Phys.* **2015**, *143*, 224107. ([†] contributed equally)
10. **Prlj, A.**; Rotzinger, F. P. Investigation of the water exchange mechanism of the Plutonyl(VI) and Uranyl(VI) ions with quantum chemical methods. *J. Coord. Chem.* **2015**, *68*, 3328-3339.
11. Sapunar, M.; Ponzi, A.; Chaiwongwattana, S.; Mališ, M.; **Prlj, A.**; Decleva, P.; Došlić, N. Timescales of N–H bond dissociation in pyrrole: a nonadiabatic dynamics study. *Phys. Chem. Chem. Phys.* **2015**, *17*, 19012-19020.
12. **Prlj, A.**; Curchod, B. F. E.; Corminboeuf, C. Excited state dynamics of thiophene and bithiophene: new insights into theoretically challenging systems. *Phys. Chem. Chem. Phys.* **2015**, *17*, 14719-14730.

13. **Prlj, A.**; Curchod, B. F. E.; Fabrizio, A.; Floryan, L.; Corminboeuf, C. Qualitatively Incorrect Features in the TDDFT Spectrum of Thiophene-Based Compounds. *J. Phys. Chem. Lett.* **2015**, *6*, 13–21.
14. Liu, H; Brémond E.; **Prlj, A.**; Gonthier, J. F.; Corminboeuf, C. Adjusting the Local Arrangement of π -Stacked Oligothiophenes through Hydrogen Bonds: A Viable Route to Promote Charge Transfer. *J. Phys. Chem. Lett.* **2014**, *5*, 2320–2324.
15. Novak, J.; Mališ, M.; **Prlj, A.**; Ljubić, I.; Kühn, O.; Došlić, N. Photoinduced Dynamics of Formic Acid Monomers and Dimers: The Role of the Double Hydrogen Bond. *J. Phys. Chem. A* **2012**, *116*, 11467–11475.

Contributed Talks

- **Workshop Innovative Surfaces and Materials**, August 2016, Primošten, Croatia, “Challenges in description of optical and electronic properties of heteroaromatic molecules”
- **51st Symposium of Theoretical Chemistry: Chemistry in Motion**, September 2015, Potsdam, Germany, “Excited states conundrum and nonadiabatic molecular dynamics of thiophene based compounds”
- **SCS Fall Meeting**, September 2014, Zürich, Switzerland, “Towards Intramolecular SAPT”

Poster Presentations

- **Excited States Bridging Scales**, November 2016, Marseille, France, “Low-Lying $\pi\pi^*$ States of Heteroaromatic Molecules: A Challenge for Excited State Methods”
- **SCS Fall Meeting**, September 2016, Zürich, Switzerland, “Low-Lying $\pi\pi^*$ States of Heteroaromatic Molecules: A Challenge for Excited State Methods”
- **Computation of Electronic Excited States**, September 2015, Donostia, Spain, “How accurate is the TDDFT for the low-lying $\pi\pi^*$ states of small conjugated molecules?”
- **MPM Conference “Modelling Photoactive Molecules”**, April 2015, Nantes, France, “How accurate is the TDDFT for the Low-Lying $\pi\pi^*$ States of Small Conjugated Molecules?”

